Spray Modelling without Droplet Size Segregation

A thesis submitted to the University of Manchester for the degree
of Doctor of Philosophy in the Faculty of Engineering and
Physical Sciences

2010

Dominic Jones

School of Mechanical, Aerospace and Civil Engineering

Contents

Word count: 25,994 words

List of Figures

List of Tables

Abstract

Spray Modelling without Droplet Size Segregation
Dominic Jones, April 2010
Doctor of Philosophy, University of Manchester

Beck and Watkins [2003a] presented a computational spray model which avoided the need to segregate the local droplet number distribution into parcels of identical droplets. The distribution instead was represented by a continuous function which required its third and fourth moments, μ_2 and μ_3, to determine the free parameter of the function. The form of the continuous function was later revised by Yue and Watkins [2004], who implemented the Gamma distribution whose parameters were obtained from the second, third and fourth moments.

General methods for reconstructing probability density functions are assessed to determine the most suitable means of describing the droplet number distribution. Maximum entropy formalism, splines reconstruction, Legendre and Laguerre polynomials and the Gamma distribution are documented. Of these, the first three are compared, revealing the Maximum entropy formalism as a robust and accurate means to describe the number distribution.

In addition to defining the droplet number distribution, the droplet velocity profile is approximated. Two methods are proposed for reconstructing the profile, an exponential based function and a polynomial function. Only the first method is shown to reconstruct sensible profiles. Implemented into the spray model, varying the exponent of the profile shows how strongly the velocity profile effects the properties of the spray.

A review of the most common droplet hydrodynamic models is presented and implemented into the spray model. A comparison is performed between three droplet break-up models which shows the model of Pilch and Erdman [1987] to be the most suitable. Calculation of hydrodynamic terms dependent on the droplet number distribution and velocity profile are no longer integrated algebraically, as done by Beck [2000], but numerically due to the complexity of the terms.

The spray model is designed such that multiple sprays within a single domain can be transported, enabling splashing and rebounding sprays to be treated independently upon an injected spray impinging on a surface. Outcome regimes of droplet wall impaction provided by Bai and Gosman [1995] are implemented into the spray model. Gradual wetting of the wall is also considered, effecting the outcome regimes.

The model is implemented in a new code, based on current numerical methods detailed in Ferziger and Perić [2002], so as to make use of high resolution differencing schemes for the transportation of the moments [Muzaferija and Peric, 1999] and enable improved resolution of the injector by using an unstructured grid topology.

Parametric testing of the complete spray model shows that for a large range of choices of parameters, the spray model is unstable. This lack of stability is attributed to the poor approximation of the droplet velocity profile. Only with certain specific parameters will the spray model run correctly. With these specific parameters, the experimental case of Park et al. [2004] is modelled, showing that the spray model captures overall features very well, though over-estimates droplet velocity, resulting in a poor comparison of droplet Weber numbers.

Declaration

No portion of the work referred to in the thesis has been submitted in support of an application for another degree or qualification of this or any other university or other institute of learning.

Copyright Statement

Acknowledgements

I wish to thank my supervisor, Dr Paul Watkins, Dr Tim Craft, Dr Colin Steele and Dr Andrew Lowe. I am very grateful for all the help they gave me. Without their generosity and their competence, this project would have been nothing more than a nice idea.

Deo Gratias!

Nomenclature

Symbols with clear conventional meanings, symbols which are adequately defined where they appear in the text, symbols locally modified with subscripts and symbols which represent constants in a particular context are omitted from this list. Units given are the basic units, without multipliers which may be used in practice. Unless stated, material properties without a subscript refer to the continuous phase.

Roman Symbols

A	Area	m^2
C_d	Drag coefficient	-
D	Downstream control volume	-
E	Energy	$\text{kg m}^2 \text{ s}^{-2}$
$\vec{F}$	Force	kg m s^{-2}
k	Gamma distribution parameter	-
k	Turbulent kinetic energy	-
L	Length	m
La	Laplace number	-
m	Mass	kg
$\vec{n}$	Surface normal vector	-
N	Neighbour control volume	-
N	Number	-
$n(r)$	Droplet number distribution	m^{-3}

Oh	Ohnsorge number	-
P	Pole control volume	-
$\vec{p}$	Momentum	kg m s^{-1}
$p(r)$	Approximate probability density function	m^{-3}
q_ϕ	Source term	-
r	Radius	m
r_k	Abscissa	m
Re	Reynolds number	-
S	Surface	-
t	Time	s
$\vec{t}$	Tangential vector	-
U	Upstream control volume	-
$\vec{v}$	Velocity	m s^{-1}
$\vec{V}_{d,i}$	Moment averaged velocity	ms^{-1}
We	Weber number	-
$\vec{x}$	Position vector	m

Greek Symbols

μ	Viscosity	kg m^{-1} s^{-1}
μ_t	Eddy viscosity	kg m^{-1} s^{-1}
μ_i	Moment about the origin	m^{i-3}
μ_i'	Moment about the mean	m^{i-3}
μ_i''	Standardized moment	m^{i-3}
γ_1	Skewness	-
γ_2	Kurtosis	-
$\gamma(\alpha,\beta)$	Incomplete Gamma function	-
$\Gamma(\alpha)$	Gamma function	-
$B(\alpha,\beta)$	Beta function	-
Θ	Volume fraction	-

ρ	Density	kg m^{-3}
σ_d	Surface tension	kg s^{-2}
ϵ	Dissipation rate	m^3 s^{-2}
τ	Time scale	s
$\phi(r)$	Probability density function	m^{-3}
$\psi(r)$	Generic function	-
Ψ	Generic moment averaged property	-
Ω	Domain	m^3
λ	Interpolation constant	-
$\underline{\lambda}$	Lagrange coefficients	-
ω_k	Weight	-

Abbreviations

amb	Ambient
bre	Break-up
coal	Coalescence
col	Collisions
curr	Current
crit	Critical
c	Continuum, continuous, collector
deg	Degree
dr	Drag
d	Droplet, discrete, donor
in	Inlet
init	Initial
inj	Injection
int	Intensity
kin	Kinetic
len	Length

n	Normal
out	Outlet
orif	Orifice
reb	Rebound
r	Radius, random
spd	Speed
spl	Splash, spline
st	Stable
stk	Stick
sur	Surface
th	Thickness
turb	Turbulent
t	Tangential

Acronyms

CFD	Computational fluid dynamics
CV	Control Volume
FV	Finite Volume
GDI	Gasoline direct injection
HRIC	High resolution interface capturing
PDF	Probability density function
SMR	Sauter mean radius
TVD	Total varitaion diminishing
UDS	Upwind differencing scheme

Notation

ρ	Scalar
$\vec{F}$	Spatial vector

$\underline{\phi}$	One dimensional array
$P\,[a,\,b\,]$	Array of elements
$\underline{\vec{v}}$	Array of vectors
$\underline{\underline{A}}$	Matrix
A_{K}	Matrix element
$\|\,\vec{v}\,\|$	Vector magnitude
$\{a,\,b\}$	Components
$\delta\,[x - x_i]$	Dirac delta
$\delta t,\,\Delta t$	Finite interval
$\rightarrow$	Becomes
$\dot{m}$	Rate of
$\binom{i}{j}$	Binomial coefficient

Chapter 1

Introduction

The motivation for modelling sprays is discussed along with currently available methods. Essential elements of such a model and its capacity to deal with particular configurations are outlined, concluding with the specific aims of the project.

1.1 Engine Cycle

The typical internal combustion engine cycle divides into four strokes; intake, compression, combustion and exhaust. The majority of research associated with these kind of engines relates to the first three strokes (Fig. 1.1) with the focus on improving the efficiency of combustion. The vast majority of these engines inject the fuel into the intake port (Multi-Point Injection), allowing sufficient time for the fuel spray to evaporate in the compression stroke, resulting in a homogeneous charge by the time ignition takes place at the beginning of the combustion stroke.

For combustion to take place, the charge must have a sufficiently high air-to-fuel ratio in the vicinity of the heat source. Under low loads, Multi-Point Injection offers no means of stratifying the charge around the heat source, minimizing the amount of fuel required.

This problem was addressed by revisiting the direct injection design. Only recently has there been the technology to advance this method, since it requires very precise timing and control systems to govern the process.

(a) Induction   (b) Compression   (c) Ignition
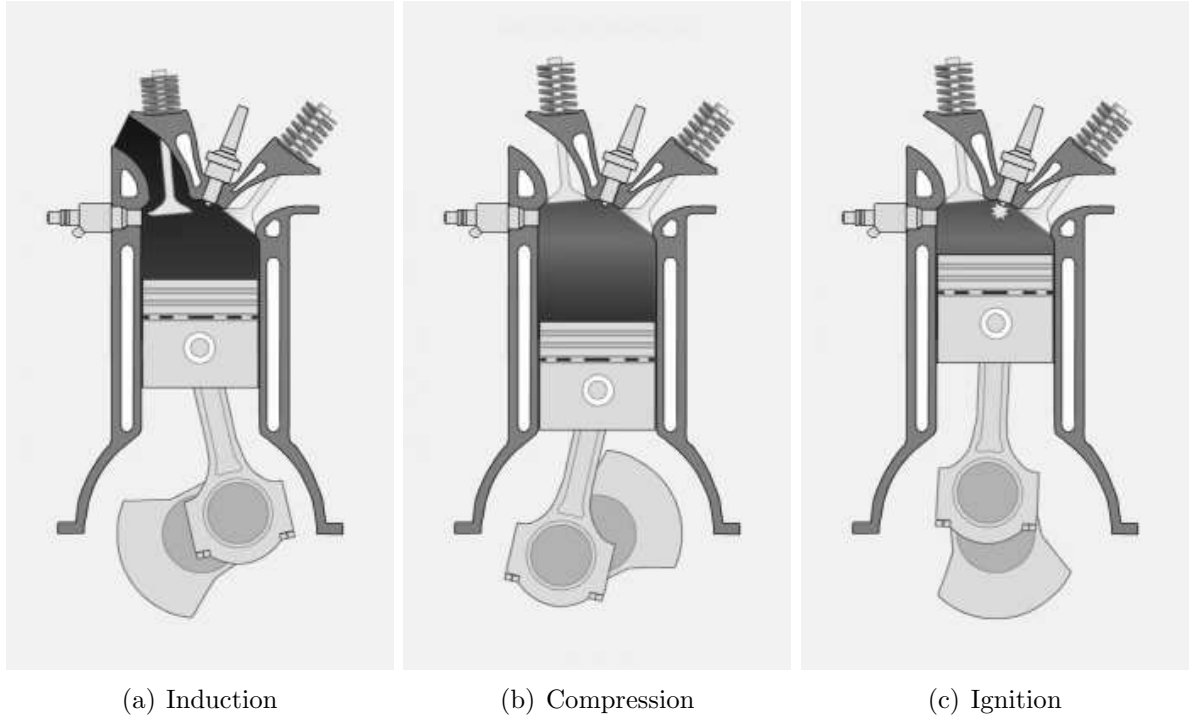
Figure 1.1: Window for fuel injection

1.1.1 Direct Injection

The introduction of Gasoline Direct Injection (GDI) engines provides the opportunity to control the injection and combustion process more precisely over the Multi-Point Injection method, providing the possibility of producing either a stratified or homogeneous charge. In the case of a stratified charge, the atomized fuel is directed towards the heat source by the impingement of the injected spray with the surface of the moving piston, as shown in Fig. 1.2.

Impingement of the spray however, does not necessarily lead to all the droplets rebounding. A number of outcomes are possible, of which not all are desired. Wetting of the piston head, caused by droplets sticking to it, are the cause of piston-top pool fires, which significantly degrade performance and efficiency [Park et al., 2004]. The impingement conditions required are such that either droplets splash or rebound upon impact as opposed to surface wetting. In order for such outcomes to occur, the required operating conditions need to be determined.

Much research has been carried out on GDI engines, such as the effect of compression pressure on the structure of the spray [Wigley et al., 2001], spray imaging in the near-

Figure 1.2: Spray directed towards heat source by the piston surface

nozzle region [Wigley et al., 2004], computational modelling of spray interaction with the piston and cylinder [Tomoda et al., 2001] and experimental analysis of spray impaction [Park et al., 2004], indicating that there is real interest in developing this type of engine.

1.1.2 Spray Development

Since the intended interaction of the piston surface with the spray is to direct the spray and charge towards the heat source, properties of both the spray and carrier gas immediately in front of the surface are required. Key questions about the spray in this region are whether or not the spray is being carried by the gas, as in an aerosol, and what the number, size and velocity of those near wall droplets are. To determine such properties, the injection and propagation characteristics of the spray are required. The state of the carrier gas before and during injection will also have a strong effect on the spray development, causing the dispersion of the spray and influencing the degree of droplet break-up and drag.

1.1.3 Wall Impaction

Provided near wall droplets have a normal velocity component in the direction of the wall, impaction will occur. However, to determine what happens to the droplet upon impaction, further information is required relating to the condition of the wall, since its state strongly effects the outcome of impaction. Wetness, roughness, temperature and material of the piston surface need to be considered. In the case of the wetness of the wall, this is the only property likely to change significantly in the course of the impaction process, becoming wetter as the spray propagates towards it. Rebounding and splashing droplets always experience a reduction in momentum, except for surfaces at a very high temperature, increasing the likelihood of post-impingement droplets being carried by the surrounding gas.

1.1.4 Engine Model

Three possibilities of determining information about the spray development and its interaction with a piston surface are available; by experimentation, correlation and numerical simulation. The work herein aims to develop the last method. A computational model is not fixed to a single engine configuration, enabling it to be a reasonable design tool. The model can be tested, modified and re-tested easily, speeding up the process of optimization. In order to simulate the fluid flow of the entire engine cycle, a number of components are required.

For realistic engine simulations the mechanical system of the engine needs to be properly represented, since this both drives and is driven by contained fluid. This would involve modelling the asynchronous movement of the intake and exhaust valves and the motion of the piston, timed correctly with the valves. Induction of air and its compression precedes the injection of fuel into the chamber, establishing the highly turbulent conditions into which the fuel is injected.

Despite computational methods for simulating continuum fluid flow being well established, the modelling of a complete engine cycle has not yet been realized. This is mainly due to (until recently) the distinction between fluid flow, stress and mechanism modelling software. The engine cycle involves all three branches in a coupled manner.

1.2 Spray Model

A major subsection of engine modelling is simulating the injection and development of the fuel spray and its interaction with surrounding walls. It is this area that the following work focuses on, first by presenting current approaches and then presenting the approach adopted for this work.

Literature on spray modelling breaks down into a number of areas: the injection process, droplet hydrodynamics, wall impaction. Secondary topics include methods of describing and solving the spray equations, describing the local droplet density and defining how the spray contributes to the turbulent flow field.

A review by Gosman and Clerides [1997] discusses the state of the art on spray modelling, assessing the current accuracy achieved by the models and highlighting shortcomings, which focuses on the manner in which the spray is described and solved. Tatschl et al. [2002] also presents a review of spray modelling, but in this case focuses on the injection conditions and the governing mechanisms of spray formation.

In this work, the topic of turbulence modelling with spray interaction is not developed from the work of Beck and Watkins [2003a], though there are a number of fundamental studies on two-phase flow behaviour. Reveillon et al. [2002] presents a two-fluid spray dispersion model validated by the direct Navier-Stokes (DNS) solution of dispersed droplets in decaying statistically static fluid flow. A. Kaufmann et al. [2008] presents similar research on a decaying two-fluid field, but in this case the Eulerian dispersed field is represented by moments of the droplet PDF, which is a very similar approach used in this work.

1.2.1 Scope

The scope of a spray model is to represent the transportation and interaction of droplets within a carrier gas. The break-up of bulk liquid into primary droplets from the injection process and the adhesion of droplets on a surface are both associated to spray modelling so will need to be considered, but in themselves are not part of a spray model.

1.2.2 Phenomena

Regardless of how the spray is described, the model must account for key phenomena in order to simulate a spray adequately. A short discussion is given here about the main phenomena.

The physical processes can be categorised with reference to the droplets: Does the event involve only a single droplet or must there be multiple droplets involved for the process to take place? Does the event change the initial number of droplets? Does the event change the initial size of the droplets? These questions help to clarify the complexity of the process and its implementation.

Inter-phase Drag

This is the fundamental force acting between a given droplet and its surrounding gas, effecting only its momentum and the momentum of the surrounding gas. So long as their relative velocity magnitude is greater than zero, the effect of drag will retard one and accelerate the other, with equal force. For a range of droplet sizes, the drag force increases with the square of the radius

$$\vec{F}_{dr} = \frac{1}{2} C_d \rho \, 4\pi r^2 \parallel \vec{v} - \vec{v}_d \parallel (\vec{v} - \vec{v}_d) \tag{1.1}$$

whereas its momentum is a function of the cube of its radius

$$\vec{p} = \frac{4}{3} \pi r^3 \, \vec{v}_d \tag{1.2}$$

Assuming all other specific properties are equal, the larger droplets will experience a smaller change in momentum than the smaller droplets, resulting in a filtering of droplets.

Droplet Break-up

Similar to the inter-phase drag, this phenomena depends on a difference in velocity magnitude and is considered from the effect on a single droplet. Determination of whether a droplet breaks up is when shear forces acting on the surface of a droplet overcome the surface tension force holding the droplet together, resulting in production of a number of

smaller droplets. The onset of break-up occurs once its Weber number

$$We \equiv \frac{E_{\mathrm{kin}}}{E_{\mathrm{sur}}} = \frac{\rho\, v_d^2\, r}{\sigma} \qquad (1.3)$$

exceeds a critical value. Equation 1.3 shows that the larger droplets will break-up at much lower velocities than smaller droplets. When a given droplet exceeds the threshold, break-up occurs. The resultant number and sizes of the droplets depends on the kind of break-up undergone.

Inter-droplet Collisions

For a collision to take place, there are two fundamental requirements; that there is more than one droplet being considered and those droplets are heading towards each other. In addition, there are a number of possible outcomes of the collision; they could stick together, bounce off each other or momentarily coalesce then separate. Moreover, the resultant velocities may be quite dissimilar to the initial velocities. Often only coalescence is considered, effecting the resultant number and size of the droplets only.

1.2.3 Injection

The simplest choice available for prescribing inlet conditions for the spray is to assume that the liquid fuel has already been injected and that the bulk liquid has been broken up to such a degree that it is reasonable to assume the droplets form a smooth droplet size distribution at some point downstream of the nozzle. The conditions downstream of the nozzle are then used to describe the inlet conditions of the spray.

1.2.4 Impaction

Upon the spray impacting on a surface, the resultant effects need to be accounted for. Outcomes of impaction are defined in literature via correlations with experimental data [Obermeier and Chaves, 1991, Bai and Gosman, 1995] and generally are listed as rebound, splash, adhesion and boil. The rebounding process is defined such that on impaction, no droplets break-up. Splashing differs in that droplet break-up does occur, resulting in a

diminishing of its speed. Adhesion groups two processes, that of stick and spread. This outcome contributes to the formation of a liquid film on the piston surface.

1.2.5 Platform

Since the spray interacts with its surrounding gas, an appropriate platform for a spray model is a computational fluid dynamics methodology for simulating continuum flow. In this work the Finite Volume (FV) discretization of unstructured grids for modelling incompressible flow, as documented in Versteeg and Malalasekera [2006] and Ferziger and Perić [2002], is used as the patform, employing the turbulence model of Launder and Spalding [1974] for high Reynolds number flow.

1.2.6 Frame of Reference

The question of which frame of reference to choose for transporting spray droplets arises because there are two choices and both are sensible in the context of sprays but require very different numerical approaches to implement.

Intuitively, what happens to a given droplet after it is formed from the injection process is of interest, since it has a finite history (in the sense that once it comes to rest at a boundary it is no longer part of the spray) and the knowledge of that droplet history shows how it interacted with the continuum. The natural method then of referencing droplets would be in a Lagrangian frame. However, in reality, engineering practice regarding spray characterization is done through averaged quantities, such as the average droplet size within a given vicinity. This would indicate that the Eulerian frame of reference may be sufficient for spray simulation.

Lagrangian Coordinates

From following an individual droplet through a flow, one obtains the change of its properties only with respect to time. This method is the most powerful when dealing with sprays. Potentially, the exact details of a modelled spray can be obtained. However, given the number of droplets involved in a typical spray, individual droplets are never considered. Identical droplets are grouped into parcels, and these parcels are tracked. This

approach provides a good means for comparing different hydrodynamic models or the effects of different turbulent models since a great deal of information is available [Soriano and Rotondi, 2008].

Considering that the continuum is described in an Eulerian frame for nearly all computational methodologies, thus dealing with locally averaged quantities, the manner in which a tracked parcel interacts with the continuum within a given local volume needs to be assessed. If the volume is too small, the spray may be poorly represented, and if too large, the continuum flow will be poorly resolved. Whilst this is not a major issue with the method, it does mean that the injection region cannot be well resolved.

Eulerian Coordinates

The change in a property field rather than the change in a property of a particular particle represents the distinction between Eulerian and Lagrangian frames of reference. To describe a spray field bounded by the geometry of the domain would be counterintuitive since a spray does not necessarily cover the whole field and secondly, multiple sprays within the domain would require multiple sets of spray field properties, which may incur significant data storage requirements. However, this approach does have its advantages. Both the continuum and the spray would be discretized in the same manner. This removes the problems associated with interaction between the spray and the gas which arise from describing the two phases in different coordinate frames and simplifies its implementation. Furthermore, the method is suitable for concentrated sprays, such as the near nozzle region [Vujanovic et al., 2008].

1.2.7   Size Classification

Once the choice of reference has been made, a further choice is the manner in which the range of droplet sizes is to described.

Division

The most obvious choice is to divide up the droplet size range into a number of bins, transporting those bins separately. Quality of resolution of the local size distribution

then depends on the number of divisions made. This is the obvious approach to use if the Lagranian coordinate system is adopted. In addition, it can be used for the Eulerian coordinate system [Vujanovic et al., 2008] and has been developed by Moukalled and Darwish [2008] with the Multi-size Group model (MUSIG) and its heterogeneous variation.

Union

Treating the droplet size distribution in a holistic manner is a method commonly used when dealing with aerosols. The method is to transport a few moments of the underlying local droplet number distribution and from their appropriate ratios, determine local averaged quantities, such as mean radii. Here, this same idea can be used for sprays, whereby the main difference is that the moments of the spray are not carried by the surrounding gas, but penetrate it.

This method assumes that the underlying distribution can be determined by assuming its general form. Common forms used are the Log-Normal and the Gamma distribution, whereby their appropriate parameters are related to the transported moments.

1.3 Spray Modelling Methods

Currently there are four methods in use for modelling sprays. The methods are differentiated by the frame of reference of the spray and the droplet size classification.

1.3.1 Discrete Lagrangian Method

Parcels of identical droplets, P_d, are tracked as they propagate through the flow field [Bracco, 1985]. The number of droplets in each parcel, N_d, their diameter, D_d, are defined at the inlet condition, along with their initial velocity, $\vec{v}_d$.

$$P_d \equiv \{\vec{x}_d,\ \vec{v}_d,\ D_d,\ N_d\} \tag{1.4}$$

Each parcel represents a segment of the initial droplet number density. For adequate representation of the distribution in a given region, sufficient parcels must be present. This method is the most obvious manner of modelling sprays and is the most flexible.

Crossing sprays and impacting sprays require no modifications of the model methodology and the accuracy of the method can be improved by refining the segmentation of the inlet distribution. However, the method is relatively expensive since the number of parcels tracked increases with injection duration and can reach the order of 10^4.

1.3.2   Discrete Eulerian Method

Again, the droplet number distribution is segmented into a number of identically sized droplets. The quantity (liquid volume fraction) of each segment and its momentum is transported. Since the droplet size of each segment is defined at inlet, the droplet number can be recovered. The method is readily implemented in a typical fluid flow solver, making use of existing subroutines since both the spray and the fluid are now discretized in the same manner. Also, the expense of the method is independent of injection duration. The number of segments transported effects the accuracy of the represented distribution and the computational workload. Typically five to forty segments of the distribution are transported.

1.3.3   Holistic Quadrature Eulerian Method

This method and the following method transport spray properties in a similar manner to that of the Discrete Eulerian method, though what they transport is somewhat different. These two methods transport properties representing the whole distribution, effectively making the computational work independent of segmentation resolution. The manner in which these two methods differ is how the droplet size distribution is represented. This method represents the distribution as a summation of Dirac delta functions (Eq. 1.5) [Marchisio and Fox, 2005]

$$n(r) = \sum_{i=k}^{N} \omega_k \, \delta\left[r - r_k\right] \tag{1.5}$$

whose weights, ω_k, and abscissas, r_k, are determined by moments of the entire distribution (Eq. 1.6) using the Product-Difference algorithm [McGraw, 1997].

$$\mu_i = \int_r n(r) \, r^i \, \mathrm{d}r \approx \sum_{k=1}^{N} \omega_k \, r_k^i \tag{1.6}$$

28

The method has undergone rapid development in the last eight years and has been shown to be stable, accurate and capable of modelling flows such as crossing sprays and spray impaction on a surface [Desjardins et al., 2006]. Approximating the distribution as a sum of Dirac functions (typically three to four [Fox, 2008]) does however present concerns about how accurately spray phenomena is represented across the whole distribution.

1.3.4   Holistic Continuous Eulerian Method

Instead of employing Dirac delta functions to represent the droplet size distribution, a continuous function is used [Beck and Watkins, 2003a]. This approach ensures that the distribution is always properly represented and the effects on droplets of all sizes is considered [Beck and Watkins, 2002]. This method then would appear to be the best compromise between computational efficiency and spray representation. In practice, the method has lacked stability [Yue and Watkins, 2004], whereby this instability is related to both the recovery of the continuous distribution and the representation of hydrodynamic processes. This method has received the least development, though with recent work on recovering the underlying distribution [Tagliani, 1999, Woodbury, 2004, John et al., 2007], improvements of stability may be achieved.

1.4   Project Aim

The intention of this work is to develop the holistic continuous Eulerian spray model, first presented by Beck [2000]. The general methodology is developed in Beck and Watkins [2003a], hydrodynamic models for collisions, break-up and drag in Beck and Watkins [2002] and evaporation and heat transfer models in Beck and Watkins [2003b].

The above referenced work, whilst successful, did not overcome certain important problems of the model, leaving it in a substandard state for implementation into a general CFD algorithm. The problems that were either not addressed or inadequately dealt with are

1. Assuming the underlying droplet size distribution can be adequately defined by a single independent variable.

2. Assuming that all droplets within a given local volume are travelling at identical speeds.

3. Using the structured nature of the grid to resolve the spray edge.

4. Only using first-order differencing schemes to approximate convection terms in the spray equations.

5. Only using first-order temporal differencing schemes for the spray equations.

The first part of this work aims to address (or re-address) these issues employing new methods from literature which may help solve these problems. Briefly considering each point made, this work proposes to

1. Consider a distribution based on approximately four independent variables relating to the mean, variance, skewness and kurtosis.

2. Assume a non-uniform velocity-radius function to describe the local droplet velocity.

3. Develop the method on an unstructured grid to aid local refinement and be able to consider a range of configurations, finding alternative means for resolving the spray edge.

4. Employ higher order convection schemes which minimize the occurrence of unphysical solutions.

5. Implement higher order temporal schemes which allow for relatively large time steps.

The second part of this work is to implement a wall impaction model as an extension of the spray model which considers the different possible outcomes of impaction as independent parts of the spray transportation. Whilst a wall impaction model was developed for this spray model [Lemini and Watkins, 2002], its method was to modify the spray equations in the near wall region to reflect the outcomes of droplets impacting on the wall. The model, though considering the different impaction outcomes, provided no means for these splashing or rebounding droplets to develop independently of the incoming spray.

No references to evaporation and heat transfer models will be made in this work as it is already well developed [Watkins, 2006]. Wall impaction does introduce additional conditions for the heat transfer model, but is a consideration beyond the scope of this work.

Finally, the hydrodynamics models (Drag, break-up and collision) will be revised in order to improve the implementation and/or the accuracy of the models since they had been a cause of instability in the work of Yue and Watkins [2004].

1.4.1 Code Development

In order to crray out the research, a new code platform is required. To date, the research on spray modelling has been performed on a structured, othogonal-type CFD code, written in Fortran 77. To implement the above aims of the research, a code which can support unstructured meshes is required. Also, a means of cleanly setting up and solving many similar partial differential equations is required for the transportation of moments of the modelled spray.

No open-source CFD code known to the author seemed like a good candidate to use as a platform for implementing the spray model into it. As a result, a new code was written by the author. The structure and features of the code are discussed in detail in the second chapter; all the closure methods, spray hydrodynamics, boundary conditions, source terms and discretization methods presented there are implemented.

1.4.2 Project Content

The following work presents the implementation of many existing models into a Eulerian-based spray simulation program. Droplet break-up, collision and drag models are implemented directly from literature, in addition to droplet wall impaction conditions and their outcomes.

A review on the methods for the construction of probability density functions for approximating the local droplet size distribution is presented, detailing the construction and performance of the (more sophisticated) models. The models are taken from literature, though variations on the algorithms for constructing the Splines and Maximum entropy methods are presented. No explicit documentation for the Laguerre PDF method was found in literature, but it is assumed that such an approach is not original to this work.

Droplet velocity profiles are documented here for the first time. Whilst the presented profiles are relatively simple, the effect such approximations have on the spray is considerable and is considered to be at present, the most important detail of the spray model. Implementation of the injection conditions used in this work are also original, though are not ideal and are not to be considered as an area of progress in this field. Better injection models exist, though they are not used here due to time constraints on implementing such models (for example, that by Moreau et al. [2004]).

Certain aspects of the numerical model are brought into focus in this work, with the aim of implementing at least second order accurate spatial and temporal schemes. No original schemes are presented, though for the convection schemes, their implementation is revisited and amended for the spray model, making their use, for the first time, possible.

Since the spray model potentially involves the solution of many associated transport equations, this work presents in detail the framework of the software written for simulating the spray. The approach presented is to construct a strongly hierachical structure to the storage of data. This method lends itself to object-oriented programming, though was not the paradigm used. The versatility of the structure is demonstrated by the fact that the spray model could simulate wall impaction simulations involving unlimited sets coupled transport equations (in the wall impaction case 24 properties were transported), with a code written in 5500 lines.

Chapter 2

Method

Modelling the spray and its associated phenomena is detailed, boundary conditions are specified and techniques for numerical implementation are discussed. The construction methods of both the droplet size distribution and the droplet velocity profile are presented, completing the spray model description.

2.1 Moments of a Continuous Distribution

2.1.1 Moments about the Origin

The simplest definition of moments of a continuous distribution, $\phi(r)$, is the moments about its origin, defined as

$$\mu_i = \mu_0 \int_r \phi(r) \, r^i \, \mathrm{d}r \tag{2.1}$$

whereby the first moment (when $i = 0$) simply returns the integral of the distribution. If the distribution is a probability density function, $\mu_0 = 1$; for a number density, the total number per unit volume; and for the volume density, the sum of the individual volumes per unit volume, etc.

Assuming the distribution to represent the range of (spherical) droplet sizes within a given volume, the first four moments of the distribution have physical interpretations. From Table 2.1, the volume fraction occupied by the droplets is known, hence the volume fraction of the surrounding gas is simply $1 - \frac{4}{3}\pi \, \mu_3$.

Table 2.1: Interpretation of moments

Quantity (per unit volume)	Moment Relation
Total number of droplets	μ_0
Sum of the radii	μ_1
Sum of the surface areas	$4\pi\,\mu_2$
Sum of the volumes	$\frac{4}{3}\pi\,\mu_3$

In the case where the distribution is not a probability density, moments are often normalized by the constant, μ_0, giving the normalized moments about the origin

$$\hat{\mu}_i = \frac{\mu_i}{\mu_0} \tag{2.2}$$

Moment ratios are of interest, providing definitions of different kinds of mean values based on the moments. This is defined as

$$r_{ji} = \left(\frac{\mu_j}{\mu_i}\right)^{\frac{1}{j-i}} \tag{2.3}$$

A common moment ratio in literature is the Sauter mean radius, r_{32}, (SMR) which will be used for characterizing the spray.

2.1.2 Moments about the Mean

From the moments about the origin, moments about the mean (or centralized moments) are defined as

$$\mu_i' = \int_r (r - r_{10})^i \, \phi(r) \, \mathrm{d}r \tag{2.4}$$

whereby the first central moment (when $i = 1$) is zero. The second moment (Eq. (2.6)) defines the variance of the distribution and the third and fourth moments (Eq. (2.7 -

2.8)) are used to define the standardized moments.

$$\mu'_1 = 0 \tag{2.5}$$

$$\mu'_2 = \hat{\mu}_2 - r_{10}^2 \tag{2.6}$$

$$\mu'_3 = \hat{\mu}_3 - 3r_{10}\hat{\mu}_2 + 2r_{10}^3 \tag{2.7}$$

$$\mu'_4 = \hat{\mu}_4 - 4r_{10}\hat{\mu}_3 + 6r_{10}^2\hat{\mu}_2 - 3r_{10}^4 \tag{2.8}$$

2.1.3 Standardized Moments

To calculate skewness and kurtosis of the distribution, the standardized moments are required. These moments are defined as

$$\mu''_i = \frac{\mu'_i}{\sigma^i} \tag{2.9}$$

where the standard deviation, $\sigma = \sqrt{\mu'_2}$. From the definition of standard deviation, the condition

$$\mu'_2 > 0 \tag{2.10}$$

is imposed. As this (the variance) tends to zero, the shape of the distribution will become more peaked. Skewness and kurtosis are defined as

$$\gamma_1 = \mu''_3 \tag{2.11}$$

$$\gamma_2 = \mu''_4 - 3 \tag{2.12}$$

The above explanation shows how the common parameters for characterizing a distribution relate to the primary definition in Eq. (2.1) of the distribution's moments. It also provides an indication of how many moments (about the origin) are required to adequately describe a distribution; the first five moments, $\mu_0 - \mu_4$, are required to calculate the mean, variance, skewness and kurtosis of a distribution.

No limits for the moments about the mean are imposed, except for Eq. (2.10). However, in practice, additional limits are required on the moments to ensure the representation of sensible distributions.

2.2   Distribution Construction

Moments of a continuous distribution has been discussed without mentioning the form of the distribution itself, assuming it is already somehow known. In the spray model of Beck and Watkins [2003a], the distribution is not initially known and a means of determining the underlying probability density function is required given a finite set of its moments. If this given set of moments does not include the first moment, μ_0, this has to be determined first.

This kind of problem is classified as an Inverse problem and are generally ill-posed; usually being deficient on one or more of the conditions of a well-posed problem (that of existence, uniqueness and stability) and as a result the computation of the solution is ill-conditioned [John et al., 2007].

A number of methods are available for prescribing the general form of a probability density function (PDF), such as assuming an a-priori form [Yue and Watkins, 2004, John et al., 2007], using polynomial fitting [John et al., 2007, Talenti, 1987] or the Maximum Entropy Formalism [Ahmadi and Sellens, 1993, Woodbury, 2004]. Each method has different characteristics but none of them possesses all the qualities of a well-posed solution. Whichever method is used, the specific form is determined through knowledge of the moments.

This discussion presents five methods of solving this inverse problem, though none of them suitably combine the requirements of being computationally inexpensive and robust, accurate and with minimum constraints on the shape of the distribution. In addition, only one method provides a means for calculating μ_0 from the available moments before the distribution is solved.

2.2.1   Normalization and Limits

For some closure methods, the moments require normalizing. This is done either to ensure the distribution is between certain limits such as the interval of 0 to 1, or more generally, to reduce the numerical difference between moments. In either case, a normalizing length scale is required. Using the ratio of any pair of successive moments a normalization radius

r_n can be defined,

$$r_n = \frac{\mu_{i+1}}{\mu_i}. \tag{2.13}$$

This radius can then be used to provide a sensible range in which the upper limit lies. From numerical tests, the upper limit can be assumed to lie in the range $r_n < r_u < 3.5\,r_n$ (for $i = 2$) and the lower limit, r_l, set to zero. In two of the methods presented where the limits are required [John et al., 2007, Talenti, 1987], accuracy of the estimated interval significantly effects the accuracy of the resulting distribution. To obtain accurate limits (only the upper limit is corrected), an iterative procedure is required.

Upon establishing a normalizing length scale, r_n, and before the closure method is called, linear normalization of the moments is performed by substition of $x = \frac{r}{r_n}$ into Eq. (2.1), giving

$$\frac{\mu_i}{\mu_0\, r_n^{1+i}} = \int_{r_n x} \phi(r_n x)\, x^i \, \mathrm{d}x \tag{2.14}$$

2.2.2 Maximum Entropy Distribution

The probability density function is approximated as [Woodbury, 2004]

$$\phi(r) \approx p(r) \exp\left[-\sum_{i=0}^{N-1} \lambda_i r^i \right] \tag{2.15}$$

where N is the number of moments available and $\lambda_0 \ldots \lambda_{N-1}$ are the Lagrangian multipliers and $p(r)$ is the 'preconditioning' approximate distribution. Different possible forms of $p(r)$ are listed in Table 2.2.

Table 2.2: Approximate distribution functions

Type	$p(r)$
Uniform	1
Mean value	r_{10}
Exponential	$\frac{1}{r_{10}} \exp\left(-\frac{r}{r_{10}} \right)$
Rayleigh	$\frac{r}{s^2} \exp\left(-0.5\frac{r^2}{s^2} \right)$, where $s = r_{10}\sqrt{0.5\pi}$
Beck [2000]	$16\frac{r}{r_{32}^2} \exp\left(-4\frac{r}{r_{32}} \right)$

Substituting Eq. (2.15) into Eq. (2.1) provides N equations with N unknown multi-

pliers (Eq. (2.16)).

$$f_j(\underline{\lambda}) = \int_r r^j \, p(r) \exp\left[-\sum_{i=0}^{N-1} \lambda_i r^i\right] \mathrm{d}r = \frac{\mu_j}{\mu_0} \tag{2.16}$$

In order to solve the set of equations, $f_j(\underline{\lambda})$ is approximated as a first-order Taylor series, using the general form for functions with several arguments;

$$f_j(\underline{\lambda}) = \sum_{k=0} \frac{1}{k!} \frac{\mathrm{d}^k}{\mathrm{d}\underline{\lambda}^k}[f_j(\underline{\lambda}^0)] \cdot (\underline{\lambda} - \underline{\lambda}^0)^k \tag{2.17}$$

$$\approx f_j(\underline{\lambda}^0) + \frac{\mathrm{d}}{\mathrm{d}\underline{\lambda}}[f_j(\underline{\lambda}^0)] \cdot (\underline{\lambda} - \underline{\lambda}^0), \tag{2.18}$$

where the gradient of $f_j(\underline{\lambda})$ is

$$\frac{\mathrm{d}}{\mathrm{d}\lambda_k}[f_j(\lambda_k)] = -\int_r r^k r^j \, p(r) \exp\left[-\sum_{i=0}^{N-1} \lambda_i r^i\right] \mathrm{d}r. \tag{2.19}$$

Rearranging Eq. (2.18) leads to a system of linear equations. Before the solution to these equations can be formed, the gradients must be calculated by performing numerical integration. Both tasks can be accomplished using standard mathematical library packages. Initial multipliers, $\underline{\lambda}^0$, are typically set to zero.

2.2.3 Splines Distribution

This method considers the distribution as a summation of N_{spl} splines of degree N_{deg}, where each spline is defined in the interval $[r_i, \ r_{i+1}]$, as [John et al., 2007]

$$\phi(r) \approx \sum_{i=1}^{N_{spl}} \sum_{j=0}^{N_{deg}} \lambda_{i,j}(r - r_i)^j \tag{2.20}$$

whereby the number of splines is dependent on the number of available moments, N_μ, as

$$N_{spl} = N_{deg} + N_\mu. \tag{2.21}$$

38

The degree of the splines is optional, but cubic splines are usually employed. Boundary conditions at r_1 and $r_{N_{spl}+1}$ and differentiability conditions at internal nodes (r_i, $i = 2, \ldots N_{spl}$) provide $(N_{deg}+1)N_{spl} - N_\mu$ equations with $(N_{deg}+1)N_{spl}$ unknowns, $\lambda_{i,j}$. The additional equations are derived from substitution of Eq. (2.20) into Eq. (2.1), which can be integrated analytically. Here, the integrand is expanded using the binomial theorem, resulting in

$$\int_{r_i}^{r_{i+1}} (r - r_i)^j \mathrm{d}r = \sum_{k=0}^{j} \binom{j}{k} (r_{i+1}^{j+k+1} - r_i^{j+k+1}) (-r_i)^{\frac{j-k}{j+k+1}}. \tag{2.22}$$

From the equations a system of linear equations can be written. With increasing the number of moments used, the condition number of the matrix formed rapidly tends towards infinity. In order to obtain a sensible solution to the system of equations, singular value decomposition is required. This approach provides a means of ignoring the small singular values, which may be regarded as numerical noise. In order to ensure that the singular values which are disregarded do not result in discontinuities in the resulting distribution, all the equations relating to the nodal conditions are numerically weakened by the constant ω^l, where l is the order of the differentiability condition.

To produce an physically sensible and accurate distribution, both the limits of the distribution and the singular value cut-off need to be determined. The former is done iteratively by examining the tails of the distribution. The later can either be iteratively increased until the distribution is physically sensible or the cut-off can be found non-iteratively by inspection of the singular values. If the first choice is adopted then the solution scheme becomes a nested iterative scheme, whilst the latter method avoids the nested iteration, but may not produce an equally accurate result. Here, the non-iterative approach is taken.

2.2.4 Laguerre Distribution

The generalized Laguerre polynomial of degree i and order k is given by

$$L_i^k(r) = \frac{r^k e^r}{i!} \frac{\mathrm{d}^i}{\mathrm{d}r^i}(r^{i+k} e^{-r}) = \sum_{j=0}^{i} \frac{(-1)^j}{j!} \binom{i+k}{i-j} r^j \tag{2.23}$$

and is orthogonal over the interval $[0, \infty]$ with respect to the weighting function $w_k(r) = r^k e^{-r}$,

$$\int_0^\infty w_k(r) L_i^k(r) L_j^k(r) \mathrm{d}r = \frac{(j+k)!}{j!} \delta_{ij} \tag{2.24}$$

Since the polynomials are orthogonal over this interval, the normalization of the moments needs to be such that the normalized radius scales well with the Laguerre polynomial coefficients. From considering the function $x \exp(-x)$, the upper limit can be approximated as lying between $15 - 20$.

By exploiting the orthogonality property in Eq. (2.24), the probability density function can be defined as

$$\phi(r) \approx w_k(r) \sum_{i=0}^{N_\mu - 1} \lambda_i^k L_i^k(r) \tag{2.25}$$

Substituting Eq. (2.25) into Eq. (2.24) provides the equation for calculating the coefficients λ_i^k as a function of the available moments,

$$\lambda_i^k = \sum_{j=0}^{i} \frac{(-1)^j}{j!} \binom{i+k}{i-j} \mu_j \tag{2.26}$$

It is worth noting that Eq. (2.23) and Eq. (2.26) have exactly the same form, making the implementation of the method very simple.

2.2.5   Legendre Distribution

This method is based on shifted Legendre polynomials for the interval $[0, 1]$, and is given by [Talenti, 1987]

$$L_i(r) = \frac{1}{i!} \frac{\mathrm{d}^i}{\mathrm{d}r^i}((r^2 - r)^i) = \sum_{j=0}^{i} (-1)^j \binom{i}{j} \binom{i+j}{j} r^j \tag{2.27}$$

and is orthogonal, giving the condition

$$\int_0^1 L_i(r) L_j(r) \mathrm{d}r = \frac{1}{2j-1} \delta_{ij}. \tag{2.28}$$

The probability density function is then defined as

$$\phi(r) \approx \sum_{i=0}^{N_\mu - 1} (2i+1)\, \lambda_i\, L_i(r) \tag{2.29}$$

where

$$\lambda_i = \sum_{j=0}^{i} (-1)^j \binom{i}{j} \binom{i+j}{j} \mu_j. \tag{2.30}$$

2.2.6 A-priori Distributions

There are a number of possible distributions which could be assumed to represent the underlying probability density function, such as the Log-Normal, Gamma, Beta and the Rayleigh distributions. Here, only the Gamma distribution will be developed.

The Gamma distribution is defined as

$$\phi(r) = \frac{r^{k-1}}{\Gamma(k)\theta^k} \exp\left(-\frac{r}{\theta}\right), \tag{2.31}$$

where

$$\Gamma(k)\theta^k = 1 \tag{2.32}$$

by definition. Combining Eq. (2.31) and Eq. (2.1) gives

$$\begin{aligned}
\frac{\Gamma(k)\theta^k \mu_j}{\mu_0} &= \int_0^\infty r^{k-1+j} \exp\left(-\frac{r}{\theta}\right) \mathrm{d}r \\
&= \left[-\theta r^{k-1+j} \exp\left(-\frac{r}{\theta}\right) \right]_0^\infty + \theta(k-1+j) \int_0^\infty r^{k-2+j} \exp\left(-\frac{r}{\theta}\right) \mathrm{d}r \\
&\qquad\qquad\qquad\qquad\qquad\qquad = \frac{\theta(k-1+j)\mu_{j-1}}{\mu_0},
\end{aligned} \tag{2.33}$$

which simplifies to

$$\frac{\mu_{j+1}}{\mu_j} = \theta(k+j). \tag{2.34}$$

From Eq. (2.34), the parameters can be related to three consecutive moments by

$$k = \frac{j\left(1 - \frac{\mu_{j+2}\mu_j}{\mu_{j+1}^2}\right) + 1}{\frac{\mu_{j+2}\mu_j}{\mu_{j+1}^2} - 1} \tag{2.35}$$

$$\theta = \frac{\mu_{j+1}}{\mu_j(k-j)}. \tag{2.36}$$

To ensure the denominator of the above equation remains unconditionally positive, limits are set on parameter k such that $1.5 < k < 20$. Moments of the Gamma distribution can be calculated by

$$\mu_\alpha|_{r_l}^{r_u} = \mu_0\,\theta^\alpha\frac{\Gamma(k+\alpha)}{\Gamma(k)}\left[\gamma\left(k+\alpha,\frac{r_u}{\theta}\right) - \gamma\left(k+\alpha,\frac{r_l}{\theta}\right)\right], \tag{2.37}$$

where $\gamma(k,x)$ is the lower incomplete Gamma function.

2.2.7 Numerical Integration

Once the probability density function is constructed, moments of that distribution may be required. For a-priori distributions, moments are obtained as functions of their parameters (Eq. (2.37)). For all other methods, the distribution must be integrated numerically.

Supposing that a group of terms are functions of a single PDF and require integrating between different limits and to different orders (such as the break-up terms in Beck and Watkins [2002]). To evaluate these terms the normal procedure would be to call a numerical integration subroutine for each moment calculation.

An alternative approach presented here is to perform the numerical integration once, calculating all integer moments covering the order range and limits of the required moments in a single sweep of the underlying distribution.
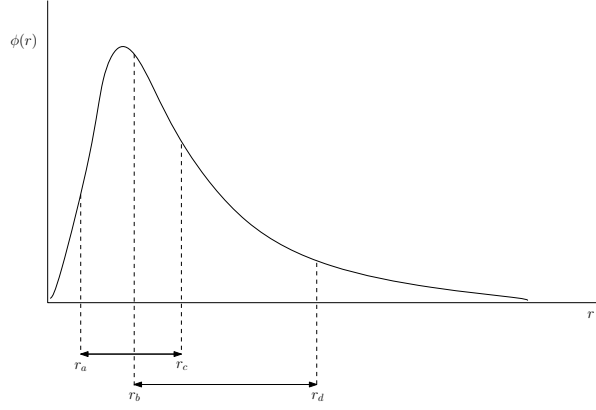
Figure 2.1: Integration of a PDF between sets of limits

Coordinates of the constructed PDF (Fig. 2.1) are stored as links on a doubly linked list (Fig. 2.2).
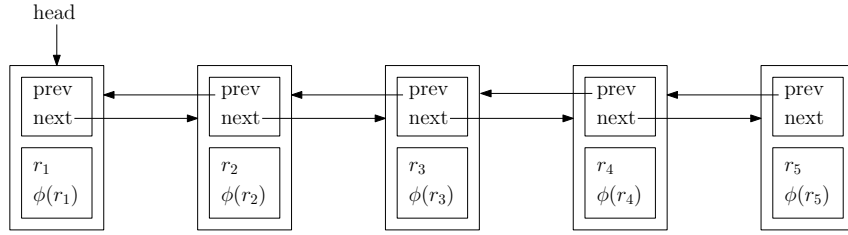
Figure 2.2: Construction of integration linked list

Pairs of integration limits are then inserted into the linked list at the appropriate position (Fig. 2.3) and the distribution ordinates ($\phi(r_a)$ and $\phi(r_c)$) are obtained by interpolation, forming a single chain of distribution coordinates. A pass is then made along the list, performing the elemental integration between the current link and the previous link and summating the elemental integrations between the pairs of limits.
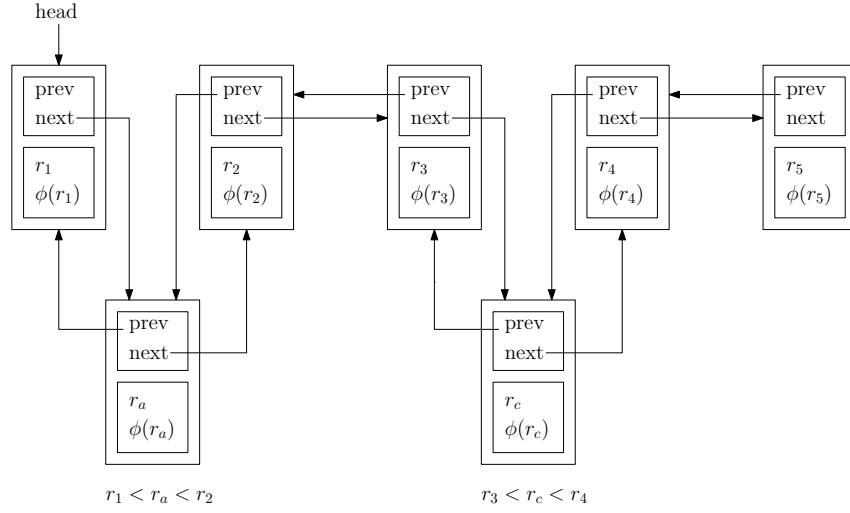
Figure 2.3: Insertion of limits to the PDF list

For example, two moments are required: $\mu_{2.35} \mid_{r_a}^{r_c}$ and $\mu_{0.78} \mid_{r_b}^{r_d}$ (Fig. 2.1). The information then sent to the integration subroutine is *calculate moments $\mu_0, \ldots \mu_3$ between the limits $r_a - r_c$ and $r_b - r_d$*, which would result in an output of eight moments grouped into two sets (μ_0 to μ_3 between r_a and r_c and μ_0 to μ_3 between r_b and r_d). The orders from 0 to 3 for the moments are requested since they span the order range of the required moments. To calculate the actual moments required, interpolation is performed between the nearest pair of integer moments.

2.2.8 Interpolation and Extrapolation

Geometric Interpolation

Assuming consecutive integer moments are available, determining non-integer moments within the range of the available moments can be approximated by

$$\int \phi(r) r^n r^{0.m} \mathrm{d}r \approx \left(\int \phi(r) r^n \mathrm{d}r \right)^{1-0.m} \left(\int \phi(r) r^{n+1} \mathrm{d}r \right)^{0.m} \tag{2.38}$$

44

Quadrature Method

Approximating the integral of Eq. (2.4) by an N-point quadrature, a function for determining any order moment is obtained, as

$$\int \phi(r) r^\alpha \mathrm{d}r \approx \sum_{i=1}^{N} r_i^\alpha w_i \qquad (2.39)$$

where r_i are the weights and w_i the abscissas, which are solved using the Product-Difference algorithm [McGraw, 1997].

2.3 Moment Averaged Properties

The manner in which intensive properties of the droplets, such as temperature and velocity, vary with droplet size may be captured in a similar way to the moments capturing the variation of the underlying distribution. By averaging such a property, $\psi(r)$, over the probability density function, moment averaged quantities, Ψ_i, are obtained by

$$
\Psi_i \; = \; \frac{\int_r \phi(r)\, r^i\, \psi(r)\, \mathrm{d}r}{\int_r \phi(r)\, r^i\, \mathrm{d}r} \tag{2.40}
$$

$$
= \; \frac{\mu_0}{\mu_i} \int_r \phi(r)\, r^i\, \psi(r)\, \mathrm{d}r \tag{2.41}
$$

Tagliani [2001] showed that whilst the determination of the probability density function in Eq. (2.1) is ill-conditioned, determination of functionals like $\psi(r)$ in Eq. (2.41) is well conditioned and can be reliably determined, assuming that Ψ_i and $\phi(r)$ are known.

2.3.1 Stabilized Closure

Woodbury [2004] makes use of the observation by Tagliani [2001] above, to aid the solution of the underlying distribution from the knowledge of the moments by defining the distribution, $\phi(r)$ to be the product of a known approximation to $\phi(r)$ and a second distribution, to be determined, i.e.

$$
\phi(r) \simeq p(r)\, \phi(r)^* \tag{2.42}
$$

where $p(r)$ is the known approximation. The role of $p(r)$ is very much analogous to the role of a preconditioning matrix in solving a system of linear equations: if $p(r) = 1$, the initial problem is recovered and so is of no benefit, but if $p(r)$ takes on a useful form, for example, a Gaussian distribution, the convergence of $\phi(r)^*$ is stabilized and accelerated.

2.3.2 Droplet Velocity Profile

Two general forms for approximating the droplet velocity profile are proposed in this work (a third is presented in Appendix B). The first profile (Eq. (2.43)) assumes that for small

droplets, their velocity, $\vec{v}_d$, increases rapidly from the surrounding gas velocity, $\vec{v}$, with increasing droplet radius and for large droplets, velocity increases slowly (for $0 < b < 1$).

$$\vec{v}_d(r) = \vec{v} + \vec{a}_i r^b \tag{2.43}$$

The coefficient, $\vec{a}_i$, is determined by substituting Eq. (2.43) into Eq. (2.41), giving

$$\vec{a}_i = (\vec{V}_{d,i} - \vec{v}) \frac{\mu_i}{\mu_{i+b}} \tag{2.44}$$

where $\vec{V}_{d,i}$ is the ith moment averaged velocity.

The second method is to not take into account the surrounding gas velocity, but make use of all the available moment averaged velocities to obtain a functional form for the droplet velocity variation. The simplest form is to consider an Nth degree polynomial, where there are $N + 1$ moment averaged velocities available. This is certainly not the best form (potentially forming an ill-conditioned problem for high order polynomials), but serves as a starting point for forming non-linear functions from a complete set of moment-averaged data.

$$\vec{v}_d(r) = \sum_{j=0}^{N} \vec{a}_j r^j \tag{2.45}$$

Substituting Eq. (2.45) into Eq. (2.41) results in a system of linear equations for solving the unknown coefficients, $\vec{a}_j$.

A variation on this method is to define the constant, a_0, as a function of the continuum phase velocity and the lowest available moment averaged velocity, such as

$$\vec{a}_0 = \lambda \vec{v} + (1 - \lambda) \vec{V}_{d,0} \tag{2.46}$$

where $0 < \lambda < 1$ and change the summation in Eq. (2.45) to $j = 1, \ldots N+1$. Coefficients of Eq. (2.46) are solved in a similar manner as above.

2.4 Transport Equations

The derivation of the moment and moment-averaged momentum conservation equations for the spray model begins with stating the derivative of a fluid particle (droplet) property, ϕ, per unit volume with respect to time which is travelling at velocity $\vec{v}_d$ and has a density ρ_d [Versteeg and Malalasekera, 2006]

$$\rho_d \frac{\mathrm{d}(\phi)}{\mathrm{d}t} = \rho_d \left(\frac{\partial}{\partial t}(\phi) + \vec{v}_d \cdot \mathrm{grad}\phi \right) \tag{2.47}$$

This represents the change of the droplet property as it is being followed along its pathline. However, in the context of the spray model, the quantities being transported will be integral quantities, i.e. the moments are integrals of the droplet size distribution within a given region and are used to represent averaged quantities, such as the local SMR, which indicates that Eq. (2.47) would be better represented in an Eulerian manner, as dicussed in Section (1.2.6). The relationship between Eq. (2.47) and the equivalent Eulerian description is [Versteeg and Malalasekera, 2006]

$$\rho_d \left(\frac{\partial}{\partial t}(\phi) + \vec{v}_d \cdot \mathrm{grad}\phi \right) = \frac{\partial}{\partial t}(\rho_d \phi) + \mathrm{div}(\rho_d \vec{v}_d \phi) - \phi \left(\frac{\partial}{\partial t}(\rho_d) + \mathrm{div}(\rho_d \vec{v}_d) \right) \tag{2.48}$$

Casting the above equation into the generalised form for a transported property and applying Guass' theorem, the template transport equation becomes (with the inclusion of source terms)

$$\frac{\partial}{\partial t} \int_\Omega \rho_d \phi \, \mathrm{d}\Omega + \int_S \rho_d [\vec{v}_d \cdot \vec{n}] \, \phi \, \mathrm{d}S - \phi \left(\frac{\partial}{\partial t} \int_\Omega \rho_d \, \mathrm{d}\Omega + \int_S \rho_d \, [\vec{v}_d \cdot \vec{n}] \, \mathrm{d}S \right) = \int_\Omega q_\phi \, \mathrm{d}\Omega \tag{2.49}$$

where q_ϕ represents any additional contributions to the rate of change of the transported property.

In order to arrive at the governing equations of the spray model, the equations for a moment about the origin (Eq. (2.1)) and a moment-averaged property (Eq. (2.41)) are introduced to Eq. (2.49), forming two conservation equations: when ϕ represents a moment of the PDF and when ϕ represents a moment-averaged velocity of the PDF.

2.4.1 Continuity

Replacing $\vec{v}_d$ with the moment-averaged velocity and ϕ with the transported moment, μ_i in Eq. (2.49), the moment continuity equation becomes (N.B. $\phi(r)$ is the PDF)

$$\frac{\partial}{\partial t} \int_\Omega \left\{ \mu_0 \int_r \phi(r) r^i \mathrm{d}r \right\} \mathrm{d}\Omega + \int_S \left[\left\{ \frac{\mu_0}{\mu_i} \int_r \phi(r) r^i \vec{v}_d(r) \, \mathrm{d}r \right\} \cdot \vec{n} \right] \left\{ \mu_0 \int_r \phi(r) r^i \mathrm{d}r \right\} \mathrm{d}S$$

$$= \int_\Omega \left\{ \mu_0 \int_r \phi(r) q_i(r) \mathrm{d}r \right\} \mathrm{d}\Omega \quad (2.50)$$

Since heat transfer is not considered, Eq. (2.49) is divided through by ρ_d (see Watkins [2006] for modifications when considering heat transfer). The third term in Eq. (2.49) is equal to zero by virtue of moment conservation.

The resulting transport equation, upon integration over all droplets, represents the conservation of moments (Eq. (2.51)) and is analogous to the mass conservation (per unit volume) of the continuum phase. The moments represent quantity (per unit volume) and those moments are convected by their moment-averaged velocity.

$$\frac{\partial}{\partial t} \int_\Omega \mu_i \, \mathrm{d}\Omega + \int_S [\vec{V}_{d,i} \cdot \vec{n}] \, \mu_i \, \mathrm{d}S = \int_\Omega q_{\mu_i} \mathrm{d}\Omega \quad (2.51)$$

2.4.2 Momentum

The moment-averaged momentum transport equation (Eq. 2.52) has its respective moment as the coefficient since the moment represents quantity per unity volume. The derivation of this follows the same method as above.

$$\frac{\partial}{\partial t} \int_\Omega \mu_i \, \vec{V}_{d,i} \, \mathrm{d}\Omega + \int_S \mu_i [\vec{V}_{d,i} \cdot \vec{n}] \, \vec{V}_{d,i} \, \mathrm{d}S$$

$$- \vec{V}_{d,i} \left(\frac{\partial}{\partial t} \int_\Omega \mu_i \, \mathrm{d}\Omega + \int_S [\vec{V}_{d,i} \cdot \vec{n}] \, \mu_i \, \mathrm{d}S \right) = \int_\Omega q_{\vec{V}_{d,i}} \, \mathrm{d}\Omega \quad (2.52)$$

Here it is noted that although the above transport equations are written for a particular moment, i, one moment cannot be considered separately from the set of transported moments corresponding to the same underlying distribution. Within a given region, all related transported moments must co-exist, otherwise none of the moments must exist.

2.4.3 Liquid Film

Since there is a possibility of droplets sticking to the wall upon impaction, the resulting formation of a liquid film must be accounted for. This film does not need to be transported (the convection term may be omitted) so long as the near wall control-volumes are sufficiently large to prevent unphysical liquid volume fractions. The liquid film volume fraction equation is then defined as

$$\frac{\partial}{\partial t} \int_{\Omega} \theta \, \mathrm{d}\Omega + \int_{S} [\vec{v}_{\theta} \cdot \vec{n}] \, \theta \, \mathrm{d}S = \int_{\Omega} q_{\theta} \, \mathrm{d}\Omega \tag{2.53}$$

In the methodology presented, the velocity of the film, $\vec{v}_{\theta}$, will be assumed to be zero, effectively grouping together the adhesing and spreading droplets resulting from impaction of the spray. Details on extending the liquid film modelling can be found in Stanton and Rutland [1998].

2.5 Physical Processes

2.5.1 Inter-phase Drag

The rate of change of momentum of a droplet equals the sum of the forces acting on the droplet

$$m_d \frac{\mathrm{D}\vec{v}_d}{\mathrm{D}t} = \sum \vec{F}_d \tag{2.54}$$

The drag force, $\vec{F}_{dr}$, is the dominant force acting on a droplet and is given by [Crowe et al., 1998]

$$\vec{F}_{dr} = \frac{1}{2} C_d \rho A_d \parallel \vec{v} - \vec{v}_d \parallel (\vec{v} - \vec{v}_d). \tag{2.55}$$

where the drag coefficient is defined as

$$C_d = \begin{cases} 24 Re_d^{-1} + 3.48 Re_d^{-0.313} & \text{if } 0 < Re_d \leq 1000 \\ 0.424 & \text{if } Re_d > 1000, \end{cases} \tag{2.56}$$

and the Reynolds number as

$$Re_d = \frac{2\rho \|\vec{v} - \vec{v}_d\| r}{\mu} \tag{2.57}$$

The form of the drag coefficient is based on empirical data of [Nicholls, 1972]. The source term contribution due to inter-phase drag is defined as

$$\vec{q}_{\vec{V}_{d,i}} = \mu_0 \int_r \frac{\mathrm{d}\vec{v}_d}{\mathrm{d}t} \, \phi(r) \, r^i \, \mathrm{d}r \tag{2.58}$$

where the acceleration of an individual droplet is

$$\frac{\mathrm{d}\vec{v}_d}{\mathrm{d}t} = \frac{3}{8} \frac{\rho}{\rho_d} \frac{C_d}{r} \parallel \vec{v} - \vec{v}_d(r) \parallel (\vec{v} - \vec{v}_d(r)) \tag{2.59}$$

In order to equate the rate of change of the moment-averaged momentum with Eq. (2.55), a number of steps are required. First, $\vec{v}_d$ needs to be replaced by the moment dependent relation, $\vec{v}_d(r)$ and secondly, the instantaneous continuum velocity, $\vec{v}$, requires approximating.

The velocity, $\vec{v}$, is decomposed into its mean and fluctuating component, whereby the mean velocity is that solved by the continuum momentum equation and the fluctuating velocity is approximated using the turbulent kinetic energy, k, provided by the turbulence model, as

$$\vec{v}' = (\vec{\gamma} - 0.5) \sqrt{\frac{2}{3}k} \tag{2.60}$$

where $\vec{\gamma}$ is randomly generated in the interval $\vec{0} - \vec{1}$.

The drag term can either be evaluated analytically, performing a summation of three integrals (assuming the functional form of the velocity distribution is of a simple form), or numerically by discretizing the PDF and the droplet velocity profile. For analytical integration the conditions relating to the drag coefficient in Eq. (2.56) are rearranged to provide critical radii, r_a and r_b respectively. The drag term is then made up of three parts: the integral of Eq. (2.58) between 0 and r_a, r_a and r_b and lastly between r_b and ∞.

2.5.2 Virtual Mass and Pressure Forces

The virtual mass force and the force acting on the droplet due to the pressure field are relatively small contributions to the overall force acting on the droplet. The virtual mass force is approximated as

$$\vec{F}_{vm} = -\frac{4}{3}\pi r^3 \rho C_{vm} \frac{\mathrm{d}(\vec{v}_d - \vec{v})}{\mathrm{d}t} \qquad (2.61)$$

where $C_{vm} \approx 0.5$. This represents the force required to accelerate the surrounding fluid entrained by the droplet. Since its contribution is relatively small, moment averaged velocities are considered rather than droplet velocities. The term, rewritten in a suitable form becomes

$$\vec{q}_{\vec{V}_{d,i}} = -0.5 \frac{\rho}{\rho_d} \mu_i \frac{(\vec{V}_{d,i}^n - \vec{v}^n) - (\vec{V}_{d,i}^o - \vec{v}^o)}{\Delta t} \qquad (2.62)$$

The force acting on the droplet due to the pressure gradient

$$\vec{F}_p = -\frac{4}{3}\pi r^3 \operatorname{grad} p \qquad (2.63)$$

is also rewritten, becoming

$$\vec{q}_{\vec{V}_{d,i}} = -\frac{1}{\rho_d} \mu_i \operatorname{grad} p \qquad (2.64)$$

where p is the instantaneous pressure (at present this is approximated with the time-averaged pressure derived from the pressure-correction equation).

2.5.3 Droplet Break-up

Three break-up models are presented. The first model of Pilch and Erdman [1987] encompasses all the known break-up phenomena. The second model of Hsiang and Faeth [1992] is applicable for diesel spray cases, whereby no categorizations are made regarding the droplet break-up methods. Lastly, the model of Reitz and Diwakar [1986] considers secondary break-up only; that of bag and stripping break-up.

With all the models, the manner in which they contribute to the source terms of the moments equations is the same, only the number of droplets produced, N_b, and the timescale for this process, τ_b, differs between the models. The equations below are presented here to show how any given break-up model contributes to any transported

moment (and that no contribution is made for μ_3).

The source term contribution to the moment transport equations due to break-up is of the form

$$q_{\mu_i} = \mu_0 \int_r \frac{\delta r^i}{\delta t} \phi(r) \, \mathrm{d}r \tag{2.65}$$

where

$$\frac{\delta r^i}{\delta t} = \frac{\left(N_b^{\frac{3-i}{3}} - 1\right) r^i}{\tau_b} \tag{2.66}$$

The number of droplets produced from the break-up of a single droplet is determined by considering droplet volume conservation, giving

$$N_b = \left(\frac{r}{r_{st}}\right)^3 \tag{2.67}$$

where r_{st} is the stable droplet radius.

None of the resultant terms of the break-up models are presented in integral form, although the first model can be integrated analytically [Beck and Watkins, 2002]. The remaining models must be either integrated numerically or approximated to enable analytical integration. In this work the former method is implemented.

Pilch and Erdman Model

Break-up occurs if

$$We = \frac{2\rho \, \|\vec{v} - \vec{v}_d\|^2 \, r}{\sigma_d} > We_{crit} \tag{2.68}$$

where the critical weber number $We_{crit} = 12 \left(1 + 1.077 \, Oh^{1.6}\right)$. Break-up phenomena are distinguised by their dimensionless break-up time, defined as

$$T = \begin{cases} 6 \, (We - 12)^{-\frac{1}{4}} & \text{if } 12 < We \leq 18 \\ 2.45 \, (We - 12)^{\frac{1}{4}} & \text{if } 18 < We \leq 45 \\ 14.1 \, (We - 12)^{-\frac{1}{4}} & \text{if } 45 < We \leq 350 \\ 0.766 \, (We - 12)^{\frac{1}{4}} & \text{if } 350 < We \leq 2670 \\ 5.5 & \text{if } We > 2670 \end{cases} \tag{2.69}$$

The break-up timescale then is calculated, using T, giving

$$\tau_b = 2T \frac{r}{\|\vec{v} - \vec{v}_d\|} \sqrt{\frac{\rho_d}{\rho}} \tag{2.70}$$

The stable droplet radius is found from

$$r_{st} = \frac{We_{crit}\, \sigma_d}{\rho \, \|\vec{v} - \vec{v}_d\| \, (1 - V_d)^2} \tag{2.71}$$

where

$$V_d = (0.375T + 0.2274T^2) \sqrt{\frac{\rho}{\rho_d}} \tag{2.72}$$

Reitz and Diwakar Model

This model considers two kinds of break-up; bag break-up which is caused by a non-uniform pressure field around the droplet and stripping break-up which is caused by the droplet being sheared. For both cases the condition for the onset of break-up and the stable radius is determined by the same inequality.

Bag Break-up   Instability is determined by the Weber number

$$We = \frac{\rho \, \| \vec{v} - \vec{v}_d \|^2 \, r}{\sigma_d} \geq C_{b,1}, \tag{2.73}$$

where $C_{b,1}$ is an empirical coefficient in the range 3.6 to 8.4. The associated time scale is

$$\tau_b = C_{b,2} r^{\frac{3}{2}} \left(\frac{\rho_d}{\sigma_d} \right)^{\frac{1}{2}} \tag{2.74}$$

where $C_{b,2} \approx 2.22$.

Stripping Break-up   Instability is determined by

$$\frac{We}{\sqrt{Re_d}} = \| \vec{v} - \vec{v}_d \|^{\frac{3}{2}} \, r^{\frac{1}{2}} \left(\frac{\mu\rho}{2} \right)^{\frac{1}{2}} \geq C_{s,1} \tag{2.75}$$

where $C_{s,1} = 0.5$. The associated time scale is

$$\tau_b = \frac{C_{s,2}r}{\parallel \vec{v} - \vec{v}_d \parallel} \left(\frac{\rho_d}{\rho}\right)^{\frac{1}{2}} \tag{2.76}$$

where $C_{b,2}$ is an empirical coefficient in the range 2 to 20.

Hsiang and Faeth Model

For diesel sprays the following model encompasses all break-up regimes. Break-up takes place if the $We > 6$ and the model is valid for Weber numbers less than 1000. The stable diameter is defined as

$$r_{st} = 6.2r^{\frac{1}{2}}\left(\frac{\rho}{\rho_d}\right)^{\frac{1}{4}}\sqrt{\frac{\mu_d}{\rho_d \parallel \vec{v} - \vec{v}_d \parallel}} \tag{2.77}$$

and the corresponding timescale is

$$\tau_b = \frac{5}{1 - Oh/7}\frac{r_d}{\parallel \vec{v} - \vec{v}_d \parallel}\sqrt{\frac{\rho_d}{\rho}} \tag{2.78}$$

2.5.4   Droplet Collisions

The collision model is based on the work of O'Rourke [1981] and applied here only to its effects on the moments. This simplifies the model by only considering coalescence. Separation and bounce have no effect on the droplet size distribution. The form of the source term contribution is similar to that of the break-up. Here, the number of droplets undergoing coalescence is determined by empirical and statistical methods in addition to critical radii conditions.

The coalescence of N_d donor droplets of radius r_d with a collector droplet of radius r_c, results in

$$\frac{\delta r^i}{\delta t} = \frac{1}{\delta t}\sum_{r_d}^{r_c}\left[(r_c^3 + N_d r^3)^{\frac{i}{3}} - r_c^i - N_d r^i\right] \tag{2.79}$$

The number of donor droplets undergoing coalescence is determined by the following method: The probability of a collector droplet undergoing N collisions with droplets of

size r_d in the time interval δt is assumed to follow a Poisson distribution

$$P_N = \frac{\bar{n}^N}{N!}e^{-\bar{n}} \tag{2.80}$$

where the mean number of collisions is defined as

$$\bar{n} = \pi(r_d + r_c)^2 \parallel \vec{v}_c - \vec{v}_d \parallel \delta t \frac{N_d}{\delta\Omega} \tag{2.81}$$

Whilst there may be the possibility of P_N collisions based on above two equations, the term $\parallel \vec{v}_c - \vec{v}_d \parallel$ does not take into account whether the droplets are heading towards each other or not. The information required to determine this is not available in the moments methodology so a random number between 0 and 1 is used. If the random number is greater than 0.5, the droplets will collide.

Since not all collisions result in coalescence, the probability that coalescence takes place is

$$P_{coal} = min\left[2.4\frac{f(\gamma)}{We_L}, 1\right] \tag{2.82}$$

where $\gamma = r_c/r_d$ and

$$f(\gamma) = 2.7\gamma - 2.4\gamma^2 + \gamma^3 \tag{2.83}$$

and

$$We_L = \frac{\rho_d \parallel \vec{v}_c - \vec{v}_d \parallel^2 r}{\sigma_d} \tag{2.84}$$

By generating two random numbers, $N_{r,1}$ and $N_{r,2}$, in the interval $(0-1)$ the actual occurrence of a collision taking place is if $N_{r,1} > P_{N=0}$. If collisions take place then coalescence is the result of that collision if $P_{coal} < N_{r,2}$ and the number of donor droplets involved is found from the Poisson distribution, such that

$$\sum_{i=0}^{N-1} P_i < N_{r,1} < \sum_{i=0}^{N} P_i \tag{2.85}$$

2.6 Injection Conditions

2.6.1 Injector

The approach used in this methodology is to resolve the actual size of the nozzle orifice (Fig. 2.4), rather than projecting a larger equivalent orifice in front of the injector [Beck, 2000].
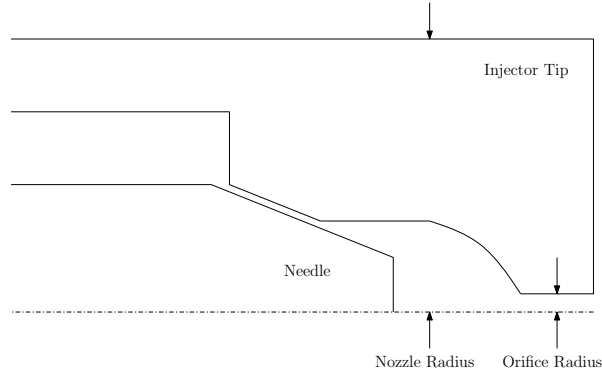
Figure 2.4: Schematic of a typical injector tip

The actual injector is represented computationally by the overall shape of the injector tip (Fig. 2.5). The modelled nozzle orifice is protruded in order to clarify its size.
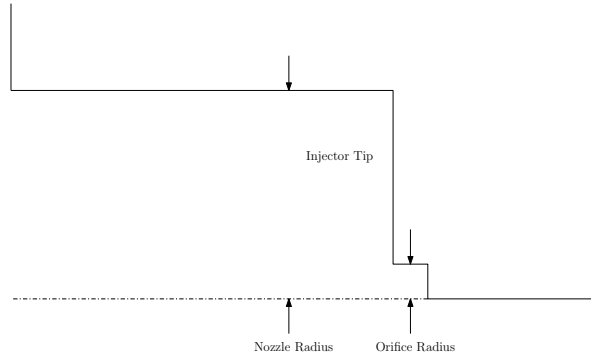
Figure 2.5: Represented injector tip

2.6.2 Injected Moments

Moments of the injected droplet size distribution are based on the Gamma distribution [Yue and Watkins, 2004]. Specifying three parameters: the liquid volume fraction, Θ, Sauter mean radius, r_{32} and the skewness parameter, k, the first two parameters μ_3 and

μ_2 are found by

$$\mu_3 = \frac{\Theta}{\frac{4}{3}\pi} \tag{2.86}$$

$$\mu_2 = \frac{\mu_3}{r_{32}} \tag{2.87}$$

and all other moments are determined recursively using the relation

$$\frac{\mu_{i+1}}{\mu_i} = r_{32}\frac{k+i}{k+2} \tag{2.88}$$

The three parameters are related to the nozzle orifice radius, the injector operating conditions and how the nozzle orifice is modelled. Since the nozzle orifice is resolved, the exiting liquid volume fraction will be high $(0.9 - 1)$. Such a high volume fraction is inconsistant with the assumption that the liquid is in the form of spherical droplets, though for the sake of resolving the injector and maintaining a simple injection model, this inconsistancy is not rectified in this work.

The exiting bulk liquid is assumed to have been broken up into droplets, so the Sauter mean radius is approximated to be in the range $0.05r_{orif} - 0.15r_{orif}$. Finally, because only break-up of bulk liquid has taken place, the relative number of smaller droplets (than the mean) will be low, implying that the distribution will only have a weak positive skew, leading to a range of $3 - 7$ for parameter k (Fig. 2.6).

2.6.3 Injection Velocity

From the ambient pressure and the operating pressure of the injector, the average speed of the exiting liquid and entrained gas can be approximated by

$$U = C_d\sqrt{\frac{2(P_{inj} - P_{amb})}{\rho_d}} \tag{2.89}$$

where the discharge coefficient, C_d, is approximately 0.7. The spray half-cone angle is then used to obtain the orifice outermost velocity. The variation of velocity towards the axis is controlled by the appropriate radial profile.
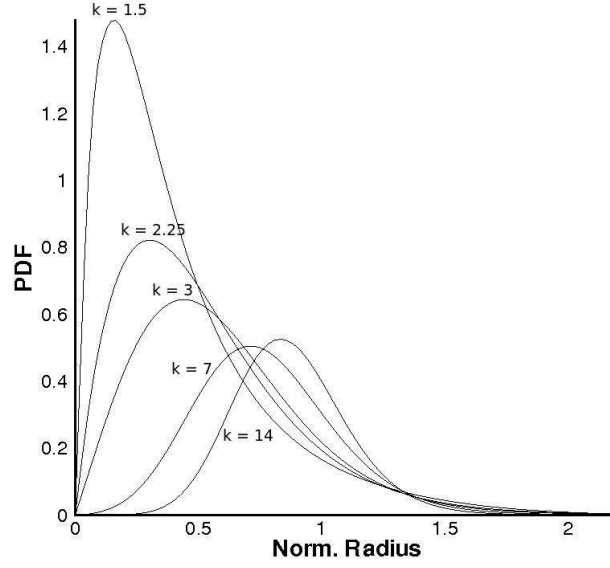
Figure 2.6: Inlet PDFs with $r_{32} = 1$ and $k = 1.5$, 2.25, 3, 7 and 14.

2.6.4 Radial Profiles

To reasonably approximate the behaviour of the exiting spray, the nozzle orifice face is discretized into a number of faces (typically 2 - 5), allowing the injector conditions to be varied radially (Fig. 2.7).
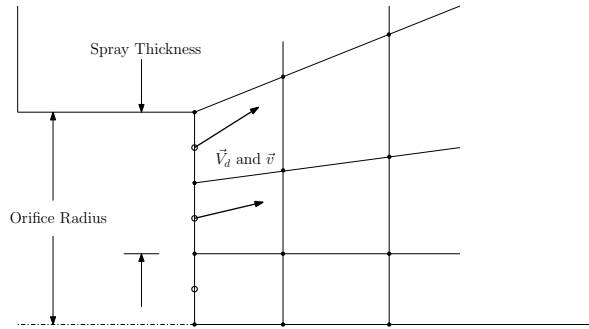
Figure 2.7: Modelling of the nozzle orifice

Radial profiles presented here are used for both the moments and the exiting injector speed (Fig. 2.8). These profiles enable the representation of the higher concentration of the liquid towards the outer edge of the orifice (Fig. 2.8(a)) due to swirl and the spread of the spray defined by the half-cone angle, applied to the speed (Fig. 2.8(b)). The functions

are defined as

$$p_1(r) = \left(\frac{1}{r_{orif}}r\right)^{\beta_1} \tag{2.90}$$

$$p_2(r) = \left(\frac{1}{r_{orif}}r\right)^{\beta_2} \tag{2.91}$$

for the moments and speed variation respectively, where $\beta_2 < \beta_1 < 1$. Currently β_1 is set as 0.7 and β_2 as 0.3.
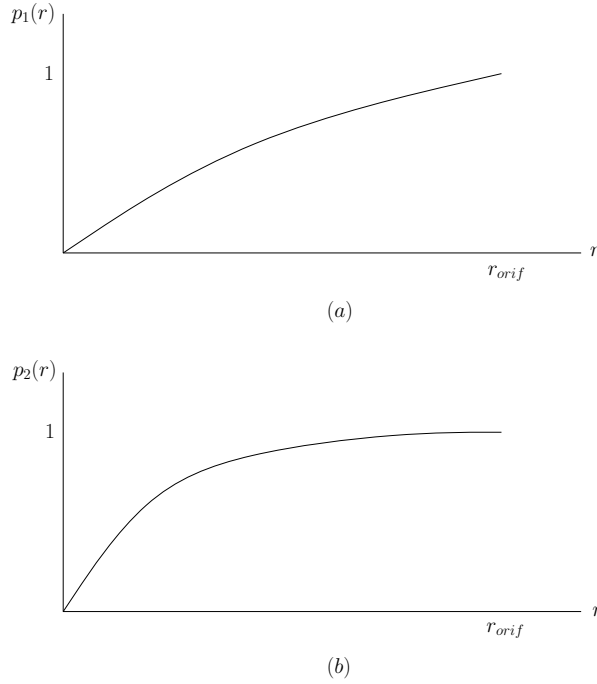
Figure 2.8: Nozzle radial profiles

2.6.5 Discharge Profiles

Two profiles are used to govern the discharge of the liquid from the injector (Fig. 2.9), where $t_1 - t_0$ is the injection duration. The first profile (Fig. 2.9(a)) controls the quantity discharged, and the second profile (Fig. 2.9(b)) controls the rate of discharge. The rate of discharge profile, $p_2(t)$, extends beyond the liquid discharge profile, $p_1(t)$, to represent the pressure potential remaining constant thoughout the duration of the discharge.
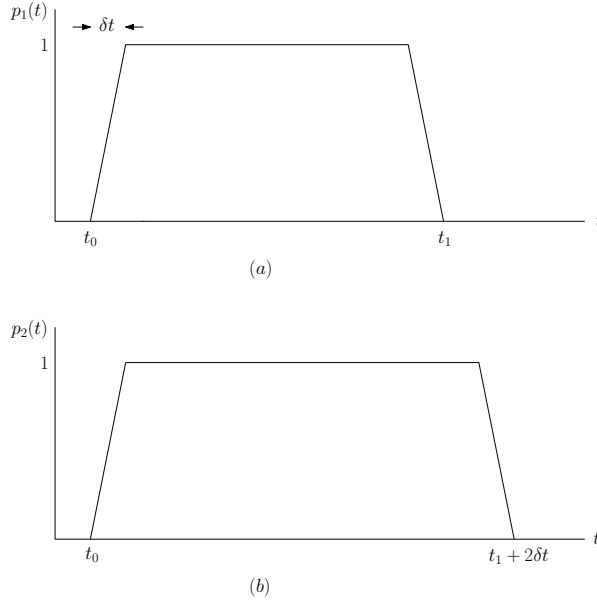
Figure 2.9: Nozzle discharge profiles

2.7 Impaction Conditions

Wall boundary conditions are based on the spray impingement model of Bai and Gosman [1995], where the condition of the wall and the state of the impinging spray determine the outcomes. If the wall is dry the velocity and moments of the splashing droplets are determined. If the wall is wet, rebounding conditions in addition to splashing conditions are defined. An alternative model is described by Grover and Assanis [2001] though is not considered here.

At the wall face (Fig. 2.10), the splashing and rebounding conditions are determined from the near-wall control volume injected spray state. The impacting spray boundary conditions at the wall are defined as being permeable, i.e. the spray passes through the wall. This prevents a build-up of moments in the near-wall control volume. To represent the build-up of liquid which actually would occur, the sum of the μ_3 fluxes at the wall (multiplied by $\frac{4}{3}\pi$) becomes the source term for the liquid film equation.

2.7.1 Critical Radii

In order to determine which droplets undergo the different processes, critical radii are obtained from the following correlations. Splashing and rebounding moments are calculated
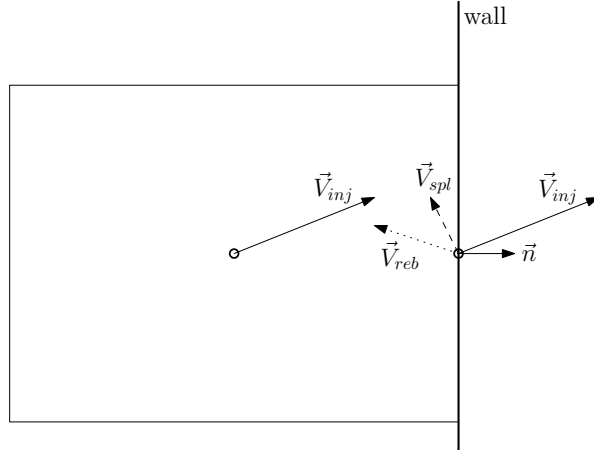
Figure 2.10: Division of the spray into injected, splashing and rebounding sprays

from integrating the near-wall PDF of the incoming spray between the limits prescribed by the critical radii. Moment-averaged splashing and rebounding velocities are calculated in a similar manner.

Dry Walls

Splashing takes place when

$$We_d La^{0.18} > C_{1,d} \tag{2.92}$$

where La is the Laplace number, defined as

$$La = \frac{2\rho_d \sigma_d r}{\mu_d} \tag{2.93}$$

$C_{1,d}$ is related to the wall roughness r_s by

$$C_{1,d} \approx 2588 \, r_s^{-0.254} \tag{2.94}$$

for wall roughness $0.05 \leq r_s \leq 12 \, \mu m$.

Wet Walls

Rebound takes place when

$$We_d < 5 \tag{2.95}$$

and splashing when

$$We_d La^{0.18} > 1320 \tag{2.96}$$

Droplets outside these ranges for both wet and dry walls are assumed to stick. From these conditions, critical radii are determined and then used to integrate over the near-wall droplet distribution, obtaining the appropriate boundary condition moments for the splashing and rebounding spray. A droplet undergoing splashing is assumed to break up into N_{spl} droplets (taken as equal to 2 by Lemini and Watkins [2002]), resulting in

$$\mu_i = N_{spl}^{\frac{3-i}{i}} \mu_{i,spl}. \tag{2.97}$$

Transition

In practice, the wall becomes wet over the duration of the spray impacting on the wall. This transition should be considered rather than assuming that either the wall is wet or dry from the outset. To perform this transition, the method proposed here compares the volume fraction of the liquid film on the wall with a critical film volume fraction, θ_{wet}, to determine whether the wall is wet. If the volume fraction is less than the critical value and non-zero, the coefficient $C_{1,d}$ is modified by the function

$$C_{1,d} = \frac{1320 - C_{1,d}}{\theta_{wet}} \theta + C_{1,d} \tag{2.98}$$

and the wall is assumed to be dry. The critical film volume fraction is taken as 0.01.

2.7.2 Resultant Velocities

Corresponding droplet velocities are calculated from the volume-averaged incoming velocity and the wall normal vector.

$$\vec{v}_{in} = \vec{v}_d(r) \tag{2.99}$$

$$\vec{v}_n = (\vec{v}_{in} \cdot \vec{n}) \, \vec{n} \tag{2.100}$$

$$\vec{v}_t = \vec{v}_{in} - \vec{v}_n \tag{2.101}$$

$$\vec{v}_{out} = -C_n \vec{v}_n + C_t \vec{v}_t \tag{2.102}$$

For rebounding droplets, the process is assumed to be inelastic, resulting in the coefficients taking

$$C_n = 0.993 - 1.76\theta + 1.56\theta^2 - 0.49\theta^3 \tag{2.103}$$

$$C_t = 0.714 \tag{2.104}$$

where θ is the incidence angle. Splashing droplets take identical coefficients of 0.25 Lemini and Watkins [2002].

Upon integrating between the limits for the splashing and rebounding conditions, two set of moments and moment-averaged velocities will be obtained (for splashing spray and the rebounding spray). The likelihood is that within either set, the moment-averaged velocities will be dissimilar (assuming a non-uniform droplet velocity profile), potentially becoming a source of divergence for the model. To overcome this, the fourth moment-averaged velocities ($\vec{V}_{d,3,spl}$ and $\vec{V}_{d,3,reb}$) are used for all moments within their respective sets.

2.8 Discretization

The Finite-Volume method is used to discretize the domain and equations. Details of the method can be found in Ferziger and Perić [2002]. Here, only the main points are discussed with emphasis on the treatment of the discrete phase equations.

2.8.1 Scalar Equation

Starting with the discretization of a generic scalar equation (2.105), the differences which need addressing in the discrete phase treatment are highlighted.

$$\frac{\partial}{\partial t}\int_\Omega \Theta \rho\, \phi\, \mathrm{d}\Omega + \int_S \Theta \rho\, \vec{v}_\phi \cdot \vec{n}\, \phi\, \mathrm{d}S = \int_S \Theta \Gamma_\phi \mathrm{grad}\phi \cdot \vec{n}\, \mathrm{d}S + \int_\Omega q_\phi\, \mathrm{d}\Omega \qquad (2.105)$$

Surface Integrals

Second order interpolation is obtained to approximate the face integral by employing the midpoint rule:

$$F = \int_S f \mathrm{d}S = \sum_k \int_{S_k} f \mathrm{d}S_k \approx \sum_k f_k S_k \qquad (2.106)$$

Volume Integrals

Assuming that the integrand varies linearly within the control volume, the integral can be approximated as

$$Q = \int_\Omega q \mathrm{d}\Omega \approx q_\mathrm{P} \Delta\Omega \qquad (2.107)$$

Interpolation

Within the discretized domain, only volume center values are stored. However, for the surface integrals, face values are required. A number of means of approximating the face value for the convective term are available and are outlined below.

Linear Interpolation: linear interpolation is the most obvious, but in certain conditions produces unbounded results. It is presented here for completeness, but not used;

$$\phi_k = (1 - \lambda_k)\phi_\mathrm{P} + \lambda_k \phi_\mathrm{K} \qquad (2.108)$$

where

$$\lambda_k = \frac{L_{\text{Pk}}}{L_{\text{PK}}} \tag{2.109}$$

Upwind Differencing: Upwind differencing is used to ensure boundedness but results in excess diffusion, being only a first order accurate scheme. The scheme is used implicitly in solving transport equations (i.e. the convective contributions in the resulting matrix are based on this method).

$$\phi_k = \min(\vec{v} \cdot \vec{n}, 0)\phi_{\text{K}} + \max(\vec{v} \cdot \vec{n}, 0)\phi_{\text{P}} \tag{2.110}$$

TVD Schemes: To avoid both the unboundedness of linear interpolation and the numerical diffusion of the upwind differencing, total variation diminishing scheme is used.

$$\phi_k = \phi_{\text{C}} + \frac{1}{2}\psi(r_f)(\phi_{\text{D}} - \phi_{\text{C}}) \tag{2.111}$$

where ϕ_{C} is the volume center value immediately upstream of the face, ϕ_{D} is the volume center value immediately downstream of the face and $\psi(r_f)$ is the flux limiter [Darwish and Moukalled, 2003]. There are a number of possibilities for the choice of flux limiter, though here only two methods are considered; the first is the Min-mod limiter which is based on central differencing

$$\psi(r_f) = \max(0, \min(1, r_f)) \tag{2.112}$$

and the second is the Superbee limiter which is based on the second order upwind scheme

$$\psi(r_f) = \max(0, \min(1, 2r_f), \min(2, r_f)) \tag{2.113}$$

r_f is the r-factor, defined as

$$r_f = \frac{\phi_{\text{C}} - \phi_{\text{U}}}{\phi_{\text{D}} - \phi_{\text{C}}} \tag{2.114}$$

where

$$\phi_{\text{U}} \approx \phi_{\text{C}} - 2\,\text{grad}\phi_{\text{C}} \cdot \vec{r}_{\text{CD}} \tag{2.115}$$

66

Interface Capturing Schemes: For scalar variables such as concentration, convection methods developed for interface capturing are likely to be of use in the transportation of moments. These methods are high order schemes which ensure the concentration remains bounded (so long as the implementation is exact). The method presented here is that by Muzaferija and Peric [1999] and can be used for moment quantities also. Ubbink [1997] offers an in depth analysis of interface capturing methods, though the scheme assumes physical limits to the variable are known (in the case of transporting concentration the lower bound and upper bound are 0 and 1 respectively. For moments, only a lower bound can be defined).

$$\phi_k = \lambda \, \phi_C + (1 - \lambda) \, \phi_D \tag{2.116}$$

where

$$\lambda = (1 - \tilde{\phi}'_k) \frac{\phi_D - \phi_U}{\phi_D - \phi_C} \tag{2.117}$$

and

$$\tilde{\phi}'_k = \tilde{\phi}''_k \sqrt{\cos\theta} + \tilde{\phi}_C (1 - \sqrt{\cos\theta}) \tag{2.118}$$

The angle between the gradient of ϕ_C and the face normal vector $\vec{n}$, θ, is a key part of this scheme; the interpolation constant, γ is related to the direction of greatest change.

$$\tilde{\phi}''_k = \begin{cases} \tilde{\phi}_k & \text{if } Co \leq 0.3 \\ \tilde{\phi}_C + (\tilde{\phi}_k - \tilde{\phi}_C) \frac{0.7 - Co}{0.7 - 0.3} & \text{if } 0.3 < Co \leq 0.7 \\ \tilde{\phi}_C & \text{if } Co > 0.7 \end{cases} \tag{2.119}$$

where

$$\tilde{\phi}_k = \begin{cases} \tilde{\phi}_C & \text{if } \phi_C \leq 0 \\ 2\tilde{\phi}_C & \text{if } 0 < \phi_C \leq 0.5 \\ 1 & \text{if } 0.5 < \phi_C \leq 1 \\ \tilde{\phi}_C & \text{if } \phi_C > 1 \end{cases} \tag{2.120}$$

and

$$\tilde{\phi}(\vec{x}) = \frac{\phi(\vec{x}) - \phi_U}{\phi_D - \phi_U} \tag{2.121}$$

The Courant number, Co, is taken as the maximum of the face Courant numbers over the control volume, C, as used by Waclawczyk and Koronowicz [2006].

Deferred Correction and Blending

A method for implementing a higher order interpolation scheme maintaining a compact stencil is to use the lower order scheme to discretize the term and form the matrix and include the difference between the higher order scheme and the lower order scheme based on current values in the right-hand side (the source term).

$$F_k = F_k^L + \gamma(F_k^H - F_k^L)^{curr} \tag{2.122}$$

Normally, a value of γ is set for each equation, typically in the range (0.5 - 1). However, under certain circumstances at particular cell faces, it may be desirable to modify this value.

When solving the moment-averaged momentum equations using a high order convection scheme, it was found that augmentations to the source term by Eq. (2.122) must be zeroed where the spray does not exist, as shown in Fig. 2.11. This step is essential for the spray to be transported using high-order convection schemes.
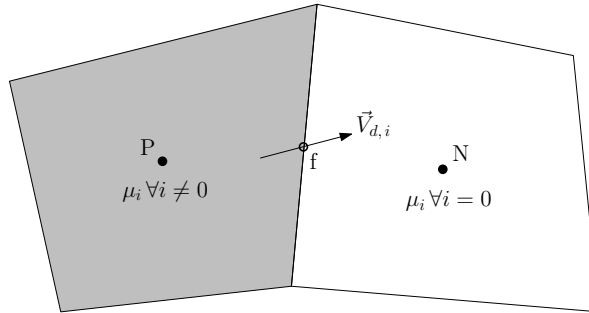

Figure 2.11: $(F_k^H - F_k^L)^{curr} = 0$ in volume N since the spray is not present there

Gradient

Calculation of the gradient of a value over its volume is performed by making use of the Gauss' theorem;

$$\text{grad}\phi_P = \frac{1}{\Delta\Omega} \sum_k S_k \vec{n}_k \phi_k \tag{2.123}$$

In order to interpolate to the face centre, values either side of the face are required. For unstructured grids, the locations of these two points do not necessarily lie along the same line passing through the face centre (Fig. 2.12) and so values at auxiliary locations (P′ and N′) are determined and used instead. To calculate these auxiliary values, knowledge of the gradient of the variable is required, which in turn requires the face centre values. Thus an iterative scheme is used to solve the gradient accurately. The number of iterations performed is typically one to 3 iterations on non-orthogonal grids. For 2-dimensional
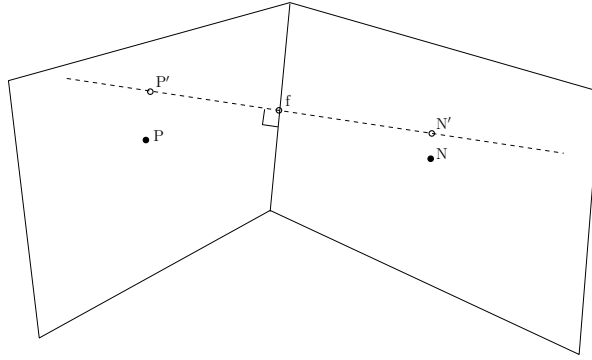
Figure 2.12: Face value interpolation

cylindrical grids, an additional term is included for $\frac{\mathrm{d}}{\mathrm{d}y}$ (where $y = r$) when the gradient is solved using finite volume methods, as detailed in Ferziger and Perić [2002]

$$\frac{\mathrm{d}}{\mathrm{d}y}(\phi_{\mathrm{P}}) = \frac{1}{\Delta\Omega}\sum_k S_k n_{y,k}\phi_k - \Delta S\,\phi_{\mathrm{P}} \tag{2.124}$$

where ΔS is the front face area, which is equal to the volume on a 2D planar grid. Here it is noted that $\mathrm{div}(\vec{v}) \neq 0$ if the gradient calculation above is used (for incompressible flow). However, the gradient is not used to calculate divergence for the FV method.

Convection Term

Consider the convection term in the scalar equation. This is discretized in the following manner, using the upwind scheme

$$A_{\mathrm{K}}^c = \Theta\rho\min(\vec{v}_k\cdot\vec{n}_k, 0) \tag{2.125}$$

$$A_{\mathrm{P}}^c = -\sum_{\mathrm{K}} A_{\mathrm{K}}^c + \Theta\rho\sum_k \vec{v}_k\cdot\vec{n}_k \tag{2.126}$$

69

The second summation in the above equation is usually assumed to equal zero when dealing with the continuous phase. However, for the discrete phase this summation must be included.

Temporal Term

Again, a number of choices exist as to which discretization scheme is used for the unsteady term, though the preferred scheme is the implicit Three Time Levels method so this will be presented.

$$\frac{\partial}{\partial t} \int_\Omega \phi \mathrm{d}\Omega \approx \frac{1}{2} \left(3 \left(\Theta \rho \phi\right)^{n+1} - \left(4 \left(\Theta \rho \phi\right)^n - \left(\Theta \rho \phi\right)^{n-1}\right)\right) \frac{\Delta \Omega}{\Delta t} \tag{2.127}$$

To include the unsteady term, only A_P and q_ϕ require modification. The contributions are

$$A_\mathrm{P}^t = \frac{1}{2} 3(\Theta \rho)^{n+1} \frac{\Delta \Omega}{\Delta t} \tag{2.128}$$

and

$$q_\phi \Delta \Omega = -\frac{1}{2} \left(4 \left(\Theta \rho \phi\right)^n - \left(\Theta \rho \phi\right)^{n-1}\right) \frac{\Delta \Omega}{\Delta t} \tag{2.129}$$

Now, with the inclusion of the temporal term, the main coefficient is guaranteed to take a positive value, so long as Δt is sufficiently small (and $\Theta \rho \neq 0$).

Additional Term

The treatment of the additional term in (2.48) needs to be included. This happens to be quite straight forward, being included implicitly.

$$-\phi \left(\frac{\partial \Theta \rho}{\partial t} + \mathrm{div}(\Theta \rho \vec{v})\right) \rightarrow -\phi \left(\frac{\partial}{\partial t} \int_\Omega \Theta \rho \mathrm{d}\Omega + \int_S \vec{v}_\phi \cdot \vec{n} \Theta \rho \mathrm{d}S\right) \tag{2.130}$$

Discretizing this term then leads to

$$A_\mathrm{P}^a = -\frac{1}{2} \left(3(\Theta \rho)^{n+1} - \left(4(\Theta \rho)^n - (\Theta \rho)^{n-1}\right)\right) \frac{\Delta \Omega}{\Delta t} - \Theta \rho \sum_k \vec{v}_k \cdot \vec{n}_k \tag{2.131}$$

Main Coefficient

The resulting coefficient from the summation of the above terms reduces to

$$
\begin{aligned}
A_{\mathrm{P}} &= A_{\mathrm{P}}^c + A_{\mathrm{P}}^t + A_{\mathrm{P}}^a && (2.132) \\
&= -\sum_{\mathrm{K}} A_{\mathrm{K}}^c + \frac{1}{2}\left(4(\Theta\rho)^n - (\Theta\rho)^{n-1}\right)\frac{\Delta\Omega}{\Delta t} && (2.133)
\end{aligned}
$$

2.8.2 Continuity Equation

Since there is no pressure-velocity coupling as in the discrete phase, the continuity equation (moments equation) is discretized using the above methods. This results in the main coefficient

$$
A_{\mathrm{P}} = -\sum_{\mathrm{K}} A_{\mathrm{K}}^c + \Theta\rho\sum_{k}\vec{v}_k \cdot \vec{n}_k + \frac{1}{2}3(\Theta\rho)^{n+1}\frac{\Delta\Omega}{\Delta t} \tag{2.134}
$$

which is the summation of the neighbour coefficients and convection fluxes and the temporal term.

71

2.9 Implementation

This section documents how the mathematical model presented earlier is implemented into the platform CFD code. The topics address the data structures used to construct and solve the equations, the solution algorithm and details on aiding the stability of the spray model. Techniques presented here are original, except those which are standard practice in a typical CFD code.

2.9.1 Outbound Outlet

To prevent recirculation occurring near an outlet boundary, the near-outlet velocity is conditioned such that if the velocity is pointing into the domain ($\vec{v} \cdot \vec{n} < 0$), the normal component of the velocity is set to zero. This modification has been found to stabilize convergence, especially if the outlet area is relatively large. Such an implementation assumes that recirculation is not expected near the outlet.

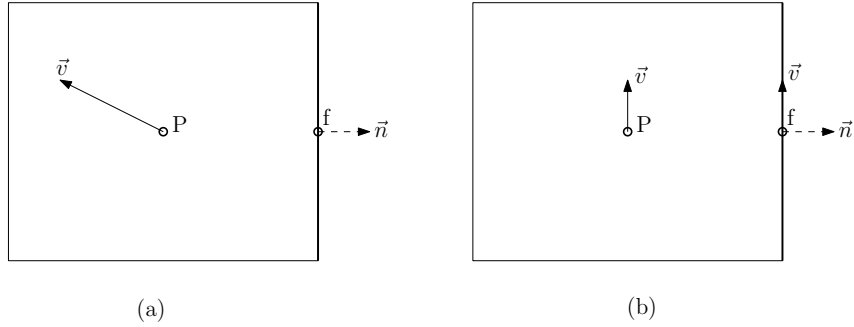(a)   (b)

Figure 2.13: Outbound outlet modification

2.9.2 Wall Shape

Because the spray is modelled as a continuum, interpenetration of the incoming and rebounding spray is only possible if the rebounding spray is transported separately from the incoming spray. However, if the wall is concave (Fig. 2.14), the rebounding droplets may also interpenetrate. This model provides no provision for that process to take place, though, this is not considered a major drawback since post-impaction droplets tend to be carried by the surrounding gas.
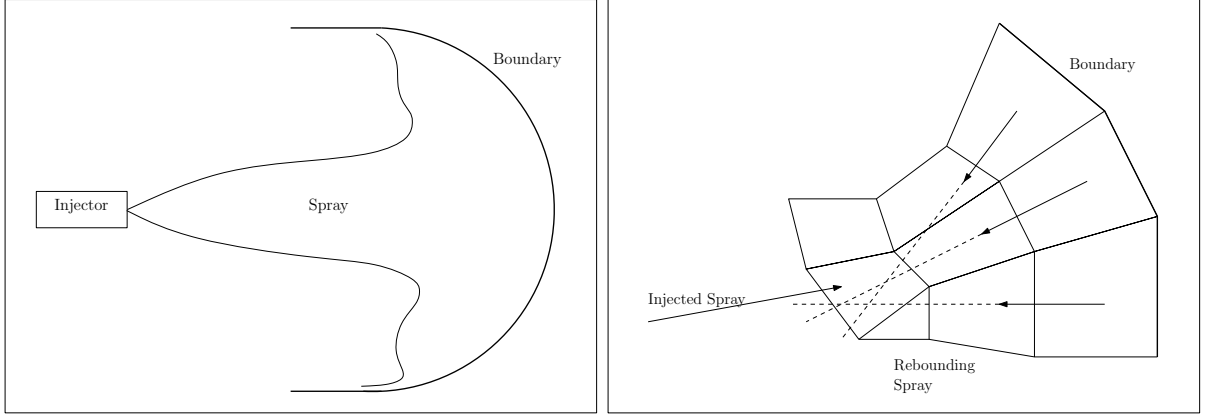
Figure 2.14: Effect of curved surfaces

2.9.3 Parameters

Scaling

To ensure numerically sensible numbers for transported properties, length and time base units are scaled up by a factor 1000. For sprays, injection duration is in milliseconds and droplet radius is in the range of 1 to 100 micrometers. The length scaling improves significantly the numerical range of the moment set (from μ_0 to μ_4), reducing it from approximately 25 orders of magnitude to approximately five.

Moments Closure

The number of moments being considered, N_μ, and their order, $P_\mu[-]$, must be defined. The latter, once defined, implies the former: i.e. $P_\mu[2, 3, 4]$ indicates that there are three moments and they are μ_2, μ_3 and μ_4.

Spray Model

The modelling parameters refer exclusively to the solution of source terms and boundary conditions of the discrete phase transport equations. They are the velocity-radius exponent, b, the number of droplets resulting from splashing, $N_{spl} = 2$, the condition of the wall: whether it is wet or dry and the wall roughness, $r_s = 0.08 \ \mu$m. The condition of the wall effects the number of sets of moments, $N_{\mu \, sets}$, being transported: if the wall is dry,

73

only the injected and rebounding spray needs to be transported. If the wall is wet, the splashing spray must also be transported. Break-up parameters for the model of Reitz and Diwakar [1986] are the critical Weber number, $C_{b,1}$, for bag break-up which is set to 6 and the timescale constant, $C_{s,2}$, for stripping break-up which is set to 20.

2.9.4 Transport Equations

Complete Set of Moments

Since a given set of moments are relating to a single underlying distribution, all the transported moments must be present within a given volume in order to represent the spray. This condition cannot be assured by the transportation of the moments alone.

To enforce this condition the spray is cropped (velocities and moments set to zero) where an incomplete set of moments are present. The condition for testing whether a complete set exists is if $\mu_j > C_\mu \, \mu_{j,ref}$, $\forall j$, where C_μ is the reference value multiplier (currently set as 10^{-7}) and $\mu_{j,ref}$ is the reference moment, which for this model is taken as the injected moment.

Cropping of the spray causes the overall model to become unconservative because a very small amount of liquid is being removed from the solution. Whilst this is undesirable, there appears to be no good alternative method for dealing with incomplete moment sets, especially since this method also removes moments strongly effected by numerical round-off errors.

Reliability of Moments

Whilst a complete set of moments may exist in a given volume, due to the potentially large numerical differences in their quantities, some moments (those far from the fourth moment) may require more iterations than others just to retain consistent ratios between the moments (assuming hydrodynamic effects are not considered). A simple test to observe the effect of unreliable moments propagation is to transport a couple of moments, performing one iteration per time step, and monitor the ratio of the moments. The non-uniformity of the ratio highlights this unreliability. If these moments were then to be used to determine the underlying distribution, the resulting PDF would be at best inaccurate.

To ensure moments are convected together, a predictor-corrector method is used. The predictor step solves the spray equations without calculating the hydrodynamic terms, then in the corrector step the hydrodynamic terms are solved. Typically, no more than three corrector iterations are required.

Data Structure

The storage of the generic equation data at a control volume or boundary face is shown in Fig. 2.15. The capacity to store all the data related to the solution of a transported property, `phi()`, is made available by defining the source term, `rhs()`, and gradient, `grad()`, and the coefficients which are generally associated with the volume fraction, `frc()`, density, `dns()`, and viscosity, `vis()`.
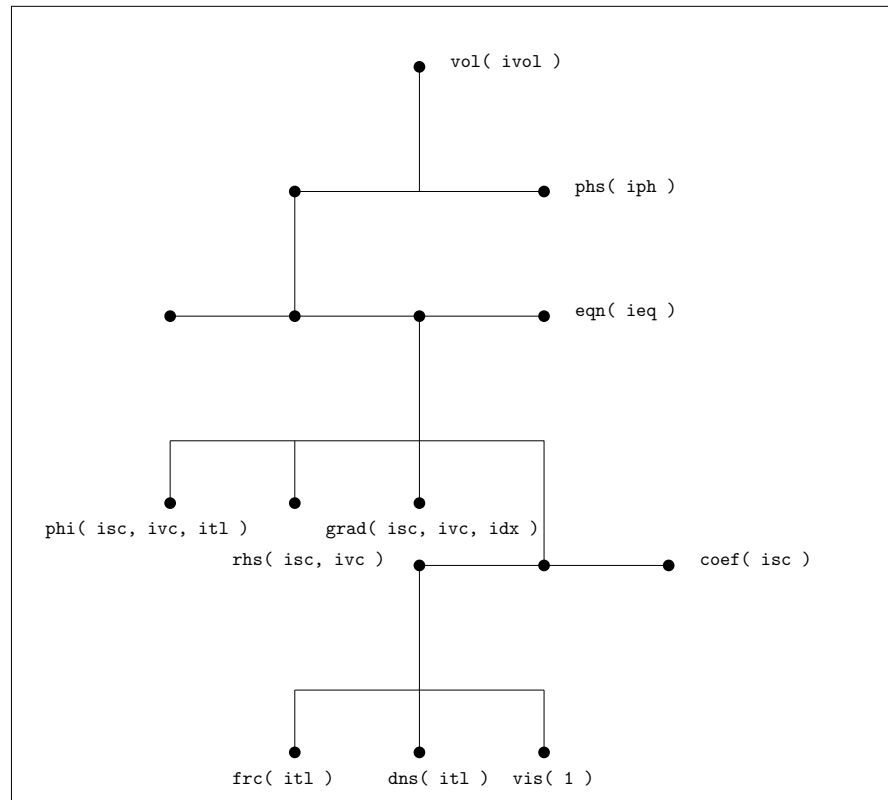

Figure 2.15: Local equation data structure

This structure is a substructure of the grid data structure, which provides two benefits: transported data is related to the grid on which it is solved, allowing for multiple grids to be defined and secondly, if the grid is adapted, volumes which are removed from the grid will also remove data associated with that volume.

Furthermore, the structure provides the capacity to store multiple equations relating to a particular phase, where the number of phases and associated equations can be modified on a case-by-case basis.

Allocation

All array data is defined with the `pointer` attribute instead of the `allocatable` attribute (in Fortran). This provides the possibility of the variable being pointed at or pointing to another variable and being allocated [Chapman, 2008].

Each equation is assumed to be made up of a number of components, whereby these components may either be scalars or vectors. This kind of definition is used since it enables a single transport equation to encapsulate all the moments and another transport equation to encapsulate all the moment-averaged velocities, facilitating the management of sets of moments.

Locally, the transported quantity is declared as

```
real(wp), dimension(:,:,:), pointer :: phi => null()
```

Each dimension is allocated as: Number of scalar components, `N_sc`, Number of vector components, `N_vc`, and Number of time levels, `N_tl`, resulting in

```
allocate( vol(ivol) % phs(iph) % eqn(ieq) % phi(1:N_sc, 1:N_vc, 1:N_tl) )
```

If the transported quantity is a vector (a velocity) then `N_vc` equals the number of dimensions of the geometry, `N_dx`, otherwise it is set to 1. The number of scalar components equals the number of groups of components multiplied by the number of components per group for a generic transport equation. In the case of the discrete phase momentum or moment transport equation, $N_{sc} = N_{\mu\,sets} \times N_\mu$. The number of time levels is set to 3 to enable the second order implicit scheme for time marching problems. For first order implicit differencing, it is set to two.

Coefficients

The following two tables define the coefficients for each transport equation, taking Eq. (2.105) as the template form of each equation.

Table 2.3: Coefficients

ϕ	Θ	ρ	Γ	$\vec{v}_\phi$
Continuum continuity, 1	θ	ρ	0	$\vec{v}$
Continuum momentum, $\vec{v}$	θ	ρ	$\mu + \mu_t$	$\vec{v}$
Continuum turb. kin. ener., k	θ	ρ	$\mu + \frac{\mu_t}{\sigma_k}$	$\vec{v}$
Continuum turb. diss. rate, ϵ	θ	ρ	$\mu + \frac{\mu_t}{\sigma_\epsilon}$	$\vec{v}$
Discrete continuity, $\underline{\mu}$	1	1	0	$\underline{\vec{V}}_d$
Discrete momentum, $\underline{\vec{V}}_d$	1	$\underline{\mu}$	0	$\underline{\vec{V}}_d$
Liquid film, θ	1	1	0	$\vec{0}$

where $\mu_t = C_\mu \rho \frac{k^2}{\epsilon}$, $C_\mu = 0.09$, $\sigma_k = 1$ and $\sigma_\epsilon = 1.3$.

The coefficients Θ, ρ and Γ defined in the generic transport equation of Eq. (2.105) must be defined for all equations at both the volumes and the boundary faces. In some cases, these properties are defined as material properties, such as volume fraction, density and viscosity respectively and in other cases as constants (either 0 or 1) or functions of properties ($\Gamma = \mu + \frac{\mu_t}{\sigma}$). To compensate for all possibilities, the transport equation data type is locally defined as

```
type::coef_t
  real(wp), dimension(:), pointer :: frc => null()
  real(wp), dimension(:), pointer :: dns => null()
  real(wp), dimension(:), pointer :: vis => null()
end type

type::eqn_t
  type(coef_t), dimension(:), pointer :: coef => null()
  real(wp), dimension(:,:,:), pointer :: phi => null()
end type
```

First, the array of coefficients is allocated

```
allocate( vol(ivol) % phs(iph) % eqn(ieq) % coef(1:N_sc) )
```

so each component of the transport equation has its own coefficients. Once the array of coefficients is allocated, its components may be used in the following ways: in the case of ρ being defined as the moment, μ_i, ρ is set to point at it (where `eqn(1)` is the moment-averaged momentum equation and `eqn(2)` is the moment equation);

```
 vol(ivol) % phs(iph) % eqn(1) % coef(isc) % dns => &
   vol(ivol) % phs(iph) % eqn(2) % phi(isc, 1, 1:N_tl)
```

otherwise ρ may be allocated and used like a normal variable.

This approach minimizes storage costs and maximizes connectivity between related data. Whilst the velocity, $\vec{v}$, is also a coefficient of the transport equation, it has not been necessary to include it in the coefficient structure, though could easily be done.

Source Terms

Normally, source terms for a given transport equation are solved during the procedure of setting up that equation. However, in the case of the source terms relating to the spray (both for the moment-averaged momentum and moments equation), these source terms are all solved and stored in a single procedure (Fig. 2.16). The reason for this is that the source terms for a given set of moments all depend on the same underlying distribution. As a result, `rhs()` must be allocated for the moment-averaged momentum and moments equation (effectively doubling the memory requirements for the spray model) and the momentum equation of the continuum (for storing the inter-phase drag term). This approach prevents the source terms being linearized (especially the inter-phase drag). An alternative to this approach, though not used, is to store the parameters of the PDF and droplet velocity profile at each control volume, though this would result in excess computational work.

The complete listing of source terms are given below

Table 2.4: Source Terms

ϕ	q_ϕ
Continuum continuity, 1	$-\sum_k \dot{m}_k - \frac{\delta}{\delta t}(\theta\rho)$
Continuum momentum, $\vec{v}$	$-\theta\left(\mathrm{grad}p - \frac{2}{3}\rho\,\mathrm{grad}k\right) + \rho_d\,\vec{F}_{dr,3}$
Continuum turb. kin. ener., k	$\theta\left(P_k - \rho\epsilon\right)$
Continuum turb. diss. rate, ϵ	$\theta\frac{\epsilon}{k}\left(C_{\epsilon,1}\,P_k - C_{\epsilon,2}\,\rho\epsilon\right)$
Discrete continuity, $\underline{\mu}$	$\underline{q}_{\mu}^{bre} + \underline{q}_{\mu}^{col}$
Discrete momentum, $\underline{\vec{V}}_d$	$-\underline{\vec{F}}_{dr}$
Liquid film, θ	$\dot{m}_{wall} - \dot{m}_{spl} - \dot{m}_{reb}$

where $C_{\epsilon,1} = 1.44$ and $C_{\epsilon,2} = 1.92$. $\dot{m}$ is the "mass" flux. The source term of the liquid film equation represents the difference between the liquid of the injected spray passing
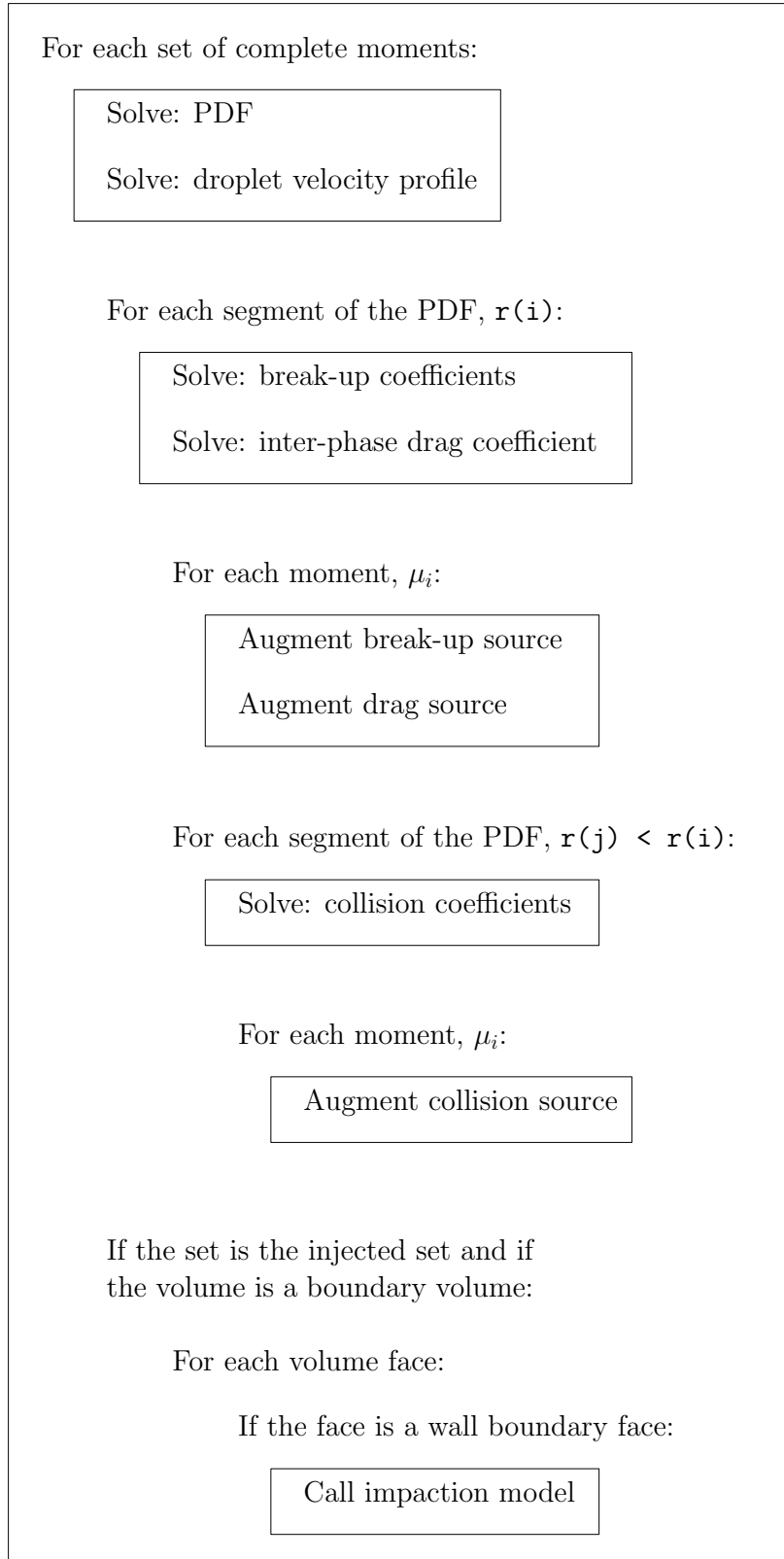
For each set of complete moments:

> Solve: PDF
>
> Solve: droplet velocity profile

For each segment of the PDF, `r(i)`:

> Solve: break-up coefficients
>
> Solve: inter-phase drag coefficient

For each moment, μ_i:

> Augment break-up source
>
> Augment drag source

For each segment of the PDF, `r(j) < r(i)`:

> Solve: collision coefficients

For each moment, μ_i:

> Augment collision source

If the set is the injected set and if
the volume is a boundary volume:

For each volume face:

If the face is a wall boundary face:

> Call impaction model

Figure 2.16: Calculation of spray source terms

out of the domain (through the wall) and the fraction of that liquid which is rebounded and/or splashes, thus remaining in the domain.

2.9.5 Initialization

Equations

For each transported equation, a number of parameters are defined: under-relaxation factor, convection schemes blending, temporal schemes blending, convection scheme (upwind scheme is always used as the implicit scheme; the option is for the explicit scheme) and the initial value of the transported quantity.

Initial turbulent kinetic energy, k_{init}, and diffusivity rate, ϵ_{init}, is based upon characteristic speed, Ch_{spd}, length, Ch_{len}, and turbulent intensity, Ch_{int}. Characteristic speed is approximated as a third of the injection speed, the characteristic length is set as ten times the injection diameter and the characteristic turbulent intensity as five percent. k_{init} and ϵ_{init} are then initialized by

$$k_{init} = 1.5(Ch_{spd}Ch_{int})^2 \qquad (2.135)$$

$$\epsilon_{init} = 2.35\frac{k_{init}^{\frac{3}{2}}}{Ch_{len}} \qquad (2.136)$$

Properties

Viscosity, density and other thermodynamic properties are obtained by temperature-property relations. Initial eddy viscosity is determined from the initial k and ϵ values as

$$\mu_t = 0.09\,\rho\frac{k_{init}^{\frac{3}{2}}}{\epsilon_{init}} \qquad (2.137)$$

2.9.6 Algorithm Platform

The presented methodology is implemented into a suitable algorithm for solving continuum fluid flow. The algorithm follows the procedure detailed in Ferziger and Perić [2002], using the SIMPLER scheme [Patankar, 1980] for pressure-velocity coupling and the $k - \epsilon$ model of Launder and Spalding [1974] for turbulence modelling for high Reynolds num-

ber flow. The domain is discretized in an unstructured manner into finite volumes. The solution of the discretized equations is performed using the Conjugate Gradients type solvers with Incomplete Cholesky preconditioning. Time marching is performed using the Implicit Three Levels method for all transported properties. Convergence of outer iterations is defined by the maximum (1-norm) normalized residual of all transport equations dropping to a predefined level (three orders of magnitude). Each residual is normalized by its maximum in the iterative procedure.

2.9.7 Solution Algorithm

The solution algorithm (Fig. 2.17) is made up of two loops, the latter being nested. The outer loop indexes the temporal progression of the solution and the inner loop performs iterations over all the transport equations until global convergence is obtained for a given time step (or until the iteration index reaches a pre-set maximum). Transported scalars are solved after its associated momentum equation. This ordering enables the volume face speed $(\vec{v} \cdot \vec{n})$ to be calculated and stored during the construction of the momentum equation, then used by the scalar equations in the convection terms.
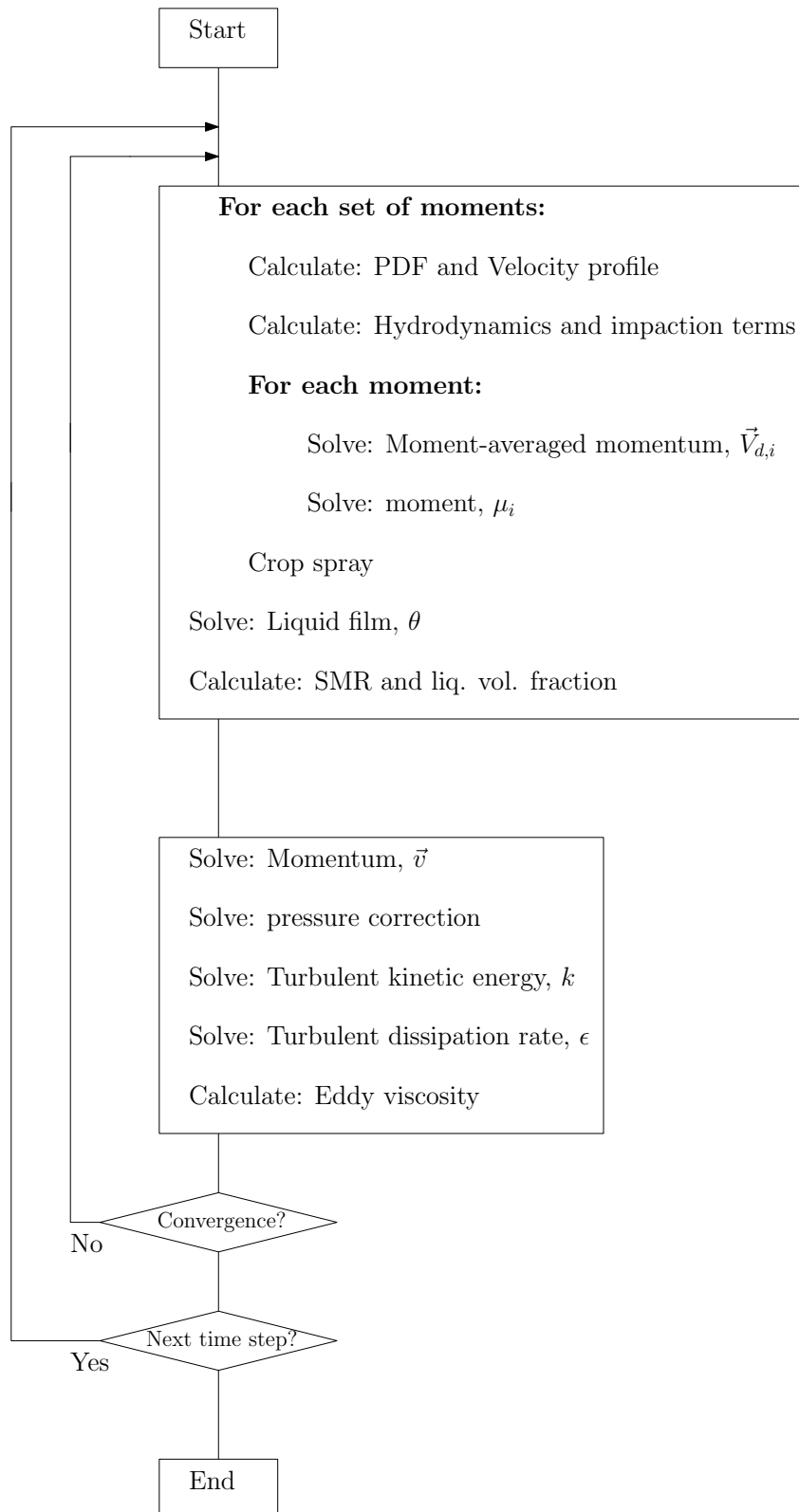
Figure 2.17: Two-phase flow algorithm

If the momentum is related to the transportation of a volumetric-based quantity, such

as droplet volume fraction or mass flow rate, the summated inlet and outlet volumetric fluxes are stored. These quantities are used later to correct the overall volume conservation.

The discrete phase preceeds the continuum phase and employs a predictor-corrector method; the equations are first iterated to bring the residual down to a certain level, whereby the source terms requiring the solution to the underlying distribution are omitted. Once the maximum of the residuals of the moments transport equation have been reduced a sufficient level, the source terms requiring the moments closure are included.

After the discrete phase is solved, the continuum phase is solved in the order described above, but with an additional procedure performed after the momentum and before the continuity (pressure correction) equation. This procedure summates the inlet and outlet volumetric fluxes of both phases and calculates the ratio

$$\frac{(\Theta\, S\, \vec{v} \cdot \vec{n})_{in} + \frac{4}{3}\pi\, (\mu_3\, S\, \vec{V}_{d,3} \cdot \vec{n})_{in}}{(\Theta\, S\, \vec{v} \cdot \vec{n})_{out}} \tag{2.138}$$

This ratio is then used as a multiplier for the outlet fluxes used in the pressure correction equation. This ensures that the source term of the pressure-correction equation tends to zero upon convergence. Equation (2.138) assumes that only the continuum phase exits the domain.

In addition to the standard boundary conditions of inlet, outlet, wall and symmetry for a generic velocity or scalar, special boundary conditions must be implemented for the turbulence model at the wall and the injection and wall impaction of the spray. For the standard boundary conditions, details are given in Ferziger and Perić [2002].

2.9.8 Pressure-Velocity Coupling

Both the SIMPLE and the SIMPLER schemes are implemented in the solution algorithm. Typically, PISO type schemes are used for spray and engine problems [Beck and Watkins, 2003a] to avoid the need to perform outer iterations, though for the spray methodology presented here, numerical tests have shown that outer iterations are required and so the implemented methods are more suitable.

Comparing the performance between the SIMPLE scheme and the SIMPLER scheme for a sample spray case, initial tests showed significant improvement in the rate of convergence using the SIMPLER scheme over the SIMPLE scheme, so the SIMPLER scheme (Fig. 2.18) will be used as the standard method of coupling velocity and pressure.
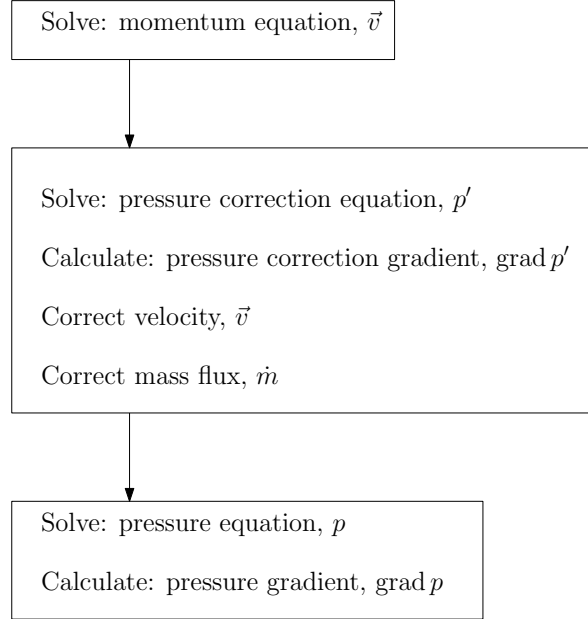
Solve: momentum equation, $\vec{v}$

Solve: pressure correction equation, p'

Calculate: pressure correction gradient, $\mathrm{grad}\, p'$

Correct velocity, $\vec{v}$

Correct mass flux, $\dot{m}$

Solve: pressure equation, p

Calculate: pressure gradient, $\mathrm{grad}\, p$

Figure 2.18: SIMPLER scheme

2.9.9 Linear Algebra Solver

A number of linear algebra solvers for sparse systems of equations are available through libraries such as LASPACK and Sparkit 2. However, to use these libraries, the arguments (ϕ, A and b) must have the proper definition, which is typically

```
real(wp), dimension(1:N_vol) :: phi, b
```

for the variable and right hand side and

```
real(wp), dimension(:) :: A
integer, dimension(:) :: IJA
```

for the matrix storage (such as the New Yale Sparse Matrix format).

However, the structure used for the storage of the transported equations is not of this form (for `phi`). To make the CFD code compatible with the libraries, the stored variable, `phi`, would have to be copied, the linear system then solved, then update the stored variable with the updated variable.

84

To avoid this copying of data, a new linear algebra library was written which accepts `phi` in the form of an array of one-dimensional pointers:

```
type::phi_t
  real(wp), dimension(:), pointer :: vc => null()
end type
type(phi_t), dimension(:), allocatable :: phi
```

The one-dimensional pointer enables `phi` to point to a vector so all the components of the momentum equations are solved in a single call. Figure 2.19 shows how the above structure connects with the data structure of the transport equations.
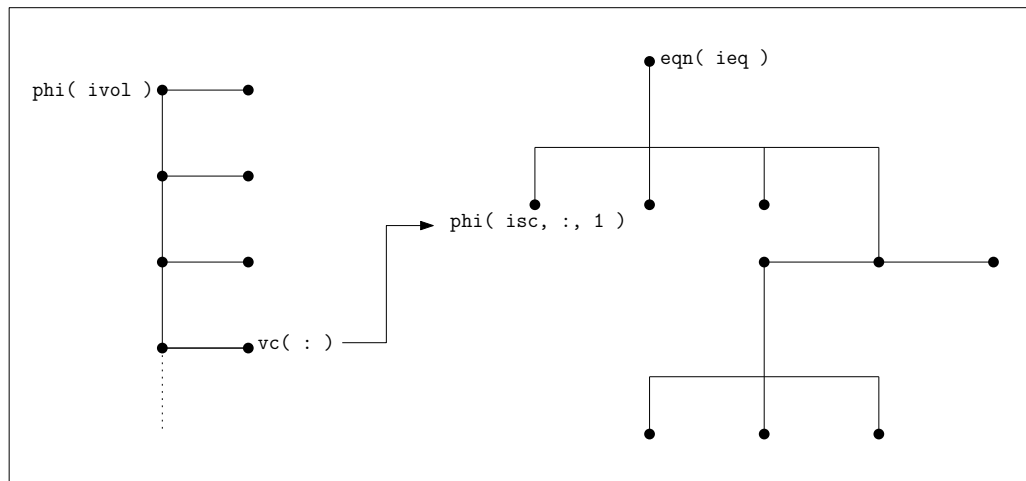

Figure 2.19: Solver variable pointing at the equation variable

Chapter 3

Results

Methods for constructing the droplet size distribution are tested, determining the most appropriate and a similar procedure is performed with the droplet velocity profiles. Parametric tests are then performed on the numerical schemes, modelling parameters and hydrodynamic models. The final form of the spray model is then used to simulate the wall impaction case of Park et al. [2004].

3.1   Distribution Construction

To determine the most suitable method for recovering the probability density function from a finite set of its moments, the methods outlined in Section 2.2 (except the Gamma distribution) are tested by comparing a range of recovered PDFs to the actual PDFs from which the initial set of moments are obtained. The most appropriate reconstruction method will be decided by how many of the sample PDFs are recovered accurately.

The procedure begins by first normalising the radius such that the largest droplet has a normalised radius of one. The moments are also normalised by the same constant. The range $0 < r < 1$ is then segmented into a number of intervals (for the following cases, 50 intervals are used) as shown in Fig. 3.1. Once these preliminary steps are performed, the selected reconstruction method is called.
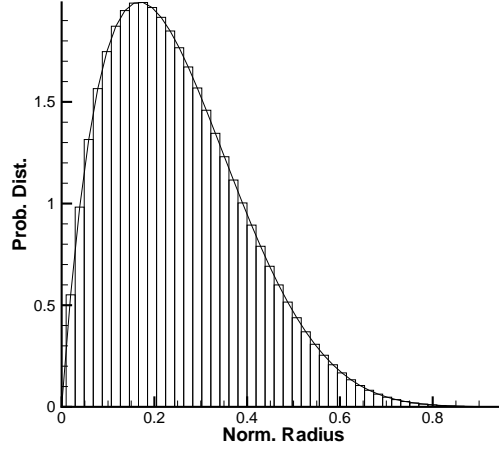
Figure 3.1: Discretization of the distribution

3.1.1 Upper Bound Search

The construction of the splines and Legendre distributions exhibit similar behaviour as the upper limit is reduced from some initial estimate, which is currently taken as $r_{max} = 3.5r_{32}$. As the upper limit is reduced, the oscillations in the shape of the constructed distribution reduce and minima tend towards the positive range (Fig. 3.2). If the limit continues to be reduced, the distribution converges then rapidly diverges after further reduction.

From this knowledge, an algorithm is written that detects when the distribution becomes positive at all discrete radius ordinates, or to find the most accurate distribution allowing for negative values, when an unconditionally positive distribution is not found.

(a) Converging   (b) Solution at 12 iterations   (c) Diverging
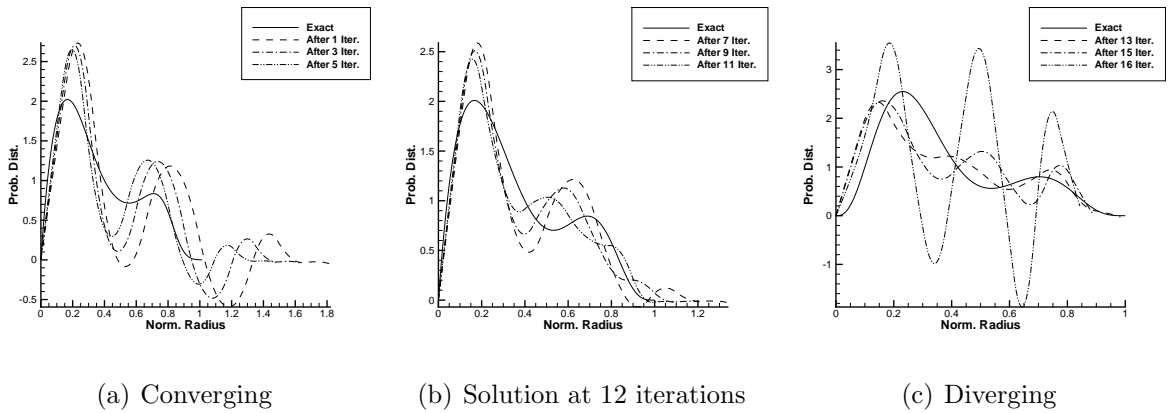
Figure 3.2: Effect of reducing the upper bound.

Maximum Entropy method will construct the same distribution regardless of the limits, so long as the limits are not within the range of the distribution, thus requiring no iterations to optimize the upper bound estimate.

3.1.2   Maximum Entropy Method

The possibility of defining an assumed probability density function, $p(r)$, is exploited (Table 2.2). The main purpose of this is to aid the convergence of the Lagrange multipliers and to improve the shape of the tails of the reconstruction. From a number of simple tests, the Exponential, Rayeigh and Beck [2000] distributions were found to significantly reduce the number of iterations required to converge the solution of the Lagrange multipliers (from approximately 25 iterations to 8) compared to setting $p(r) = 1$. Little difference was found between the recovered distributions which employed the stated a-priori distributions. However, using the distribution from Beck [2000], the lower bound tail was more accurately resolved, compared with the other assumed PDFs (Exponential and Rayleigh).

3.1.3   Splines Method

The splines method has a number of free parameters and can be solved in a number of ways. Because of this freedom, highly accurate reconstructions can be performed using this method, at the cost of determining certain free parameters iteratively for each new solution. Within the context of CFD, computational time is critical, so free parameters ought to be estimated from the outset. This generally results in sub-optimal solutions. The degree of the splines is the primary parameter. Generally, fewer moments are required if higher order splines are used, but may promote oscillations in the shape (Fig. 3.3).
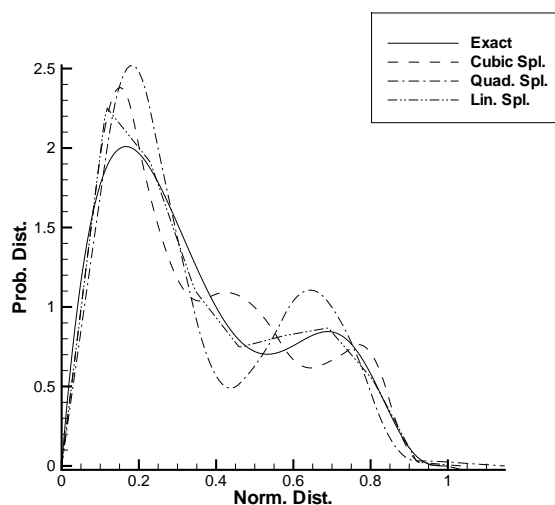
Figure 3.3: Effect of splines order

Since the linear system of equations produced by the Splines method are highly ill-conditioned, the solution is found by calculating the pseudo-inverse. This in turn requires the matrix to be decomposed using singular value decomposition. From the produced set of singular values, the smaller values represent noise in the solution, whereas the the remaining are required for the solution. One method of filtering out the singular values causing noise in the solution is to iteratively discard values, beginning with the smallest, until all the oscillations are removed. This results in a nested iterative process. Alternatively, the singular values can be filtered based on a simple criteria. The filtering technique adopted searches the ordered sigular values from the largest to the smallest. If the difference between two consecutive singular values is found to be greater than an order of magnitude, all singular values after the smaller of the two is set to zero. This procedure is illustrated in Fig. 3.4.
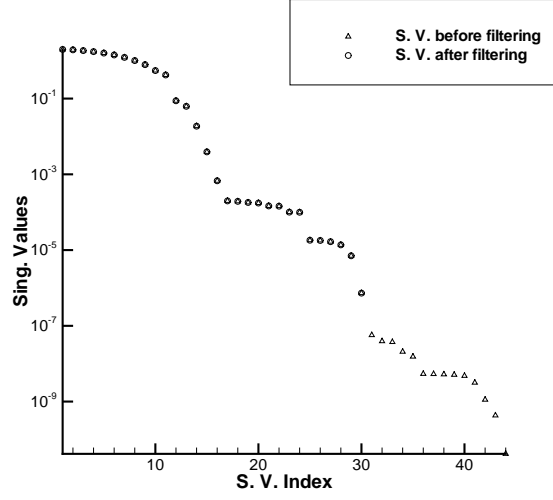
Figure 3.4: Filtering singular values

3.1.4 Sample Distributions

Unimodal distributions are defined using functions

$$\phi(r) \quad = \quad \frac{1}{B(\alpha,\beta)} r^{\alpha-1}(1-r)^{\beta-1} \tag{3.1}$$

$$\phi(r) \quad = \quad \gamma^{\frac{1}{3}}(4r^2(1-r)^2)^{\gamma} \tag{3.2}$$

where Eq. (3.1) is used to construct positive skew distributions and Eq. (3.2) for negative skew distributions. These two distributions are then combined to construct bimodal distributions. The contribution by Eq. (3.2) is halved to produce a diminished second peak, in order to mimic realistic spray distributions.

Maximum entropy, Cubic splines and Legendre distributions are compared to the exact distribution. Different shapes of distribution are tested to show the capacity and reliability of the different methods. Results from the testing of the Laguerre distribution are not documented since the method neither recovered any of the sample distributions accurately nor conserved the input moments (Upto 20% error in the recovered moments). Its relatively poor performance is likely to be associated with the support being defined between zero and infinity, making the choice of normalization difficult, and that the resultant function (the PDF) does not diminish to zero beyond the largest droplet size but fluctuates about the axis, as in Fig. 3.5.

90
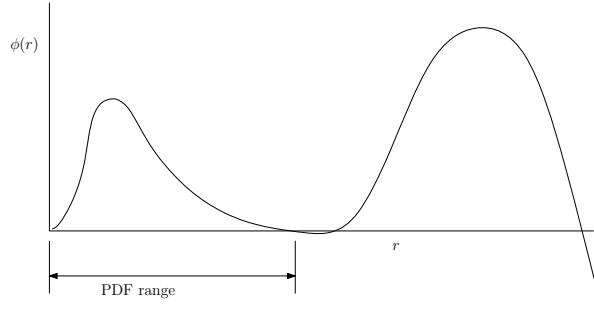
Figure 3.5: Behaviour of the recovered PDF using the Laguerre method

Unimodal

Positive Skew Figure 3.6(a) shows the cubic splines method performing poorly at reconstructing the distribution with a large variance and strong negative skew. Reduction in the variance in Fig. 3.6(b) results in greater wiggling of the tail of the cubic splines reconstruction, whilst the other two methods perform well. Reducing the positive skew towards a bell-shaped distribution, Fig. 3.6(c) shows that the Legendre distribution is unable to recreate the shape, whereas the other methods do and are in good agreement. Finally, reducing the variance of Fig. 3.6(c) results in the distribution in Fig. 3.6(d). In this case the Legendre method does produce a distribution, however at the supports, the magnitude of the gradients are large, producing a broad shape, unlike the other distributions.

From these first cases, the Maximum Entropy method performs consistently well, the Cubic splines method produces poor reconstructions for the highly positively skewed cases and the Legendre method fails to produce a sensible distribution for the weakly skewed case.
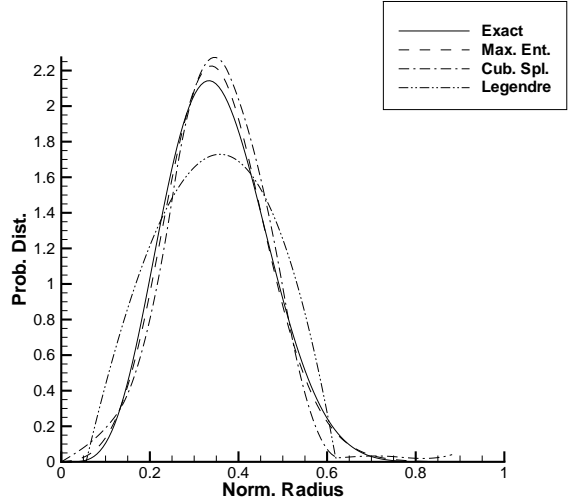
91
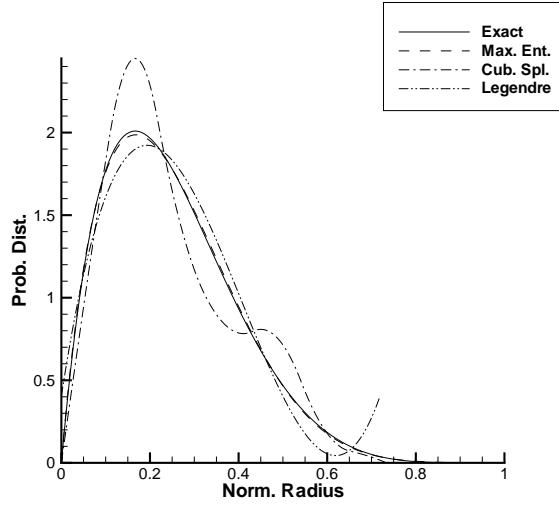
(a) $\alpha = 2$, $\beta = 5$
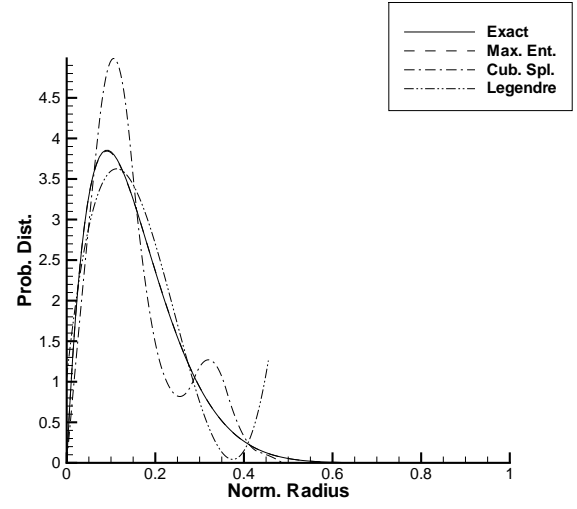
(b) $\alpha = 2$, $\beta = 10$
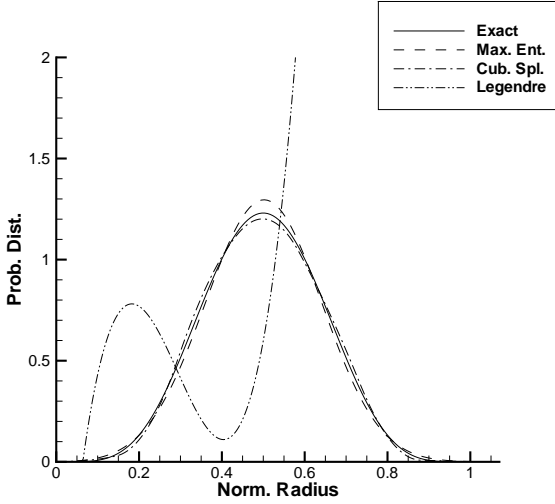
(c) $\alpha = 6$, $\beta = 5$

(d) $\alpha = 6$, $\beta = 10$

Figure 3.6: Distributions with positive skew using the first four moments.

Negative Skew   The Maximum Entropy method and the Cubic Splines method in Fig. 3.7(a) both over predict the peak and produce a tail on the right hand side, though still perform well. Legendre method produces a near perfect approximation. Reducing the negative skew, Fig. 3.7(b) shows the Legendre method failing to produce a sensible approximation. This pattern continues as the variance is further reduced in Fig. 3.7(c) and Fig. 3.7(d). Only in Fig. 3.7(d) does the Maximum Entropy method show a slight advantage over the Cubic splines method in approximating the height of the peak.
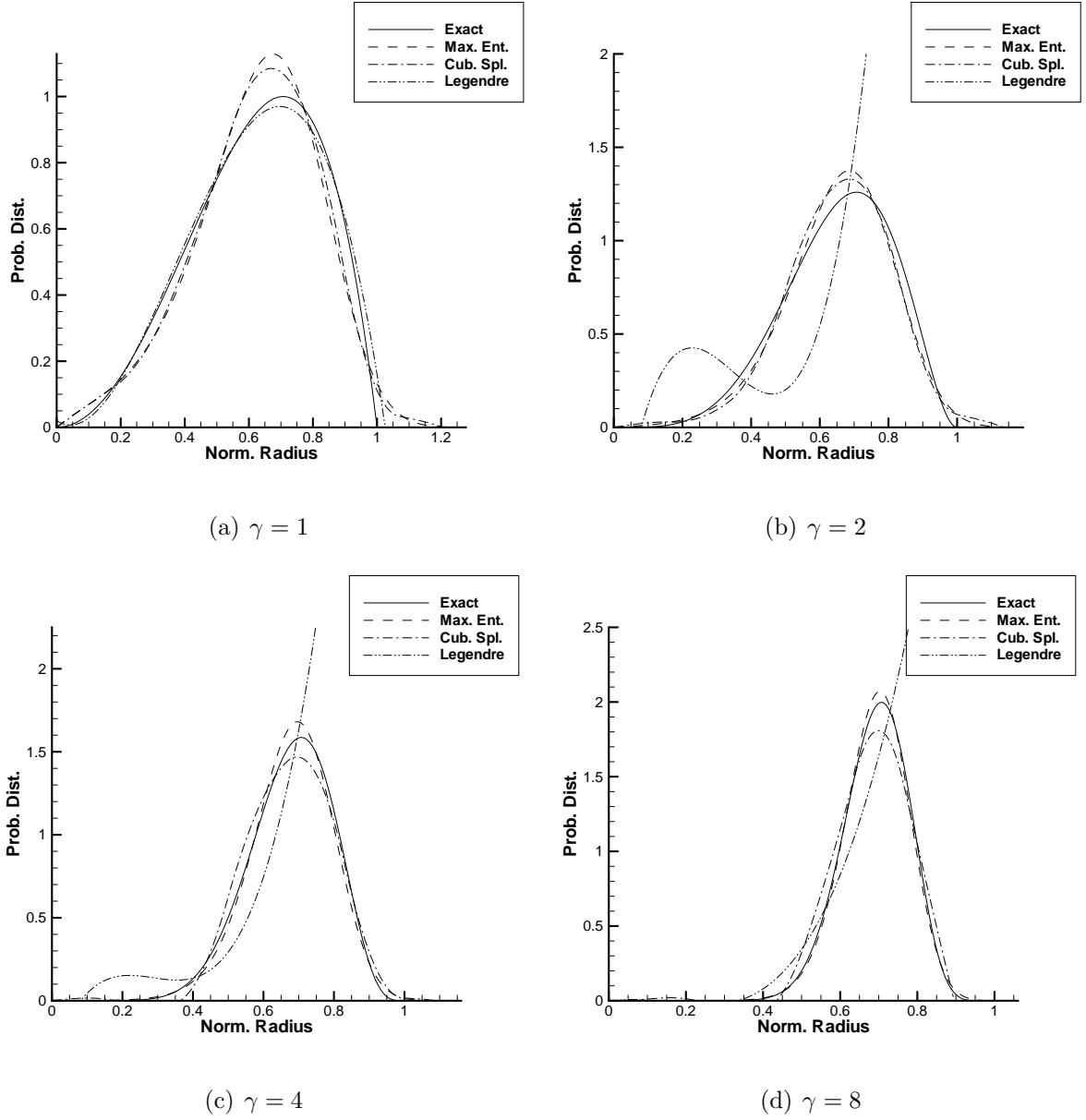
Figure 3.7: Distributions with negative skew using the first four moments.

Bimodal

All methods manage to produce sensible reconstructions for bimodal distributions. Again, Maximum Entropy method consistently performs the best, though the Legendre method produces almost identical distributions for all except that in Fig. 3.8(c). Cubic splines method produces wiggles in the distributions with large variances (Fig. 3.8(a) and Fig. 3.8(b)) and overshoots the peaks of the distributions with lower variances (Fig. 3.8(c) and Fig. 3.8(d)).
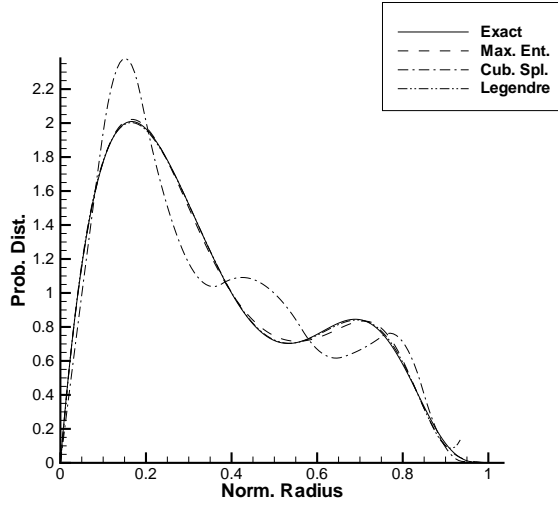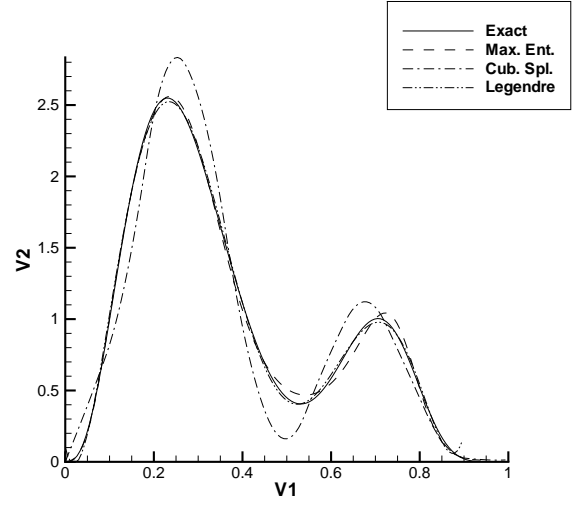
(a) $\alpha = 2$, $\beta = 5$, $\gamma = 4$
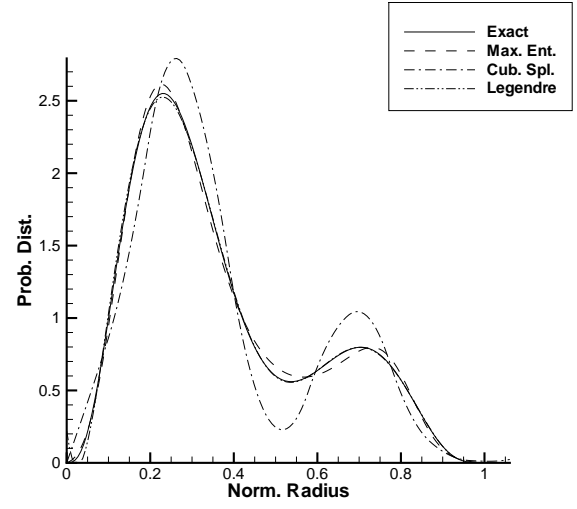
(b) $\alpha = 4$, $\beta = 10$, $\gamma = 4$
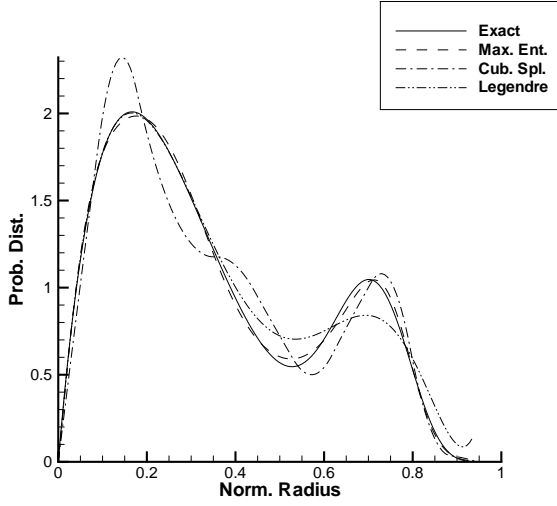
(c) $\alpha = 2$, $\beta = 5$, $\gamma = 8$

(d) $\alpha = 4$, $\beta = 10$, $\gamma = 8$

Figure 3.8: Bimodal distributions using the first eight moments.

3.1.5 Unconditional Solution

In the context of a CFD algorithm, the method for recovering the underlying distribution must be very reliable, that is, for a large range of possible moments which relate to a physically sensible distribution, the method will recover that distribution. Of the cases given above, only one of these methods achieved that condition (at least for the range of cases considered) that is the Maximum Entropy method. This is not to conclude that other methods cannot produce reliable results for a range of cases (see John et al. [2007] for

examples of the Splines method), but given the computational time restriction preventing optimized free parameters being sought (especially in the Splines method), the Maximum Entropy method performs by far the best.

When running the different cases, the moments about the mean were calculated (from Eq. (2.4)). The purpose of this was to find a relationship between values of the moments about the mean and whether the closure method (in this case the Maximum Entropy method) converged or not. For this test only the first four moments were used. From 16 sample tests, for all cases, the following conditions were always met

$$\frac{\frac{r_{10}}{\sigma^2}}{\frac{\sigma^2}{|\gamma_1|}} = \frac{r_{10}\,|\gamma_1|}{\sigma^4} < 2.1 \tag{3.3}$$

and

$$\frac{r_{10}}{\sigma} > 1.1 \tag{3.4}$$

and the Maximum Entropy method always converged. These conditions make use of the mean, variance and skewness of the distribution, thus only require the first four moments. These then provide conditions which can be tested to determine whether the Maximum Entropy method should be called, or whether an alternative should be called if the condition is not met.

A-priori methods can be forced to provide a solution by adjusting their parameters into the valid range if the parameters derived from the moments are out of range. This is a highly desirable quality, since such a method could be called if the conditions above are not met.

3.1.6 Method

As suitable methods for determining the droplet distribution, two are feasible:

1. The Maximum Entropy method is set as the primary closure method, therefore moments from μ_0 must be transported. If closure by Maximum Entropy is not possible (Eqs. (3.3) and (3.4) are not met), the Gamma distribution is employed, using any choice of three consecutive moments, μ_i, μ_{i+1} and μ_{i+2}. The preferred choice would be when i is maximized (see Sect. 3.3.8).

2. The second choice is to use the Gamma distribution exclusively, thus only three moments are transported. This is the simplest method, and closure can be forced when necessary.

In the context of the spray model, transporting the first moment, μ_0, has been unachievable to date due to its relatively rapid decay compared to the transported higher order moments. With the inclusion in this model of a droplet velocity distribution, the problems associated with transporting μ_0 will hopefully be diminished.

Constructing the PDF using the Maximum Entropy method, as shown earlier, does not imply that the first moment, μ_0, must be known. However, attempts to solve the droplet number distribution failed. Only when the integral of the distribution was normalized to equal unity did the algorithm run successfully. In addition, if μ_0 is unknown, $p(r)$ must be set equal to one, preventing the solution from being accelerated and stabilised.

3.2 Droplet Velocity Profile

The two proposed methods for constructing the velocity profile in Sect. 2.3 are presented here using point data obtained from running the case found in Sect. 3.4, whereby the simulation is run for a short duration, using the Maximum Entropy to construct the probability density function and the exponential function to construct the droplet velocity profile.

Data from three points within the spray are taken: the first is close to the injector (Point 1), the second is in the middle of the spray body (Point 2) and the last is close to the inside edge of the spray (Point 3). The extracted point data (the moments, continuum velocity and moment-averaged velocities) is shown in Table 3.1, with the corresponding PDFs at each point shown in Fig. 3.2.

Table 3.1: Extracted data from the spray

Point	μ_0 (mm^{-3})	μ_1 (mm^{-2})	μ_2 (mm^{-1})	μ_3
1	18467.9	169.204	2.03169	0.0294586
2	6201.11	48.2283	0.482322	0.00561636
3	684.43	0.894604	0.00125258	2.70287E-05

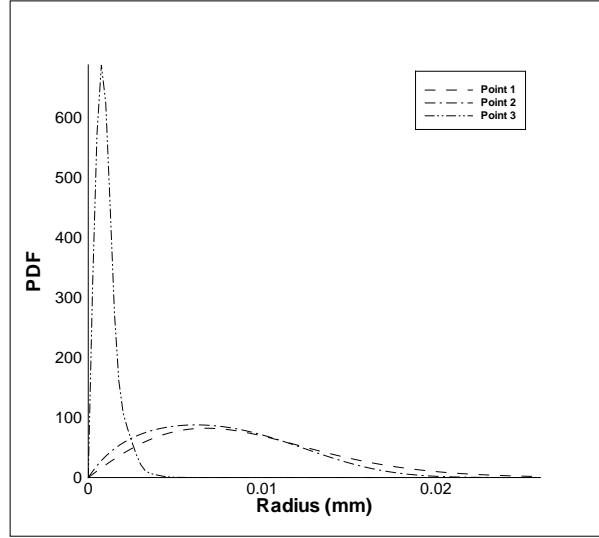| Point	v (m/s)	$V_{d,0}$	$V_{d,1}$	$V_{d,2}$	$V_{d,3}$
1	37.4231	101.471	102.005	102.318	102.437
2	11.1468	74.447	68.5326	65.2815	67.5938
3	1.2158	66.7343	57.5367	50.7085	58.2257

Figure 3.9: PDFs from the extracted moments at points 1-3

3.2.1 Exponential Function

The first method is presented in Fig. 3.10 at points 1-3 for a range of exponent values (0.2, 0.4 and 0.6). The index i in Eq. (2.43) is set as 3. At points 1 and 2, very similar shaped velocity profiles are found since the underlying PDFs are similar and the difference between the continuum and spray velocity at both points is also similar. For the third point, where the underlying PDF has strong positive skew, the droplet velocity picks up slower for the small droplets compared with the droplet velocities at points 1 and 2. For large exponents ($b \geq 0.4$) the velocity profile shows exaggerated values for the larger droplet size range compared with the corresponding moment-averaged velocities listed in Table 3.1.
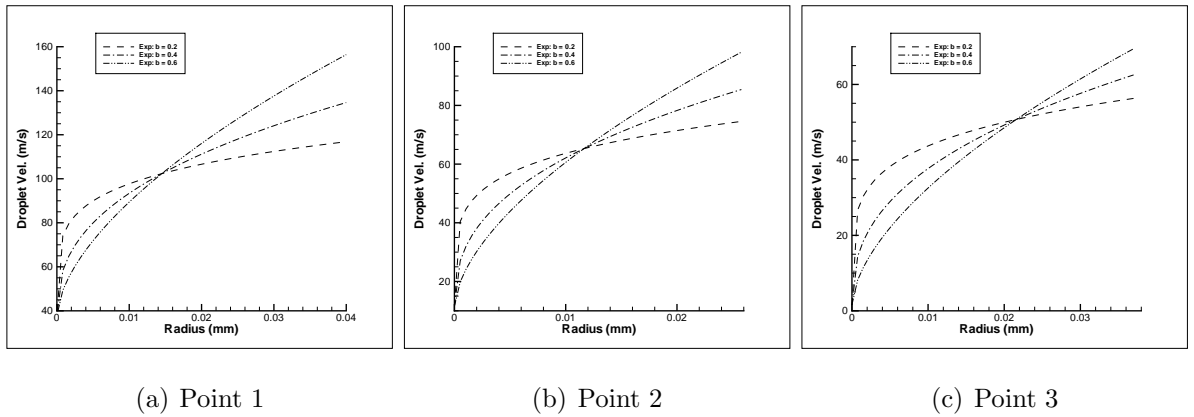

(a) Point 1   (b) Point 2   (c) Point 3

Figure 3.10: Droplet velocity profile based on the exponential function

3.2.2 Polynomial Function

The second method proposed has the capacity to make use of all the available moment averaged velocities to construct the droplet velocity profile, via a polynomial of a predefined degree. Figure 3.11 shows that the profiles for the second and third degree polynomials are very similar (Fig. 3.11(a)) or near identical (Fig. 3.11(b)-3.11(c)) indicating convergence of the profiles. However, only the parabolic velocity profile for point 2 (Fig. 3.11(b)) reflects the drop in the velocities for the intermediate moments, whereas the profiles for the remaining two points show no relation to the velocities they are based on.

The only possible use for this method is if only first degree polynomials are considered. However, the purpose of this method was to propose a means of using all the available moment velocities, which is shown to not be possible. For the spray model then, the first method will be adopted.

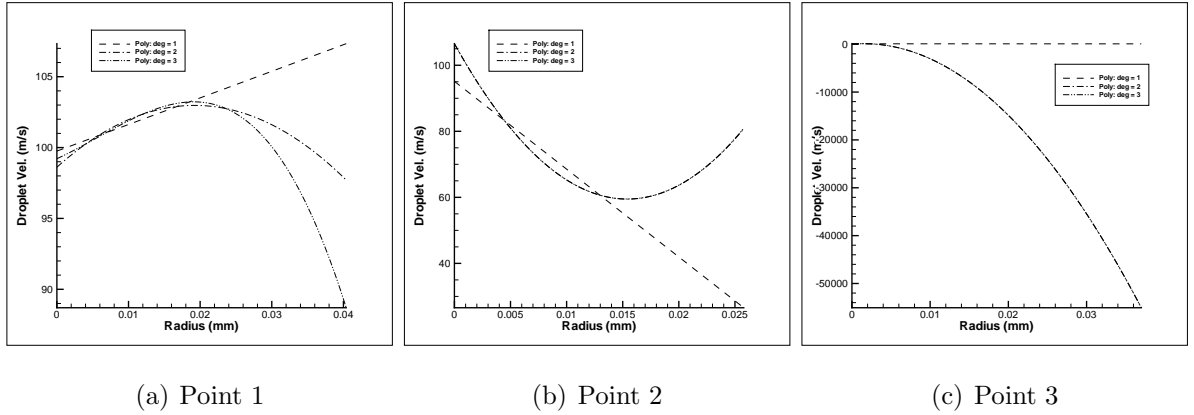(a) Point 1   (b) Point 2   (c) Point 3

Figure 3.11: Droplet velocity profile based on the polynomial function

The unrealistic shape of the resulting profiles using polynomial functions is attributed to the the kind of profile being solved. Unlike the PDF, the velocity profile does not have compact support. The problem this causes can be seen if the product of $\phi(r)$ and $v_d(r)$ were to be solved instead and then $v_d(r)$ recovered from the result. Unreliable values of $v_d(r)$ would be obtained when division of the resultant product by near-zero values of $\phi(r)$ is performed.

3.3 Spray Model Parameters

There are a number of parameters and submodels to choose from in order to define the complete spray model. This section is presented in order to show how the different parameters and submodels effect the overall spray and to come to conclusions about which parameters and submodels are most suitable.

The suitability of the choice of parameters and submodels is defined by meeting two conditions. First, that with a given configuration, the complete spray model remains stable throughout the entire simulation, and secondly, the Sauter mean radius (SMR) is physically sensible in all regions of the spray.

The range of parameters and submodels are listed in Table 3.2, where the initial reference parameters (and submodels) are shown in bold font and ideal parameters are marked by an asterisk. After a parametric case is performed, reference parameters referring to that case may be modified, whereby the modified parameters are used for subsequent parametric cases.

The computational grid, fluid properties and other configuration details of the test cases are exactly the same as those found in Sect. 3.4 detailing the wall impaction case.

Table 3.2: Parameters and submodels

Parameter/submodel	Options
Moments conv. bl. (HRIC)	**0**, 0.3, 0.6, 0.9
Velocity conv. bl. (TVD: Min-mod)	**0**, 0.3, 0.6, 0.9
Break-up model	RD, **PE***, HF
Velocity exponent, b	0.2, **0.4**, 0.6
Collision model	**Off**, On*
SMR at injector, $r_{32,inj}$ (μm)	15, **25**, 35
Skewness of inj. PDF, k_{inj}	3, **7**
Temporal scheme	EI2, **EI3***
Time step, Δt (μs)	1, **2**, 3*
Moments, $P_\mu[-]$	$[1\,2\,3]$, $[\mathbf{2\,3\,4}]$, $[3\,4\,5]$, $[0\,1\,2\,3]$, $[0\,1\,2\,3\,4]^*$

The overall shape of the spray is expected to be strongly effected by the accuracy at which the spray properties are convected and so the convection schemes are assessed

first. Once the choice of blending for the moments and their momentums are decided, the break-up models are compared. As noted in the methodology, only the break-up model of Pilch and Erdman [1987] (PE) covers all break-up regimes for any type of spray so is expected to be the model adopted. However, all three models are compared and are considered as suitable candidates. Velocity exponent is then varied to find out what degree of influence this has on the spray and then the collisions model is introduced.

Parameters of the injected distribution are not expected to have a strong effect on the overall spray. If the SMR is over-predicted, the break-up model should suitably reduce this and the collisions model is expected to compensate to some degree for an excessively positive-skew distribution. Here, this hypothesis is tested.

Comparison between the Euler implicit temporal discretization schemes is performed only to show whether adopting a three time levels method (EI3) makes any noticeable difference to the spray over the two time levels method (EI2). Very little difference, if any, is expected, since geometrical errors are expected to considerably out-weight temporal discretization errors, especially since the grid topology is non-orthogonal.

Convergence with a time step as large as 3μs is not expected, though is tested anyway. For the majority of cases found in Beck [2000], the time step was set as 1μs. With improved temporal discretization (EI3), the possibility of using a larger time step is sought.

Finally, once all the major components of the spray model are set, the choice of transported moments is assessed. For the first three cases, the PDF will be reconstructed using the Gamma distribution, and for the last two cases, the Maximum Entropy method will be used as the primary choice and as the secondary choice the Gamma distribution will be used, based on the three highest order moments available ([1 2 3] and [2 3 4] respectively).

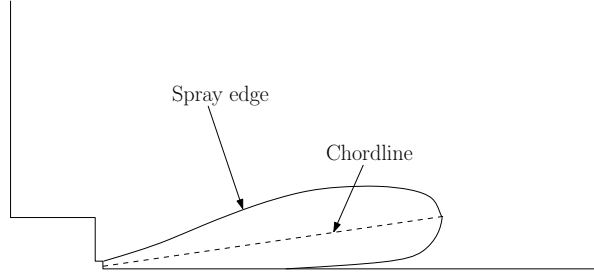*N.B.* All graphed SMR data presented is taken from the chordline of the spray as shown in Fig. 3.12.

Figure 3.12: Chordline of the injected spray

3.3.1 Number of Segments

Before beginning the parametric cases, the number of segments required for the discretization of the PDF and droplet velocity profile is determined by plotting the cumulative inter-phase drag source term (since contributions to the source term are made over the entire droplet size range, unlike break-up and collision terms). Figure 3.3.1 shows that whilst the cumulative term for the range of segmentations is almost identical (the source term can be calculated accurately with as few as 10 segmentations), the intermediate contributions converge with 40 segmentations.
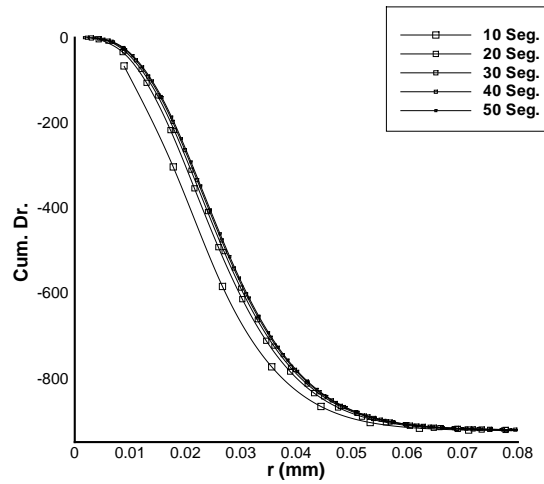
Figure 3.13: Convergence obtained for 40 segmentations

With 40 segmentations, the computational time required to solve the hydrodynamics was found to be disproportionate to the time required to solve the spray transport equations. As a result, the number of segmentations performed on the underlying distributions is reduced to 30.

102

3.3.2 Convection Schemes

The testing of the convection schemes breaks down into two sections; first the spray alone is transported without spray hydrodynamics activated (inter-phase drag and break-up) as a means of testing the boundedness of the transported moments for the various configurations. Once a suitable configuration is found, the hydrodynamics terms are activated and the spray model is tested with the optimal choice of convection schemes blending.

To determine whether the spray is being modelled in a bounded manner, the SMR is calculated. If the SMR deviates from the inlet SMR then the solution is not bounded. Both the TVD scheme and the HRIC scheme are blended with the implicitly implemented UDS scheme. The degree to which the high order scheme is blended with the UDS scheme is listed in Table 3.2.

First, the calculated spray shape is shown in Fig. 3.14 using UDS for both the moments and their momentum. This shows excessive false diffusion, as shown by the presence of the spray above the theoretical outer edge (determined from the injection angle) shown by the grey line cutting through the spray. SMR is constant throughout the spray.
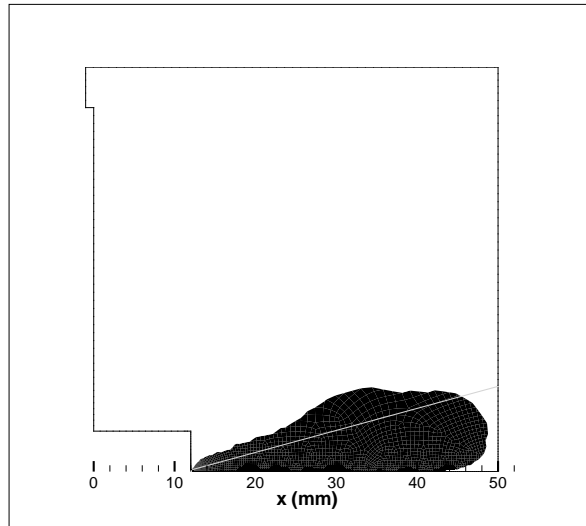

Figure 3.14: Spray shape with pure UDS

103

Moments

The effect of increasing the weighting of the HRIC on the moments is tested first (with UDS for momentum). From Fig. 3.15 the trend shown is that increasing the weighting towards the HRIC scheme, the spray shape becomes more sharply defined, reducing false diffusion. The boundedness condition is perfectly satisfied, as shown in Fig. 3.17.
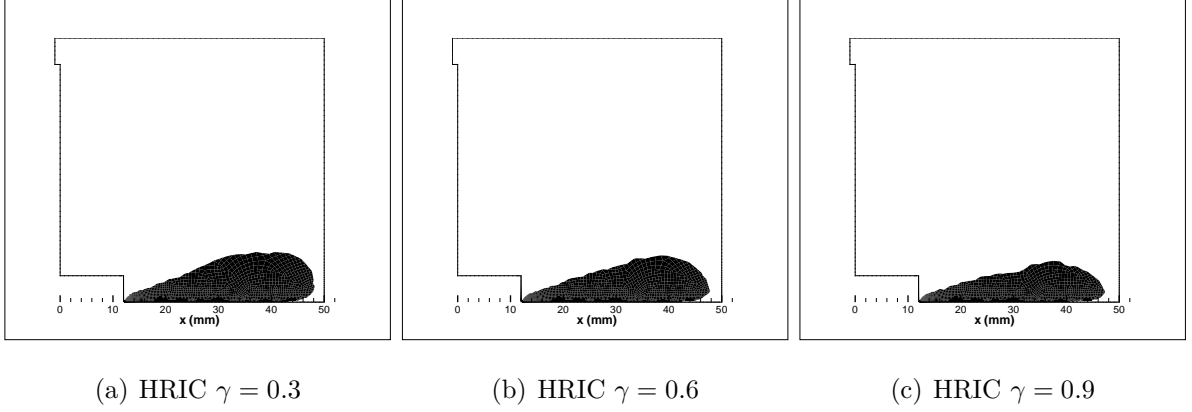

(a) HRIC $\gamma = 0.3$ (b) HRIC $\gamma = 0.6$ (c) HRIC $\gamma = 0.9$

Figure 3.15: Variation of spray shape due to HRIC interpolation
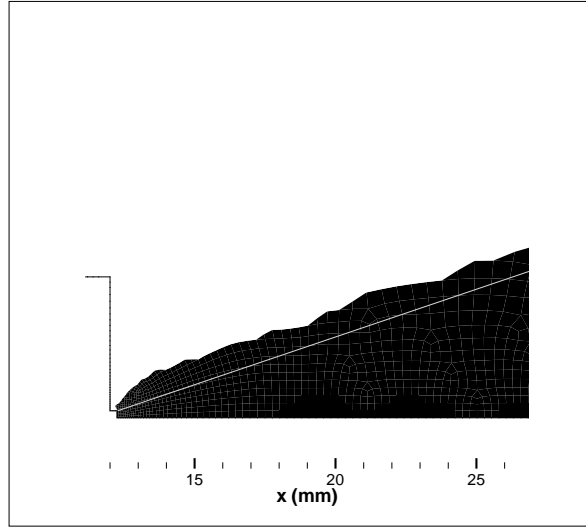
Figure 3.16: Radial diffusion along outer spray edge (HRIC $\gamma = 0.6$)

In addition to sharpening the spray shape, the penetration is reduced slightly with increasing γ, though there remains near-uniform radial diffusion along the outer edge of the spray which is present regardless of the value of the blending constant (Fig. 3.16). This radial diffusion may be related to the manner in which interpolation is performed between

104

radially adjacent CV convection coefficients (particularly μ_i in the flux term $\mu_i[\vec{V}_{d,i} \cdot \vec{n}]$ from Eq. (2.52)). Further from the axis, volumetric values have greater influence so using linear interpolation (which does not account for volumetric change) will tend to exaggerate the influence of the CV values closer to the centreline, causing excess radial spread, as seen in Fig. 3.16.
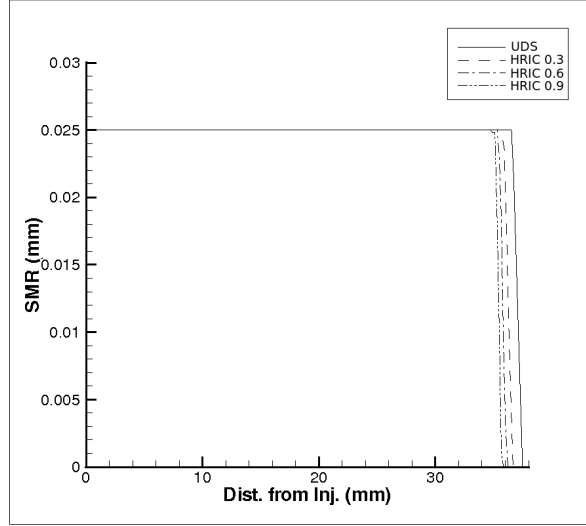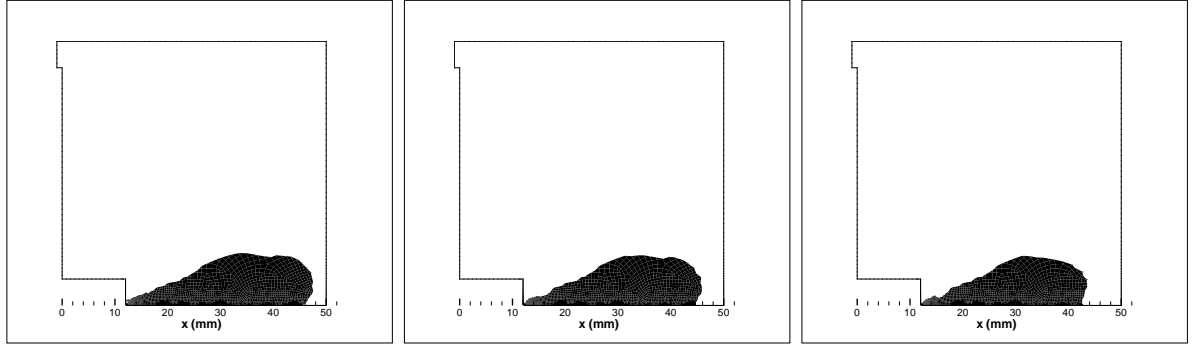

Figure 3.17: Boundedness of spray using HRIC

Momentum

The TVD scheme is the most appropriate higher order interpolation scheme to use for the momentum equations, since central differencing tends to cause unbounded solutions and HRIC is designed for resolving scalars (particularly concentrations). With the TVD scheme, a number of interpolation functions are available, but here only the Min-mod interpolation is tested (with UDS for the moments).

Sharpness of the spray shape is not effected by the increased weighting of the TVD scheme on the momentum (Fig. 3.18), but the penetration is reduced to a much greater degree with the increased influence of the TVD scheme (Fig. 3.19) than compared with the previous case. Again the SMR is perfectly bounded.

(a) TVD: Min-mod $\gamma = 0.3$ (b) TVD: Min-mod $\gamma = 0.6$ (c) TVD: Min-mod $\gamma = 0.9$

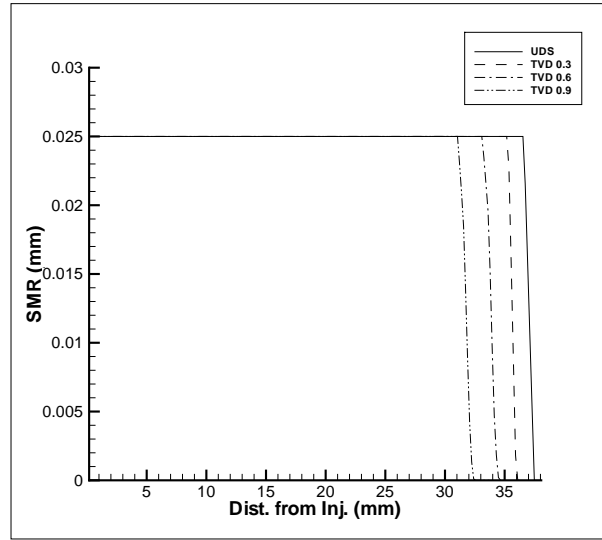Figure 3.18: Variation of spray shape due to TVD interpolation

Figure 3.19: Boundedness of spray using TVD

Moments and Momentum

Combining the blending of both the moments and their momentum, three further cases were performed (HRIC/TVD $\gamma = 0.3$, HRIC/TVD $\gamma = 0.6$ and HRIC/TVD $\gamma = 0.9$). However, only the first case ran successfully and is documented below, in Fig. 3.20. There is no obvious reason why the second and third case failed to run properly since independently, both schemes have been shown to work, though it may be due to the difficulty in converging stiffer sets of the coupled moment and momentum equations. At 30% blending, very little difference is found in the sharpening of the spray or its penetration compared to the pure UDS case.
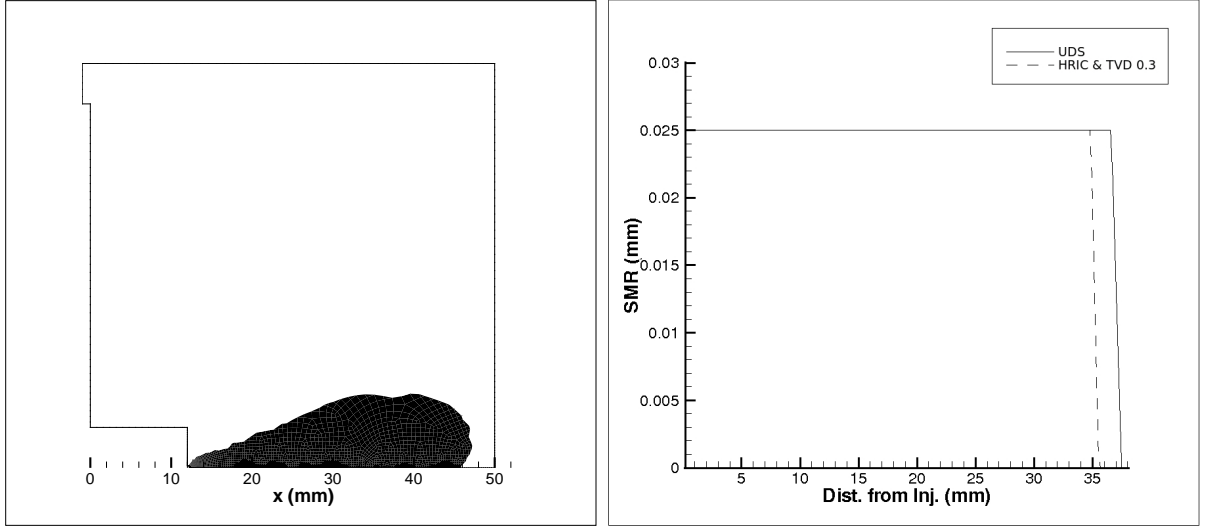
Figure 3.20: HRIC $\gamma = 0.3$ and TVD: Min-mod $\gamma = 0.3$

Optimal Blending

HRIC blending for the moments resulted in the greatest improvement in spray shape by reducing false diffusion, whereas using TVD for momentum, only the penetration was reduced. Combining the HRIC and TVD for the moments and momentum respectively caused the algorithm to become unstable for high degrees of blending.

For HRIC $\gamma = 0.9$, false diffusion is minimized, maintaining a bounded solution so the reference blending parameters are revised to HRIC $\gamma = 0.9$, TVD $\gamma = 0$. With this condition implemented and the hydrodynamics activated, the spray model was run, though as shown in Fig. 3.21, the SMR towards the spray tip was found to be unphysically large. Reducing the blending down to 0.6 presented a much more realistic droplet size variation.

The modification of the convection blending was not expected to have such as strong influence on the resulting SMR but only on the spray shape since its direct effect is only to cause higher concentrations in the spray by resolving its true edge more accurately. Figure 3.21 clearly shows, however, that the degree of blending has significant indirect influence, apparently presenting a choice between compromising on resolution of spray shape or on accuracy of the properties of the spray.

To simplify the problem, the reference break-up model (PE) was turned off and the

HRIC $\gamma = 0.6$ and HRIC $\gamma = 0.9$ spray simulations were run again, leaving only in inter-phase drag model active. Figure 3.21 shows that without the break-up model on, the spray SMR for both cases are very similar, showing that the HRIC scheme is only influencing the spray shape, as expected, indicating that activation of the break-up model and variation of the HRIC blending somehow promotes a significant changes in the spray.

The prediction of the SMR becomes worse for larger values of γ when the break-up model is active. Both the break-up source term and the HRIC scheme augment the right-hand side of the moments equations. When the break-up model is off, the moments equations are much less stiff than when break-up is on, making the equations much easier to converge, thus consistent behaviour is found (with regards to the SMR) for various values of γ .

The normal way to treat stiff equations is to under-relax the solution scheme. However, the moments and momentum equations are already solved with relatively low under-relaxation factors (0.7 for all spray equations are used, whereas Beck [2000] performed no under-relaxation). This apparently leaves no clear alternative than to make a compromise between spray shape accuracy and the accuracy of the SMR, thus the reference blending parameters are set to HRIC $\gamma = 0.6$, TVD $\gamma = 0$. To attempt to resolve the problem, the only clear way forward would be to revise the entire iterative solution scheme for solving the spray related transport equations, by introducing a robust predictor-corrector algorithm. This task however, is beyond the scope of the project.
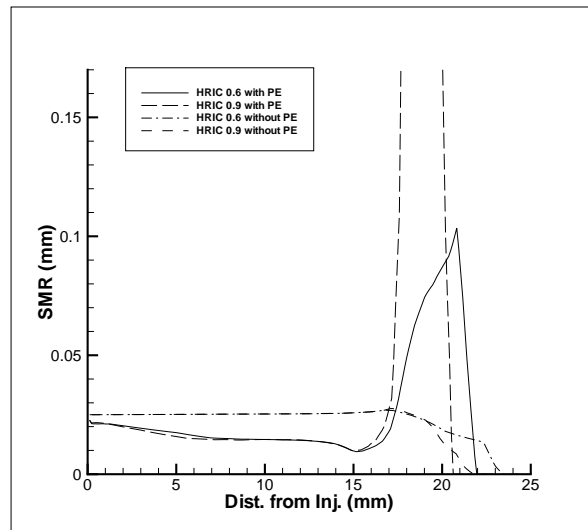

Figure 3.21: Effect on the SMR by HRIC and break-up

3.3.3 Break-up Models

Droplet break-up is shown to have a significant effect upon the spray, as shown in Fig. 3.22(a) - 3.22(b). From the comparison of the effects on the SMR by the models, two are found to be unsuitable; the models of Hsiang and Faeth [1992] (HF) and Reitz and Diwakar [1986] (RD). These models excessively break up droplets, resulting in a large increase in the lower moments (momentarily reducing the SMR) which causes a rapid increase in drag for their corresponding velocities (particularly the lower moment-averaged ones), leading to very large SMR at the leading edge of the spray. Only the model of Pilch and Erdman [1987] (PE) performs reasonably well, producing large SMR at the front end, but not to excess (Fig. 3.22(a)). This break-up model is now set as the revised break-up option.

The reason why two of the models appear to perform poorly is not because of the models themselves but rather that those two models are only suitable for secondary break-up processes, where primary break-up is assumed to already have taken place. The spray model is not implemented with such a condition assumed. The model of Pilch and Erdman [1987] compensates for this since it deals with the break-up of both primary and secondary droplets and is set as the revised parameter for this case.
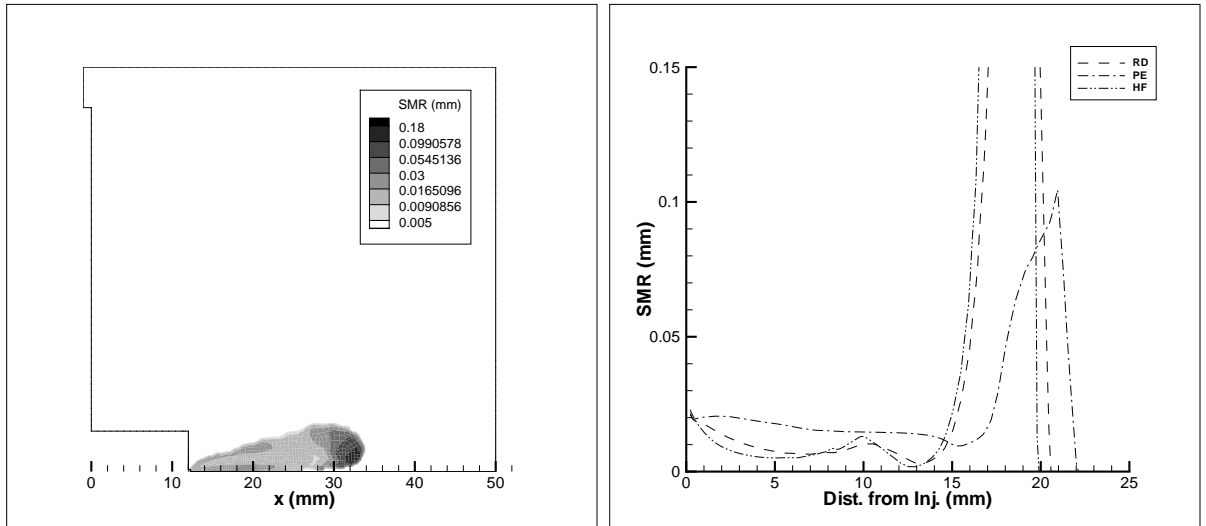

(a) Effect of break-up using PE model

(b) Comparison of break-up models

Figure 3.22: Effect of break-up models

3.3.4 Velocity Exponent

Since the polynomial based velocity-radius function showed such poor trends, only the exponential function is employed. This function has one free parameter, the exponent, b. To obtain a uniform distribution $b = 0$, and for a linear distribution, $b = 1$. Within that range, values for the exponent are considered. Before numerical tests on the spray are performed, the effect on break-up, collision and inter-phase drag models are assessed based on data at point 1 (Table 3.1), whereby the source terms relate to μ_0 for break-up and collisions and $V_{d,0}$ and $V_{d,3}$ for inter-phase drag. The effect of varying exponent b on the hydrodynamic terms are shown in Fig. 3.23 for break-up and collisions and Fig. 3.24 for inter-phase drag.
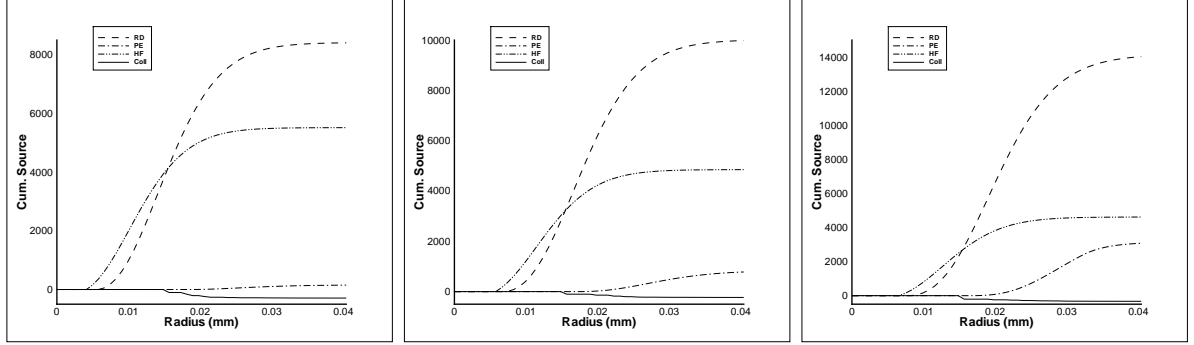
(a) Velocity exponent, $b = 0.2$ (b) Velocity exponent, $b = 0.4$ (c) Velocity exponent, $b = 0.6$

Figure 3.23: Cumulative break-up model terms and collision term at point 1

Of the three break-up models, HF shows virtually no change in value for the range of exponents tested, whereas both RD and PE (the selected model) do. The influence on the collision source is minimal. Comparison between the change in drag due to variation of the exponent for both the first and fourth moment highlight how spray edge SMR can be controlled to a degree. The drag source term for $V_{d,3}$ is virtually unaffected by variation in b, unlike the drag source term for $V_{d,0}$ where the magnitude is significantly reduced when the exponent is increased from 0.2 to 0.6, enabling the lower moments to convect more readily, reducing the likelihood of producing exaggerated SMR.
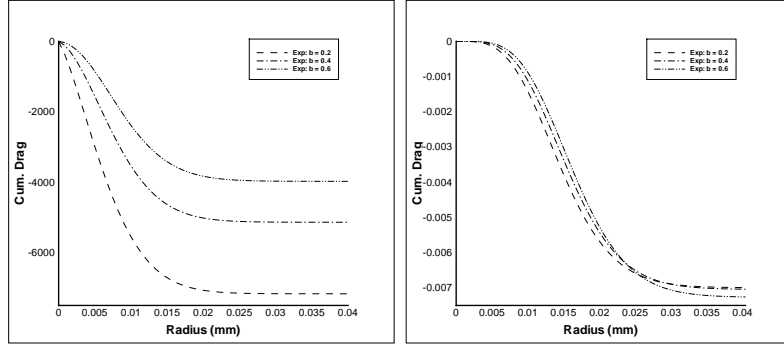
(a) Drag term for $V_{d,0}$ (b) Drag term for $V_{d,3}$

Figure 3.24: Cumulative drag terms at point 1

With exponents of 0.2 and 0.4, over-prediction of the leading edge SMR was found (Fig. 3.25(b)). Only by further increasing this value to 0.6 did the SMR drop at the front end of the spray, as shown in Fig. 3.25(a), thus the reference exponent is modified to 0.6. Even with such a large exponent as 0.6, the leading edge SMR does eventually pick up once the spray becomes more developed, as documented in Sect. 3.4.

An exponent of 0.6 tends to push up the velocity of the larger droplets beyond what is sensibly expected. Consider the data at point 1 in Table 3.1; the moment-averaged velocities are all around 102m/s, though Fig. 3.10(a) shows the constructed droplet velocity range between 40 and 160m/s, whereby the lower bound is dictated by the continuum velocity. Clearly, 160m/s is well beyond the range of the moment-averaged velocities indicating unrealistic modelling of the droplet velocities. However, at present this is the only working configuration and so it is used.

The effective upper limit of the velocity profile can be determined by looking at the associated cumulative source terms. Break-up, collision and drag models (in Fig. 3.23 and Fig. 3.24) show effectively no further contribution after 0.03mm, which corresponds to approximately 140m/s, presenting a more realistic velocity range.
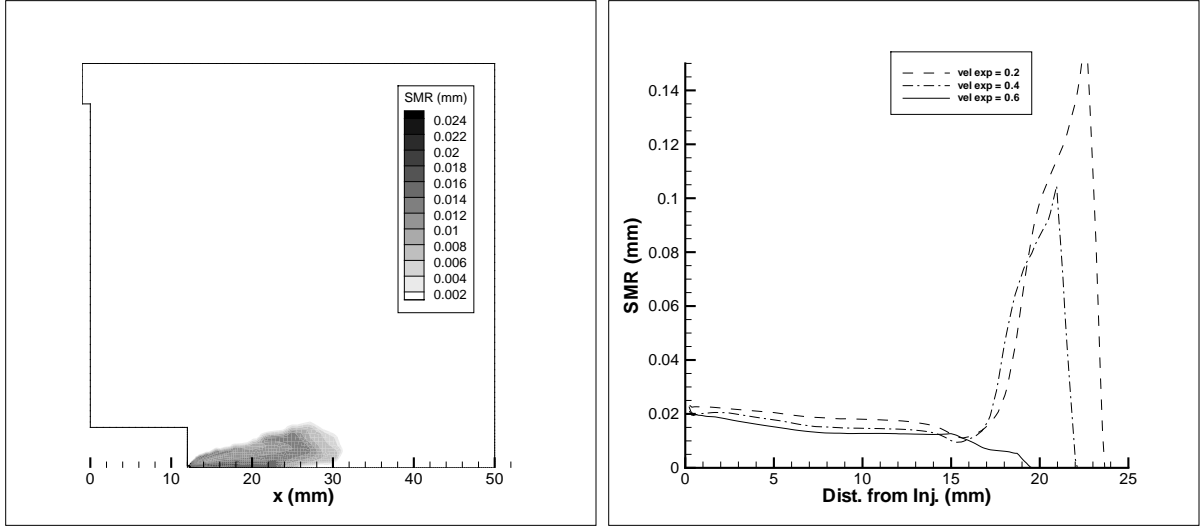
(a) Velocity exponent, $b = 0.6$ (b) SMR for $b = 0.2$, 0.4 and 0.6

Figure 3.25: Variation of velocity exponent

3.3.5 Collisions Model

The introduction of the collisions model is expected to have the opposite effect (to some degree) on the spray compared to the break-up model. When the model is active, smaller droplets are coalescing to form larger droplets resulting in a reduction in the lower moments, manifested by an increase in the SMR. This in turn will effect the drag terms, but not to the same degree that break-up does. This behaviour is shown in Fig. 3.26, comparing the SMR with and without the collisions model activated.
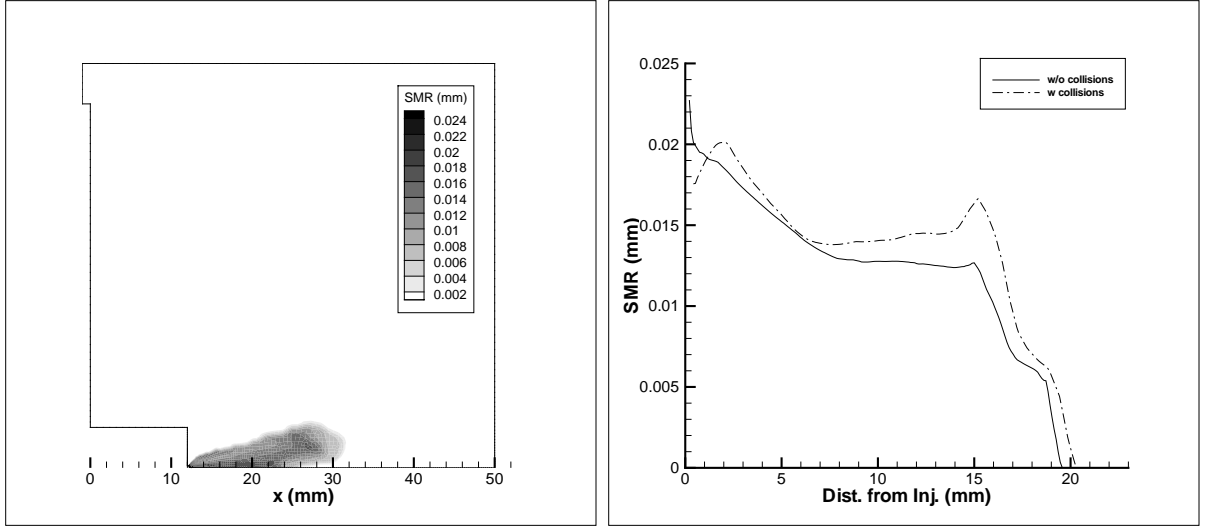
Figure 3.26: Activation of the collision model

From this stage the following cases include the collisions model.

3.3.6 Injection Parameters

As expected, neither modifying the injection SMR nor the skewness of the injected PDF had significant effect on the overall spray (Fig. 3.27). The only noticeable difference was that penetration was slightly increased for $r_{32,inj} = 15\mu$m. This is unusual since larger droplets retain their momentum more readily, generally causing greater penetration. This early spray development may be due to the break-up model (PE) having little effect on the spray with injection SMR of 15μm, whereas for larger injection SMRs (25 and 35μm) the break-up model becomes active, reducing the penetration.
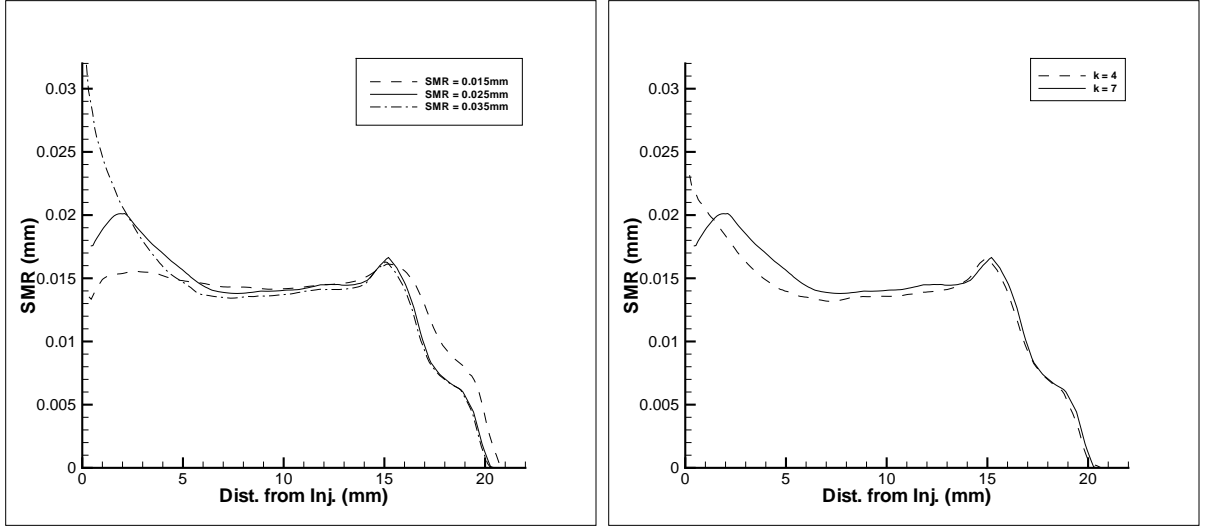
(a) Variation of injection SMR

(b) Variation of injection skewness

Figure 3.27: Variation of injection parameters

3.3.7 Temporal Discretization

Time step values are based around those used by Beck and Watkins [2002]. With the implementation of second order temporal interpolation, larger time steps are tested. Stability of the algorithm will be reduced with the increase of the time step, though a maximum value at which the algorithm remains stable and gives accurate results is sought.

Variation in the time step (Fig. 3.28(b)) shows very little difference in both the penetration and SMR, though 2μs will still be used for the calculations. Greater difference is shown between the choice of scheme (Fig. 3.28(a)). The penetration is noticeably different, with the Three levels discretization causing a reduction. This shows that the revision of the temporal scheme has been worthwhile.
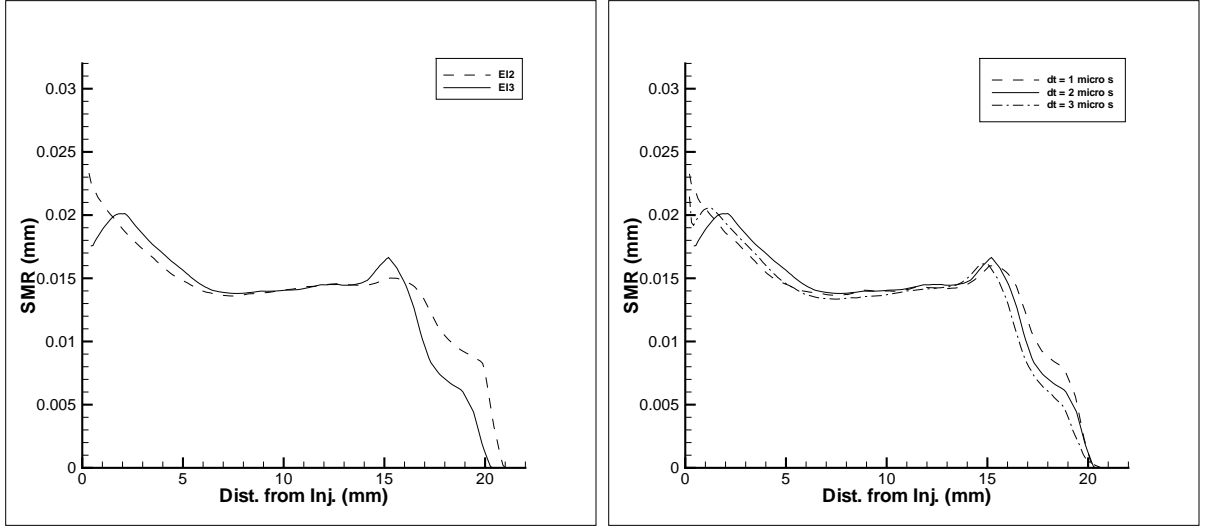
(a) Temporal scheme effect   (b) Time step effect

Figure 3.28: Variation of temporal parameters

3.3.8 Moments

If the Gamma distribution is used as the method of recovering the droplet size distribution, only three consecutive moments are required. Whilst any starting index is possible, the range of starting indices is chosen such that the volumetric based moment, μ_3, is always transported. This is done so volume fractions of both phases are solved explicitly, rather than being derived from the recovered distribution, thus volume and mass concentration are more assured. Alternatively, if the Maximum Entropy distribution is used, consecutive moments from μ_0 must be transported. This means that at least four moments must be transported to include μ_3. However, five moments must be transported to represent the main quantities used to represent a distribution (mean, variance, skewness and kurtosis).

Of the five cases listed in Table 3.2, the last two did not run to completion ([0 1 2 3] and [0 1 2 3 4]). The reason why comes to light when the first three cases are examined ([1 2 3], [2 3 4] and [3 4 5]). Of the first three cases (Fig. 3.29) the last two show strong resemblance, whereas the first case shows a huge increase in SMR at the leading edge of the spray. This shows that as lower moments are transported, the accuracy of the model degrades. The droplet velocity profile has already been shown to have a significant effect on the lower moment drag terms (Fig. 3.24) whereas for higher moment velocities,

the shape of the profile causes only minor differences in the inter-phase drag. Unless the droplet velocity profile is accurately represented, divergence between low order moments is likely to occur resulting in the over-estimation of SMR found in Fig. 3.29 and in the first two cases referred to above.

From the comparison of the first three cases, the reference transported moments are revised, becoming μ_3, μ_4 and μ_5, based on the trend that the further away from low order moments, the more stable the algorithm will be.
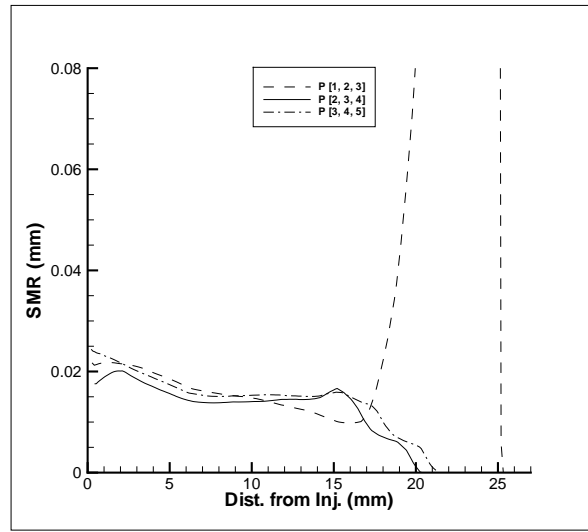

Figure 3.29: Choice of moments for the Gamma distribution

3.3.9 Parameters

The revised default parameters and submodels options are listed in Table 3.3. Of the nine parameters tested across their ranges (Table 3.2), varying four of them caused the spray model to diverge for some values (convection blending, break-up models, velocity exponent and moments). Of these four parameters, all of them are considered as key parameters in the spray model.

Table 3.3: Revised parameters and submodels

Parameter/submodel	Option
Moments conv. bl. (HRIC)	0.6
Velocity conv. bl. (TVD: Min-mod)	0
Break-up model	PE
velocity exponent, b	0.6
Collision model	On
SMR at injector, $r_{32,inj}$ (μm)	25
Skewness of inj. PDF, k_{inj}	7
Temporal sch.	EI3
Time step, Δt (μs)	2
moments, $P_\mu[-]$	$[3\,4\,5]$

From the list of revised parameters, a final case is run whereby the geometry is modified to allow the spray to propagate freely, and the runtime is extended to two milliseconds. This test aims to show whether the spray calculations remain stable over long durations and to show whether the SMR remains at a sensible level.

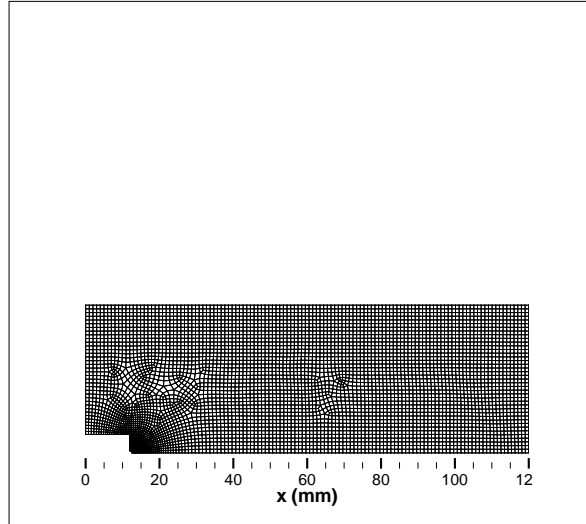The grid used for this case is shown in Fig. 3.30.

Figure 3.30: Computational domain for open-ended case (5271 CVs)

The results revealed that whilst the algorithm remained stable, by 1.4ms the SMR had grown at the leading edge of the spray by over an order of magnitude from the injection SMR of 25μm, as shown in Fig. 3.31.
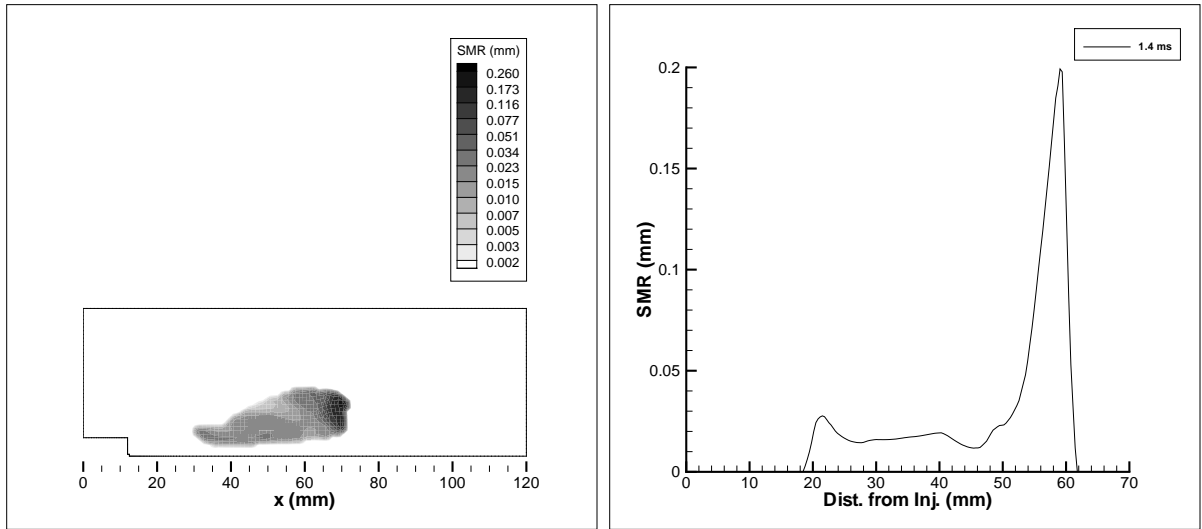
117

Figure 3.31: Sauter mean radius at 1.4ms

From this open-ended spray case and from the set of parametric cases, a preliminary conclusion can be drawn about the state of the presented spray model: the spray model becomes increasingly less accurate as it propagates. For the wall impaction case, this is not a problem since the wall prevents the spray from propagating, though for many other cases where the spray is not restricted, at present the spray model is not capable of simulating these accurately.

3.4 Wall Impacting Spray: Park, et al (2004)

The experimental cases of Park et al. [2004] were performed to present a simplified analysis of late injection stratified charge mode found in direct injection engines. The spray model developed in this work will be used to replicate one of the experimental cases computationally in order to assess its performance at both simulating the spray and modelling the spray interaction with a wall.

3.4.1 Case Parameters

Geometry

The computational grid (Fig. 3.32) is arranged such that the injector tip is situated 38mm in front of the wall on which the spray impacts. The narrow-cone pressure-swirl injector operating at 6.8MPa producing a nominal cone angle of 20 degrees is assumed here to have an orifice radius of 0.25mm. The injector tip is shown as a bluff-body in the bottom left-hand corner of the grid.
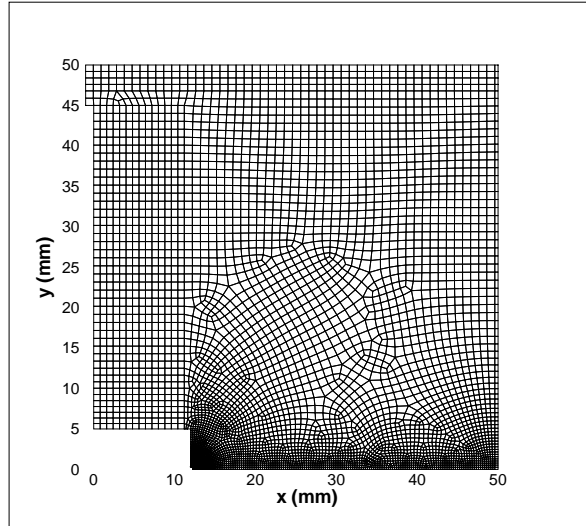

Figure 3.32: Computational domain for wall impaction case (5103 CVs)

Grid refinement is shown around the injector forming five injector inlet faces (Fig. 3.33(a)), along the line of symmetry. A relatively coarse layer of cells is found along the right hand side of the grid, where the impacting wall boundary is defined (Fig. 3.33(b)). This coarse layer is designed to avoid the liquid volume fraction in the near-wall cells

becoming over-full. Finally, the protrusion at the top left hand corner of the grid is the outlet, situated far away from the spray. The outlet is necessary in this case since the flow is assumed to be incompressible.
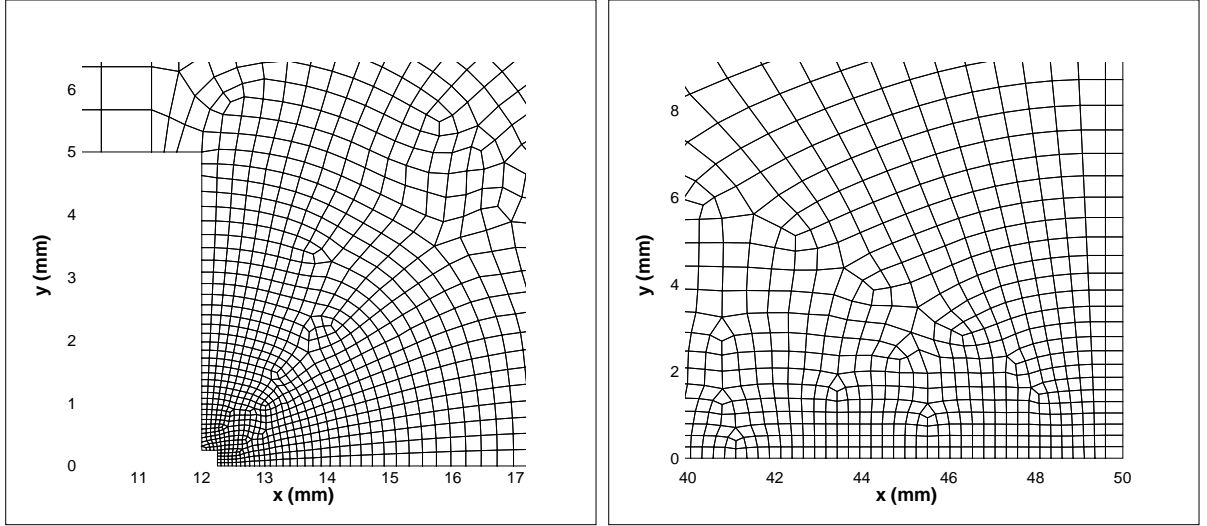

Figure 3.33: Injector and wall treatment

No grid independence testing is given here for two reasons. First, the grid presented is finer (in the areas of interest) than the grids used by Beck and Watkins [2003a] and Lemini [2004]. In their grids, the injector was resolved with a maximum of three cells. Secondly, this is as fine a grid as can be afforded for this study, with the algorithm taking around 8 hours to complete (spray source terms plus twenty seven partial differential equations are solved per iteration).

Fluid Properties

The case is run at room temperature with an elevated pressure of 4.7kPa, giving a air density of 5.5kgm^{-3}. Molecular viscosity is taken as 1.846x10^{-5}kgm^{-1}s^{-1}. Iso-octane is the injected fuel, having a density of 702kgm^{-3} and viscosity of 5.65x10^{-5}kgm^{-1}s^{-1}. Surface tension coefficient between air and Iso-octane is 0.0226kgs^{-2}.

Injector Conditions

Injected Sauter mean radius is set as one tenth of the injector orifice radius to 25μm and the skewness parameter $k = 7$. Spray velocity and continuum velocity are assumed to be

equal and are controlled by the discharge profile, $p_1(t)$, presented earlier. The profile is applied to both the velocities and the moments. Injection duration (pulse width) is set as 0.5ms with the rise time (δt in Fig. 2.9(a)) set as 0.025ms. The rise time is an overestimate (it should be approximately 0.01ms), because divergence occurs if the injector is turned off too quickly.

Modelling Parameters

Droplet velocity profile exponent is set to 0.6. Both the break-up model of Pilch and Erdman [1987] [PE] and the collision model are employed. For determining whether the full set of moments are present in a given volume, the multiplier, C_μ, is set to $1\text{x}10^{-7}$. The underlying distribution is assumed to be a Gamma distribution and the moments μ_3, μ_4 and μ_5 are used to determine its parameters. All terms related to the PDF and velocity profile are solved using numerical integration, discretized with 30 segments. Ideally the distributions should be divided into at least forty segments, though this is not done because of the computational cost incurred.

Discretization

Second order Euler implicit temporal discretization [EI3] is used for all transport equations, with a constant time step of 2μs. The convection discretization is detailed in table 3.4. No high order convection scheme is used for the moment-averaged momentum equation. Eddy viscosity is under-relaxed by the same constant used for the turbulence equations. Relatively low convection blending is used for the turbulence modelling to stabilize the algorithm.

Table 3.4: Discretization Parameters for wall impaction case

Transport equation	Under-relaxation	Convection blending
Continuum momentum	0.7	0.9 (TVD: Min-mod)
Continuum turbulence	0.65	0.5 (TVD: Min-mod)
Discrete momentum	0.7	0
Discrete continuity	0.7	0.6 (HRIC)

Two iterations are performed on all gradient calculations, dropping the error one

order of magnitude. Further iterations of the gradient showed very little gain in accuracy. Pressure and pressure correction are interpolated from the near-boundary CVs to the boundary after the first iteration.

Initialization

Only the turbulent kinetic energy and dissipation rate require non-zero domain initialization. Values of these are sought such that the resulting eddy viscosity is as small as possible without causing the algorithm to diverge early in the solution procedure. Over-estimation of eddy viscosity has been found to excessively resist the acceleration of the continuum phase.

The characteristic length scale of the initial turbulence is assumed to be 1cm with a velocity of 40m/s at 20% intensity, giving initial eddy viscosity one hundred times greater than the molecular viscosity.

Algorithm

Outer iterations are limited to 20 and is assumed to converge once the global maximum normalized (1-norm) residual has dropped three orders of magnitude. Inner iterations (of the linear system) are required to drop the residual one order of magnitude.

3.4.2 Penetration and Impaction

Figure 3.34 from Park et al. [2004] shows the development and impaction of the spray, showing that impaction occurs at some time between 0.4 and 0.9ms. Cross-referencing this with the earliest recorded near-wall Weber numbers in Fig. 3.43 - 3.46, impaction is most likely to have occurred around 0.9ms after the start of injection.

Figure 3.34: Spray from 0.4ms at intervals of 0.5ms

From Fig. 3.34 taken from Park et al. [2004], the spray half-cone angle is estimated as being 27 degrees. However, the cone angle is stated as being 20 degrees, implying a half-cone angle of 10 degrees. Clearly there is a discrepancy, so for the computational case a compromise is made by setting the half-cone angle to 20 degrees.

In the same figure, penetration at 0.4ms is shown to be approximately 16mm and at 0.9ms the spray reaches the wall, which is 38mm from the injector. This implies that the spray accelerates towards the wall, which is highly unlikely. A more likely explanation is that the first image in Fig. 3.34 corresponds to an earlier time. Comparing the first two images in Fig. 3.34 with the profiles in Fig. 3.35, good correlation of the spray shape is found at 0.9ms, especially at the front end of the spray. The experimental case shows a greater degree of spreading as the spray exits the nozzle, causing greater retardation to the spray than in the computational case.
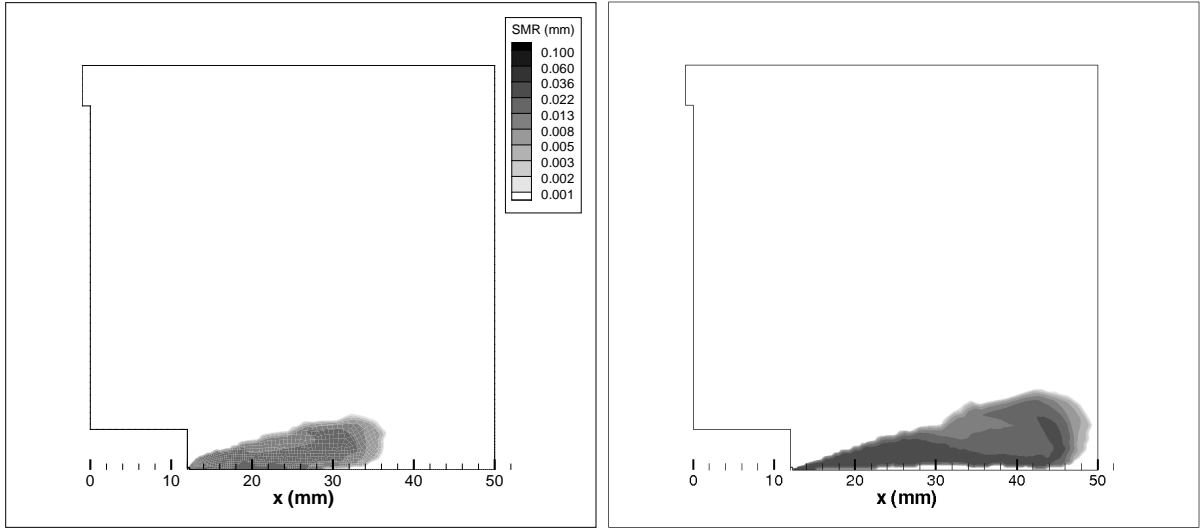
Figure 3.35: Sauter mean radius at 0.4 and 0.9ms

Early spreading of the spray outwards is strongly resisted by the gas phase as it is drawn towards the injector orifice by the sharp drop in pressure in that region, forming a small vortex just in front of the nozzle (Fig. 3.36).
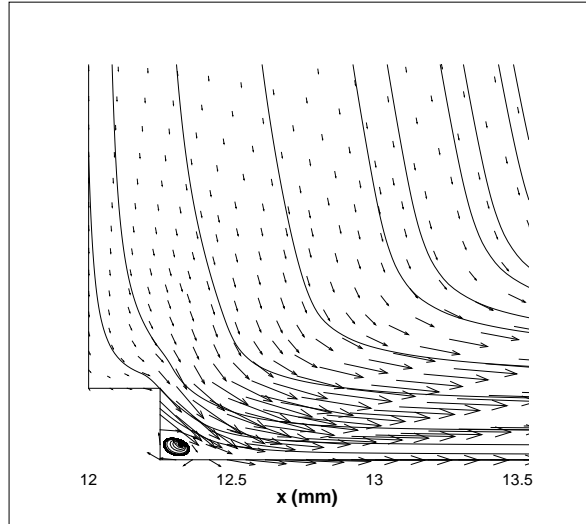

Figure 3.36: Near-nozzle flow of the surrounding gas (at 0.4ms)

The penetration rate of the spray model shown in Fig. 3.37 appears to be accurate, gradually slowing down as the spray progresses with spray tip arriving at the wall by 0.9ms, which is the initial impaction time recorded by Park et al. [2004].
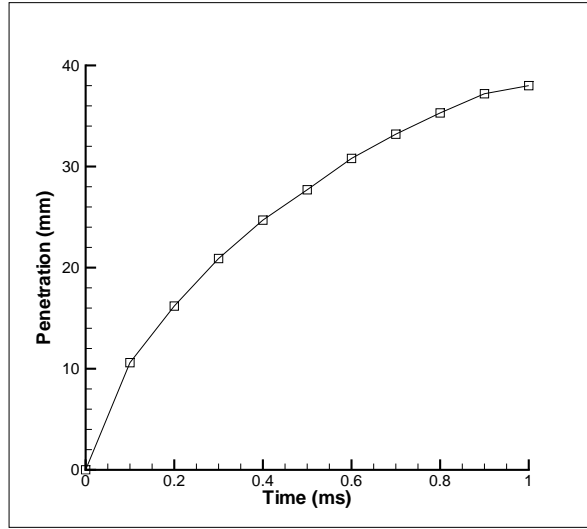
Figure 3.37: Penetration rate of the spray model

Although the injector pulse width is only 0.5ms, at both 0.9 and 1.4ms there still appears in Fig. 3.34 to be a strong concentration of the spray from the injector tip, appearing as though the injector is still spraying. This is also found in the computational results, as shown in Fig. 3.35 - 3.40, but with a reduced spray width at the tail-end of the spray. (At 10mm from the injector at 0.9 and 1.4ms the spray width is 9mm and 8mm respectively, whereas the computational results show half-thicknesses of 3mm and 2mm, respectively.)
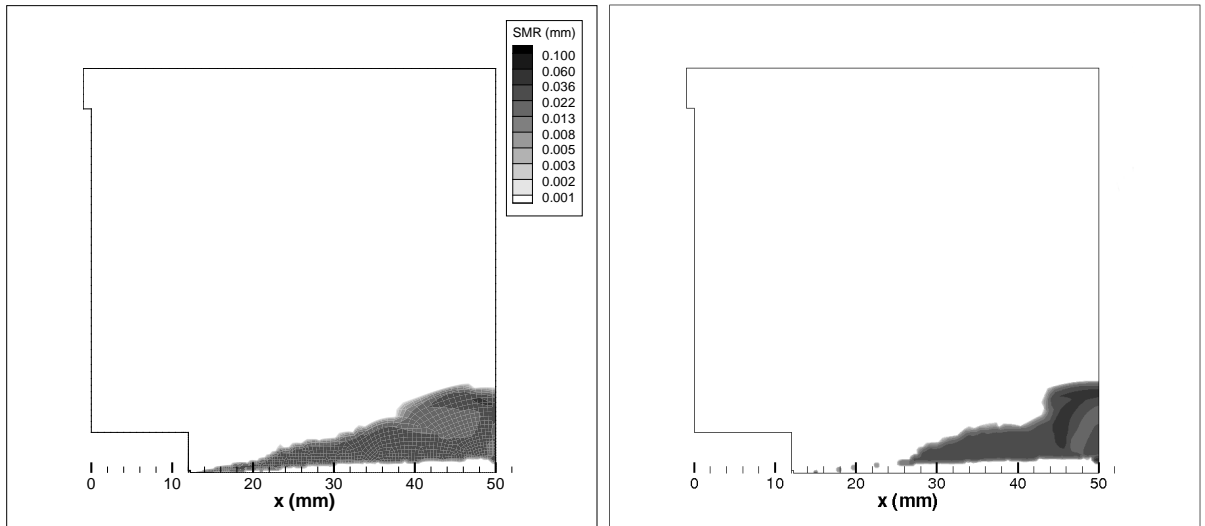

Figure 3.38: Sauter mean radius at 1.4 and 1.9ms

The contraction of the spray is attributed to the effect the continuum has on these trailing droplets. Figure 3.39(a) shows how the gas phase velocity forms an anti-clockwise vortex, which pushes the upstream spray towards the centreline resulting in a smaller SMR along the chordline (Fig. 3.39(b)) and pulls the downstream spray outwards.
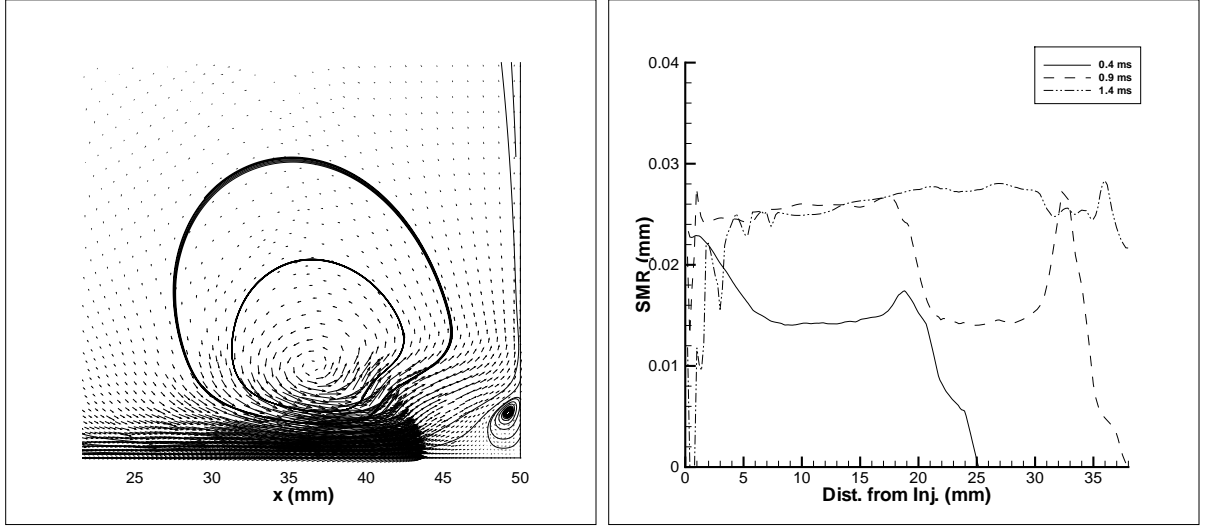
(a) Anti-clockwise vortex formed in the gas phase (b) SMR along the chordline from 0.4ms to 1.4ms (at 1.2ms)

Figure 3.39: Effect of the gas flow on the spray

Only after 1.9ms does the spray concentration drop downstream of the injector. This pattern of the spray development indicates that the trailing edge of the spray after injection is completed is being carried by the surrounding gas. This retardation of the trailing edge of the spray was also found in the computational model, as shown in Fig. 3.38 - 3.40.
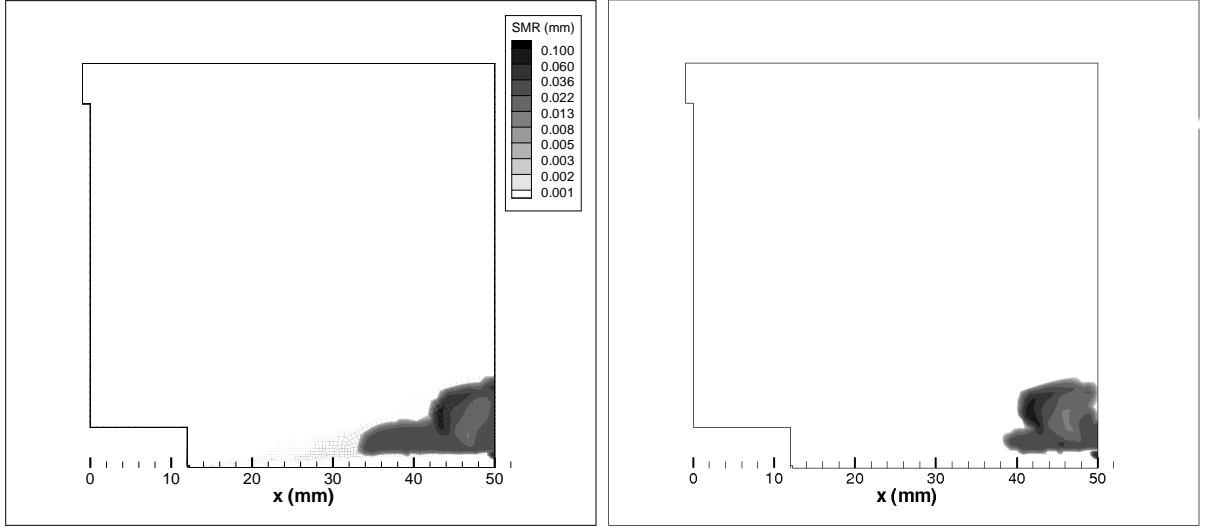
Figure 3.40: Sauter mean radius at 2.4 and 2.9ms

Chordline values of volume weighted SMR show the drop in mean radius near the wall due to the break-up of splashing droplets. Further out from the wall the SMR picks up because the splashing droplet distribution is strongly positively skewed.
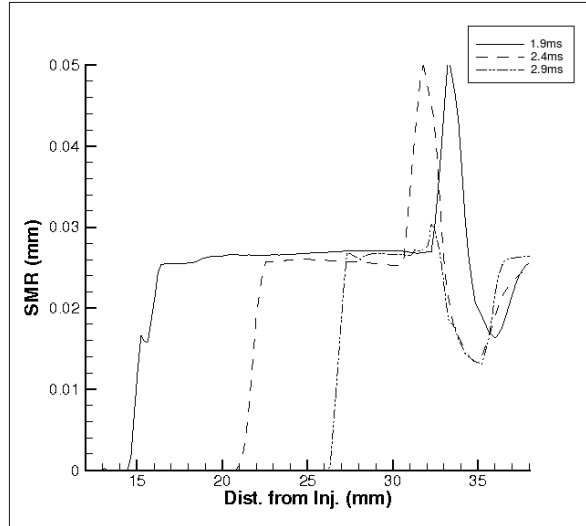

Figure 3.41: Sauter mean radius along the chordline from 1.9ms to 2.9ms

3.4.3 Near-wall Weber Number

The droplet Weber number

$$We_d = \frac{2r\,\rho_d V_{d,n}^2}{\sigma_d} \tag{3.5}$$

127

is sampled at locations in front of the wall, as shown in Fig. 3.42. Line abc is 1mm above the wall, line def is 3mm above the wall and lines ad, be and cf, are 0, 4 and 8mm from the centreline.
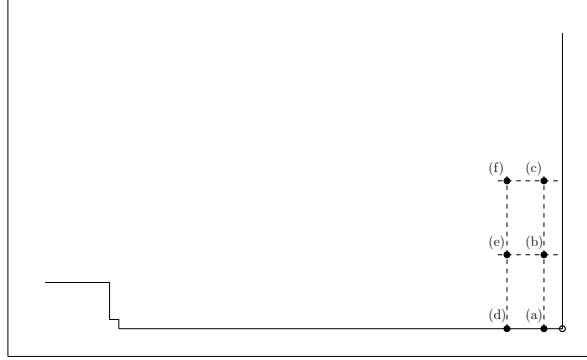

Figure 3.42: Sampled Weber number locations

Pre-impingement Weber numbers at each location were measured with respect to time and are plotted in Fig. 3.43 - 3.46, showing both the experimental data and the computational data where the spray was present. Park et al. [2004] states that the near-wall drop radii were in the range of 2 to 50 μm and the normal droplet velocity component was less than 15m/s. Computational data showed substantial over-prediction of the droplet velocity (with the largest value of 27m/s), which when squared in the calculation of the Weber number, further magnifies the error.

With the impinging droplets having such momentum, the post-impingement droplets will tend to have sufficient momentum to overcome the cross-flow of the gas phase, resulting in the droplets penetrating into the oncoming spray rather than being carried radially outward over the wall.
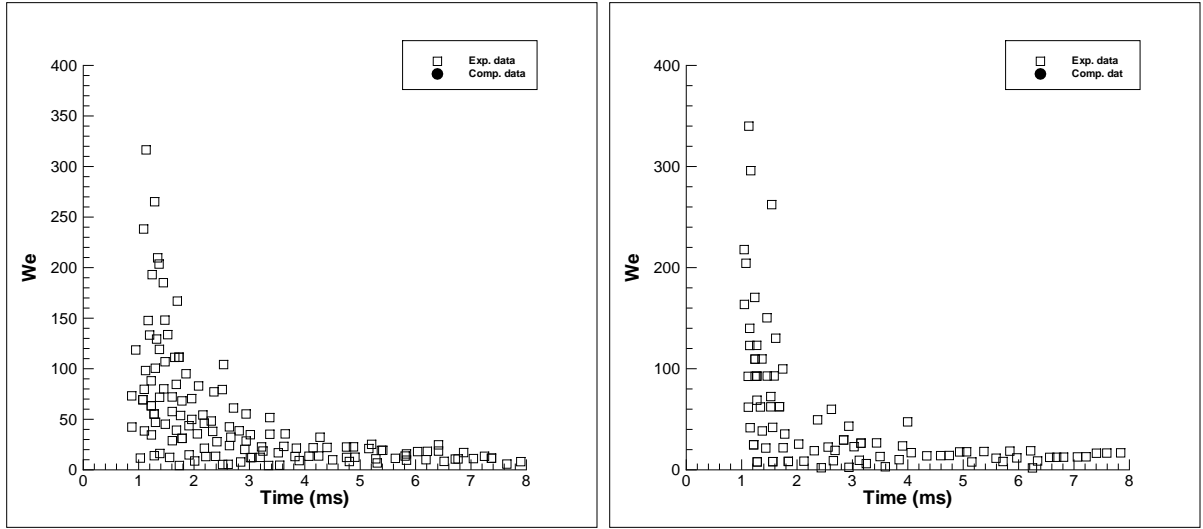
Figure 3.43: Weber number before impaction at positions (a) and (d)

Since the spray form was assumed to be a hollow cone shape in the computation, no centreline data exists in front of the wall (Fig. 3.43). However, experimental data shows a very clear presence of droplets heading towards the wall along the centreline. This indicates that the spray should have been modelled to consider the pre-swirl injection stage, as discussed in Wigley et al. [2001] (though details about the transient behaviour of the process in this case are lacking), whereby fuel initially exits the nozzle along the centreline as the injector needle opens and develops into a hollow cone as the spray gains swirl momentum (Fig. 3.44).

Figure 3.44: Pre-swirl injection stage [Wigley et al., 2001]

Four millimetres out from the centreline, the difference between the spray and the computational model are shown in Fig. 3.45. Initial over-prediction of the Weber number does decay rapidly with time, though by 4ms the entire injected spray has interacted with
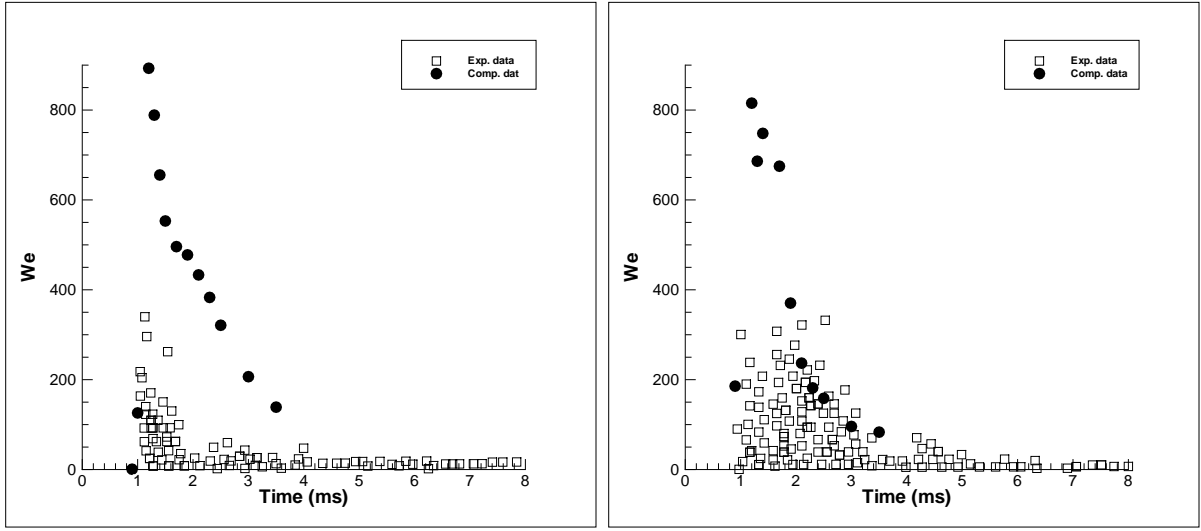
129

the wall.

Figure 3.45: Weber number before impaction at positions (b) and (e)

At the outer edge of the spray, the Weber numbers of the computation model remain high, whereas the experimental data shows decaying Weber numbers away from the centreline.

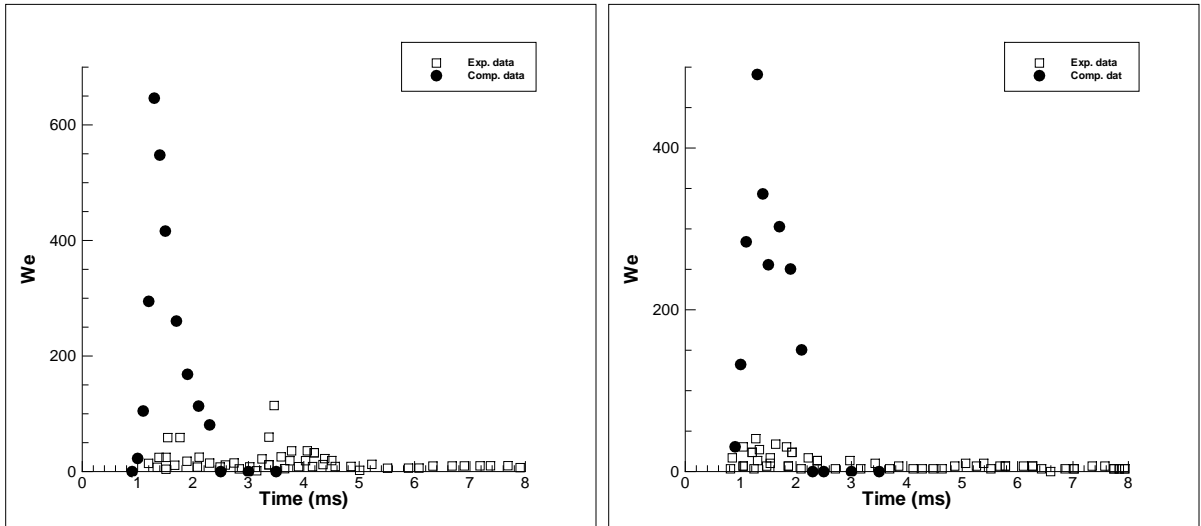Figure 3.46: Weber number before impaction at positions (c) and (f)

Post-impingement Weber numbers are shown in Fig. 3.47, where the experimental data is taken at the centreline position (a) and the computational data is taken at position (b)

because no data exists for position (a). The computational model shows that droplets rebound immediately after the spray begins to impact on the surface, whereas in the experimental case this only occurs after 3ms, implying that droplets prior to this time stuck to the surface, forming a film of liquid. Once the film is formed, rebounding readily occurs for droplets with low Weber numbers ($We < 5$).
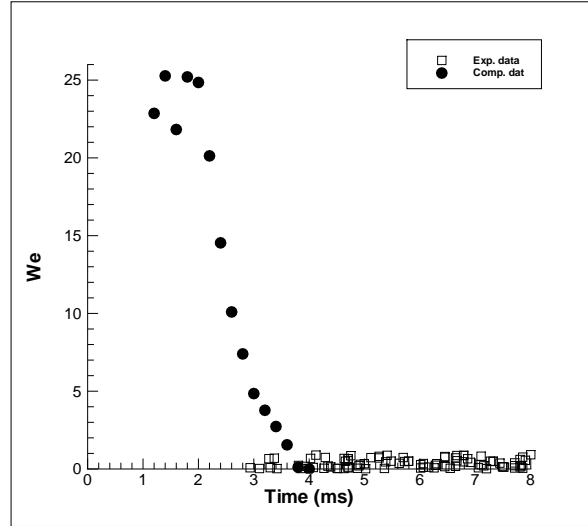

Figure 3.47: Weber number before and after impaction at position (a)

3.4.4   Wall Wetting

The wetted patch from the experimental results has a radius of approximately 11mm, which compares reasonably well with the wetted footprint produced by the model, shown in Fig. 3.48.
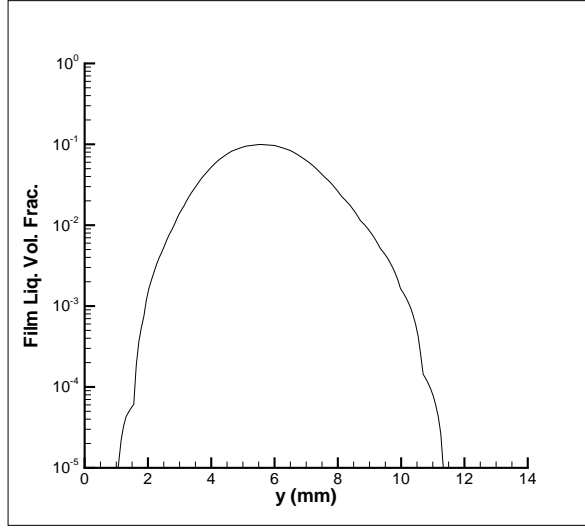
Figure 3.48: Near-wall liquid volume fraction

3.4.5 Conclusion

The complete spray model operating with optimal parameters shows that the current implementation is capable of simulating spray propagation and wall interaction to a reasonable degree of accuracy. The poor accuracy found in the comparison of near-wall Weber numbers is likely to be associated with the parameters set for the injection conditions, particularly the half-cone angle.

Further simulations were run with wider half-cone angles (25 and 30 degrees) though neither case ran to completion due to numerical divergence after 0.7ms. The cause of divergence is likely to be related to the increased effect of drag on the spray causing greater differentiation of the moments, leading to over-estimation of the SMR. These tests were attempted based on the assumption that as the cone angle is increased, near-wall droplet velocity would drop, bringing the Weber numbers more in line with the experimental data.

Further experimental comparisons with the spray model are not documented in this section since the parametric tests earlier in this chapter showed that the model is still in a substandard condition. Until the problematic parametric cases are re-addressed and corrected and the model is shown to be robust, such comparisons are considered to be of limited use.

Chapter 4

Conclusion

Project aims are revisited, with a discussion on how well these aims were achieved and further work is proposed to direct their improvement. Topics to be addressed which are outside the aims of the project are also presented as additional areas for future work.

4.1   Droplet Size Distribution

Much work has been done on investigating the methods for determining the underlying droplet size distribution, making use of the most recent research done in this area. This work revealed that the Maximum Entropy method is a very suitable candidate for determining the distribution, a conclusion which is quite different to that of Beck [2000]. Conditions have been found for checking the moments before the distribution is recovered as a means for determining which method to use.

Methods for distributing segmentation ordinates non-uniformly would enable fewer segmentations of the distribution to be performed, reducing the time to reconstruct the distribution and reducing the time required to solve the hydrodynamic terms dependent on the distribution.

4.2 Droplet Velocity Profile

The application of non-uniform velocity profiles has been implemented. Although the revised profile implemented did not characterize the droplet velocity accurately enough to allow the lower moments to be transported properly, it provides sufficient improvement to enable the full spray model to be run using high order moments. Varying the exponent showed how significantly the velocity distribution effects the characteristics of the spray, indicating how important it is to ensure the profile is estimated accurately.

Further research is necessary for developing well behaved droplet velocity profiles based on the complete set of available moment averaged velocities. General forms could be constructed using the methods presented for the construction of the probability density function. An accurate representation of the droplet velocity is the key component to successfully implementing this spray model since it is required in all the source terms and boundary conditions presented. As discussed by Tagliani [2001], the reconstruction of such a distribution is well conditioned, so should not be too difficult to compute.

The hydrodynamic contributions are generally over-estimated for the lower order moments (such as the inter-phase drag) which is due to either the droplet size distribution being too strongly positively skewed and/or the droplet velocity profile over-estimating the difference between the velocity of the smaller droplets and the velocity of the surrounding gas. An attempt to minimize this difference could be performed by prescribing certain conditions of the velocity profile, such as the gradient of the distribution must be equal to zero at the tails. These kind of conditions can be set using the Splines reconstruction method, potentially leading to a profile of the shape (b) in Fig. 4.1, rather than the current kind of shape, (a). This alternative shape would significantly reduce the inter-phase drag and break-up terms for the lower moments, which will alleviate many of the numerical problems associated with the spray model presented.
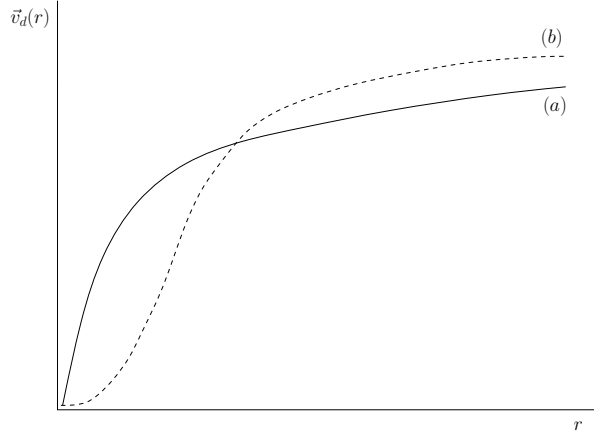
Figure 4.1: Revised droplet velocity profile

As an alternative to solving the droplet velocity profile, the droplet velocity magnitude profile could be solved instead. This would enable an additional condition to be supplied for the reconstruction of the profile; that the profile must be greater than or equal to zero. Such a condition would be very useful if the splines method were used.

4.3 Grid Topology

The spray model has been shown to work very well on an unstructured grid, enabling fine resolution of the near injector region without compromising the grid quality. This is an important advancement, enabling the strong gradients of the spray velocity, continuum velocity and pressure to be resolved. No special treatment of defining the spray edge has been required to prevent excess radial spread due to numerical diffusion. This has partly been due to the improved resolution of the grid around the injector.

4.4 Convection and Temporal Schemes

High order convection schemes for all transport equations were implemented. The lack of such schemes was a major shortcoming in both the works of Beck [2000] and Lemini [2004] and both authors acknowledged the need to address this. Three types of schemes were implemented; the central differencing (which was not used), TVD scheme for the velocities and turbulence models and HRIC scheme for the moments. The use of the

HRIC scheme had the most significant effect on the spray, enabling clearer resolution of the hollow cone spray structure.

Implementation of the Three time levels method for approximating the temporal terms show noticeable, though not considerable, difference in the spray compared to the Euler implicit scheme used by Beck [2000].

4.5   Wall Impaction

A suitable wall impaction model was implemented successfully to the spray model which retains as much detail of the rebounding and splashing sprays as the impinging spray, enabling coexistence of all three sprays within a given volume. The model has been shown to work successfully, transitioning the impaction conditions from dry to wet with the data obtained from the liquid film equation.

4.6   Further Topics

4.6.1   Collision Model

When interpenetration of sprays occur, such as when the incoming and rebounding sprays cross paths near the wall, the current collision model does not consider collision between the two sprays. Extension of the collision model to consider this possibility is required.

4.6.2   Grid Adaption

Retaining a high level of grid refinement in the regions of the domain where the spray is expected to be present or has been present brings significant computational costs, especially for three dimensional simulations. Adapting the grid based on whether the spray is present in a particular region would be a more cost effective approach. Grid adaption may also be extended to dealing with moving parts within the grid, such as the movement of the piston and valves inside a combustion chamber, enabling the complete combustion cycle to be modelled.

4.6.3 Pressure-Velocity Coupling

The standard methodology for solving the coupled pressure and velocity fields is performed using the SIMPLE based schemes. However, this scheme converges slowly, especially in the case of modelling the spray interaction with the surrounding gas around the injector.

An alternative approach to coupling the pressure and velocity, which according to the results from Darwish and Moukalled [2009] will converge up to 100 times faster than the SIMPLE scheme, is to couple pressure and velocity implicitly. The continuity equation, $\sum_k \dot{m}_k = 0$, is re-written by replacing $\vec{v}_k$ by $\overline{\vec{v}}_k - D(\Delta p - \overline{\Delta p})$ [Ferziger and Perić, 2002], resulting in equations for momentum and continuity containing velocity and pressure. Combining the algebraic form of both equations, a single system of linear equations is constructed (Fig. 4.2).

$$
\begin{bmatrix} A^u & A^{uv} & A^{up} \\ A^{vu} & A^v & A^{vp} \\ A^{pu} & A^{pv} & A^p \end{bmatrix} \begin{bmatrix} u \\ v \\ p \end{bmatrix} = \begin{bmatrix} b^u \\ b^v \\ b^p \end{bmatrix}
$$

Figure 4.2: Form of the pressure-velocity system of equations

Appendix A

Software Resources

Name	Description
Ubuntu	Distribution of the Linux kernel
Xfce	Desktop environment
gfortran	Fortran compiler
ifort	Intel Fortran compiler
ddd	Debugging front-end for gdb
MPICH	MPI library
Kdevelop	Programming integrated development environment
Gmsh	Meshing utility
Gambit	Meshing utility (commercial)
Paraview	Mesh and data visualization
Tecplot	Mesh and data visualization (commercial)
g3data	Data extraction utility
IPE drawing editor	Draw schematics, export in .eps
GIMP	Drawing software and image converter
Gnuplot	Graph and contour plotting utility
Kile	Latex front-end

Appendix B

Droplet Velocity Profile

Since the Maximum Entropy formalism performed the best in reconstructing the droplet size distribution (see Sect. 3.1.4), here the method is also tested for constructing the droplet velocity profile.

The Maximum Entropy formalism is employed to solve

$$\vec{V}_{d,i} = \frac{\mu_0}{\mu_i} \int_r \phi(r)\, r^i\, \vec{v}_d(r)\, \mathrm{d}r \tag{B.1}$$

given the first four moments of the droplet size distribution and the moment-averaged velocities. For the following sample case, the moments of the droplet size distribution set as

$$\mu_0 = 7.14173 \text{ x} 10^{-1}$$
$$\mu_1 = 1.78571 \text{ x} 10^{-1}$$
$$\mu_2 = 5.95319 \text{ x} 10^{-2}$$
$$\mu_3 = 2.38156 \text{ x} 10^{-2}$$

and the moment-averaged x-component velocities are

$$V_{d,0} = 20$$
$$V_{d,1} = 21$$
$$V_{d,2} = 23$$
$$V_{d,3} = 27$$

The Maximum Entropy formalism is represented here in its general form in order to describe the solution of both the probability density function, $\phi(r)$, and the droplet

velocity profile, $\vec{v}_d(r)$. The continuous function to be recovered is defined as

$$q(r) \approx p(r) \exp\left[-\sum_{i=0}^{N-1} \lambda_i e_i(r)\right] \qquad (B.2)$$

where $p(r)$ is the preconditioning function and $e_i(r)$ is the external function where both of which are assumed to be known, along with the moments and moment-averaged velocities.

First, the PDF is recovered by substituting Eq. (B.2) into Eq. (2.1) and solving the Lagrange multipliers, λ_i in the resulting equation (Eq. (B.3)).

$$f_j(\underline{\lambda}) = \int_r e_j(r)\, p(r) \exp\left[-\sum_{i=0}^{N-1} \lambda_i e_i(r)\right] \mathrm{d}r = \frac{\mu_j}{\mu_0} \qquad (B.3)$$

For this sample case, $p(r)$ is defined as the Rayleigh distribution and $e_k(r) = r^k$. The resultant PDF along with its preconditioning PDF, $p(x)$, is shown in Fig. B.1.
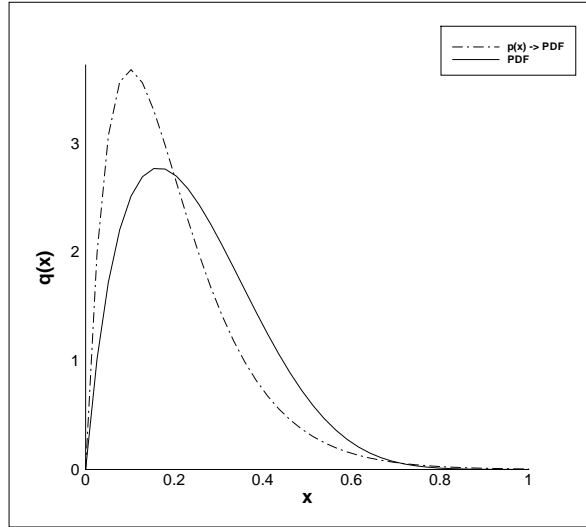

Figure B.1: Recovered PDF with its preconditioning PDF

Once the PDF is recovered, a similar procedure is used to solve the droplet velocity profile, $v_d(r)$. Substituting Eq. (B.2) into Eq. (B.1) and normalizing the result gives

$$f_j(\underline{\lambda}) = \frac{1}{V_{d,0}} \int_r e_j(r)\, p(r) \exp\left[-\sum_{i=0}^{N-1} \lambda_i e_i(r)\right] \mathrm{d}r = \frac{\mu_0}{\mu_j}\frac{V_{d,j}}{V_{d,0}} \qquad (B.4)$$

where $p(r)$ is defined as a linear function where at $r = 0$, $p(r) = 1$ and at $r = r_{max}$,

$p(r) = \frac{V_{d,3}}{V_{d,0}}$. The external function now includes the PDF, giving $e_k(r) = \phi(r)\, r^k$. The resulting preconditioning droplet velocity profile and the recovered droplet velocity profile are shown in Fig. B.2.
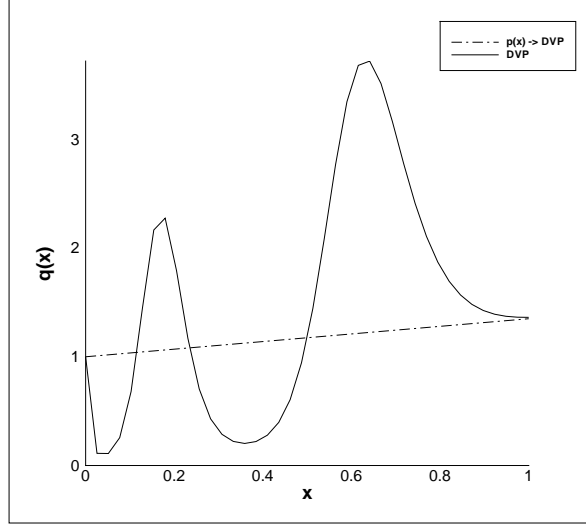

Figure B.2: Recovered DVP with its preconditioning DVP

As shown in Fig. B.2, resultant droplet velocity profile is very unrealistic and is most likely due to the droplet velocity profile not tending to zero at the tails. This test shows that solving the velocity profile accurately will require a different approach then that used to solve the PDF.

A possible way forward is to abandon the constraint of the moment-averaging condition (until a correct alternative is found) and simply construct a best guess velocity profile from the moment-averaged velocities available, as in the example of Fig. B.3.
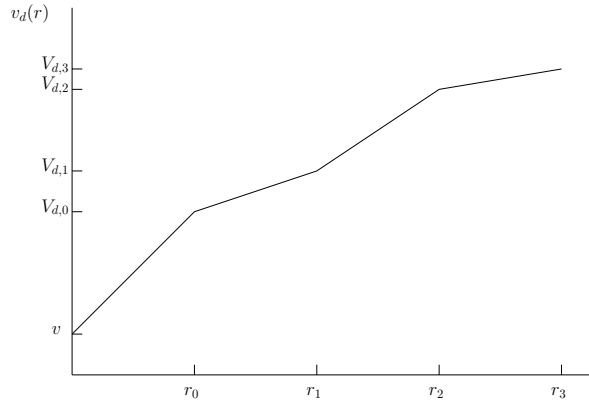

Figure B.3: Alternative droplet velocity profile construction

141

If no satisfactory solution is found, the spray model may need to be rewritten into a form such that the underlying droplet size distribution and droplet velocity distribution are found through constructing the bivariate probability density function, $\phi(r, v_d)$. Methods for reconstructing such a distribution are found in Woodbury [2004], Sellens [1989], Ayres et al. [2001] and Abramov [2009]. However, the work by Gurpura [2007] is a excellent first reference, as it considers the context of the use of the PDF in additon to its construction.

Appendix C

Platform Validation

The spray model presented was incorporated into a CFD code which solves incompressible fluid flow using pressure based coupling. The CFD code in addition to the spray model were developed in this work. Here, sample cases are presented which were used to validate the platform code, comparing results with those in Ferziger and Perić [2002].

C.1   Moving Lid

This case provides a means for testing the pressure-velocity coupling, convection and diffusion schemes, turbulence model and the implementation of the wall boundary conditions. For the laminar case, the flow has a Reynolds number of 1000 with respect to the length of the square domain and the moving north wall. The grid used is non-uniform and orthogonal, refined close to the walls (Fig. C.1(a)). Expected flow structure is found, as shown in Fig. C.1(b) with the primary vortex dominating the flow and two secondary vorticies in the lower corners. Similar cases with Reyonlds numbers of 5000 and 10000 are run with the turbulence model on. Anaylsis of the results are performed by comparing velocity profiles at $x = 0.5$ and $y = 0.5$ with experimental data from Ghia et al. [1982]. For the laminar case (Fig. C.2), profiles match the experimental data very well, though for the turbulent cases (Fig. C.3 and C.4), the velocity magnitude is under-predicted.
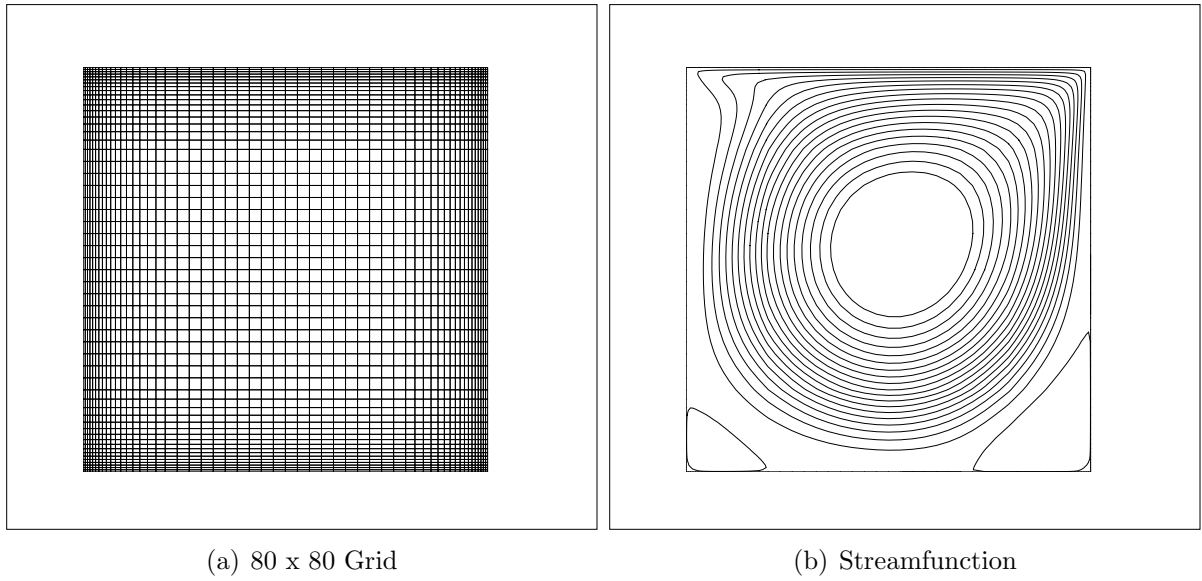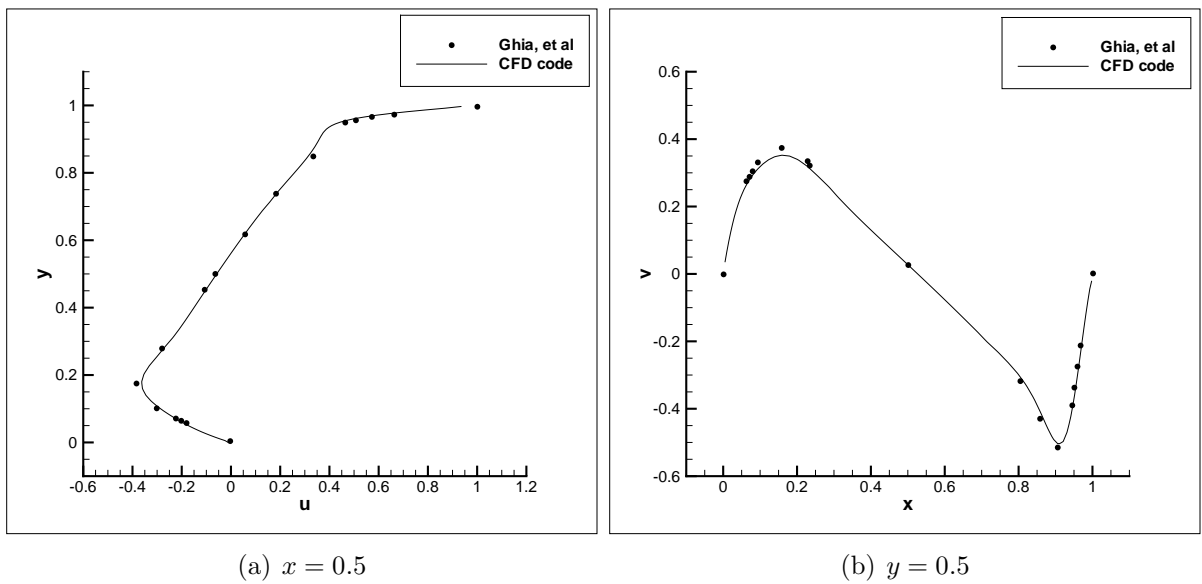
(a) 80 x 80 Grid

(b) Streamfunction

Figure C.1: Cavity flow at Re = 1000

(a) $x = 0.5$

(b) $y = 0.5$

Figure C.2: Velocity comparison for cavity flow at Re = 1000

(a) $x = 0.5$

(b) $y = 0.5$
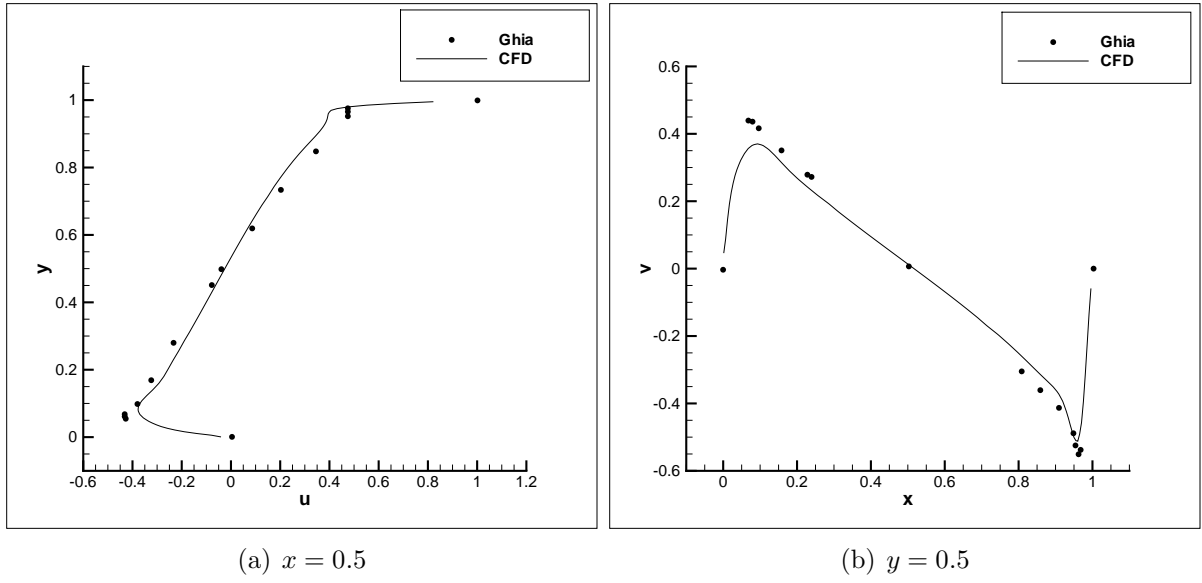
Figure C.3: Velocity comparison for cavity flow at Re = 5000
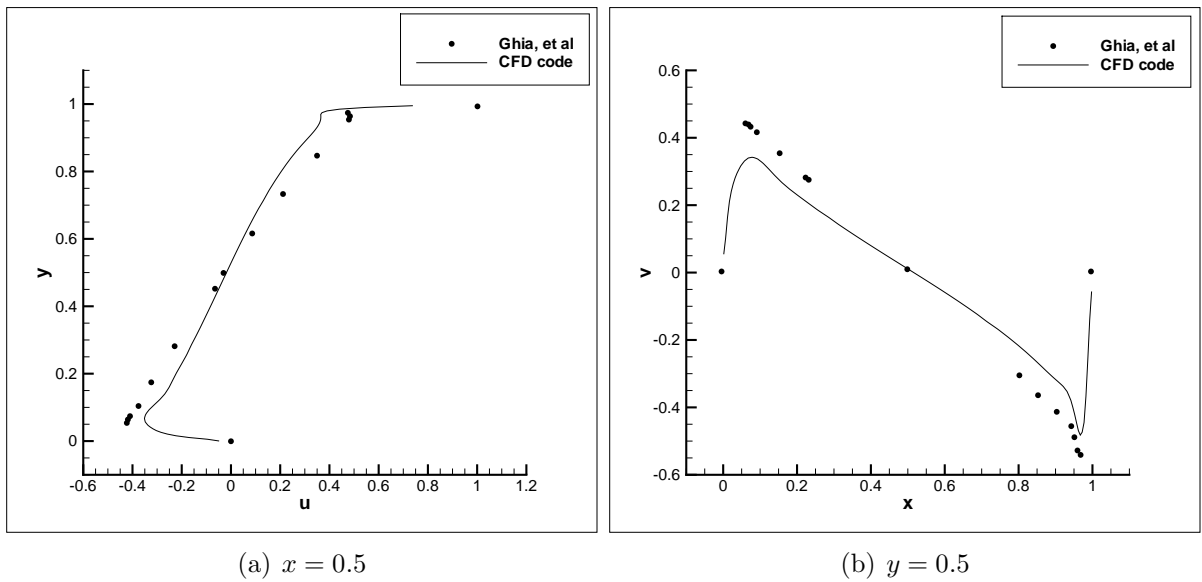

(a) $x = 0.5$

(b) $y = 0.5$

Figure C.4: Velocity comparison for cavity flow at Re = 10000

C.2 Flow Around a Cylinder

This second case introduces non-orthogonal grid structure, time dependence and inlet and outlet boundary conditions. The case is taken from Ferziger and Perić [2002]. Lift and drag coefficients are calculated around the cylinder and compared to the results of Ferziger and Perić [2002].

C.2.1 Steady Flow

At a Reynolds number of 20, the flow around the cylinder is steady, as shown by the streamfunction in Fig. C.5(b). The drag coefficient obtained about the cylinder is found to be 5.61, which is slightly higher than 5.58 found in Ferziger and Perić [2002]. The simulation was run on four grids with 1554, 3999, 4908 and 9710 CVs. Convergence of the drag coefficient was found with the 4908 CV grid.
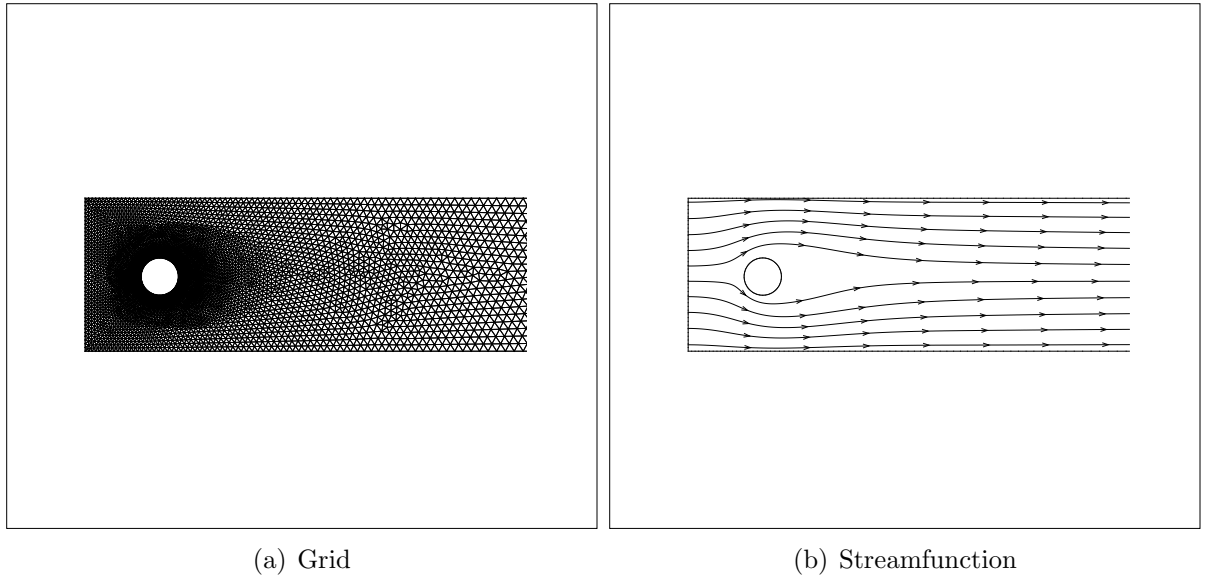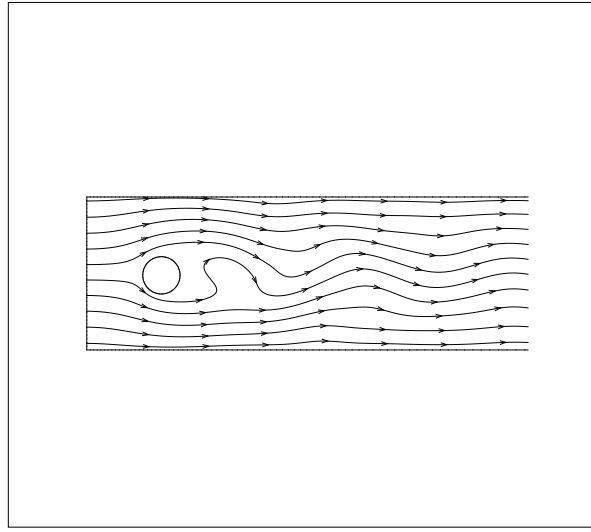

        (a) Grid   (b) Streamfunction
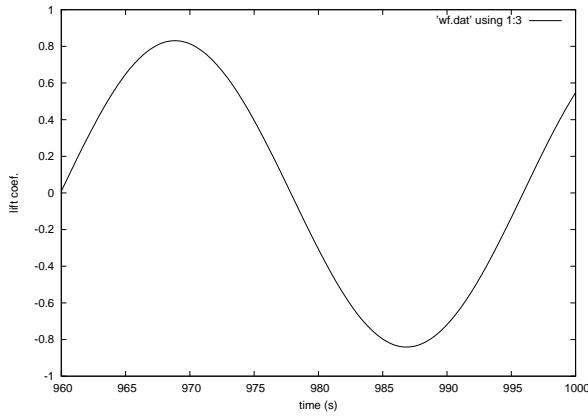
Figure C.5: Channel flow at Re=20

C.2.2 Unsteady Flow

Increasing the Reynolds number to 100 causes the flow to become unsteady. Transient lift and drag coefficients are plotted, showing the frequency of the drag to be twice that of the lift. Lift and drag ranges were found to be consistant with Ferziger and Perić [2002],

where maximum and minimum lift for this case are 0.86 and -0.85 compared to 0.987 and -1.021 from Ferziger and Perić [2002] and the maximum and minimum drag are 3.22 and 3.17 compared to 3.228 and 3.165. For this case two grids were used from the steady state case; 4908 and 9710 CV grids. Convergence of the maximum and minimum drag coefficient values was found on the coarser grid. The lower and upper values of lift and drag are not expected to be of the same magnitude since the domain is not symmetrical along the x-axis (in order to promote unsteady flow).

(a) Streamfunction

(b) Lift coefficient
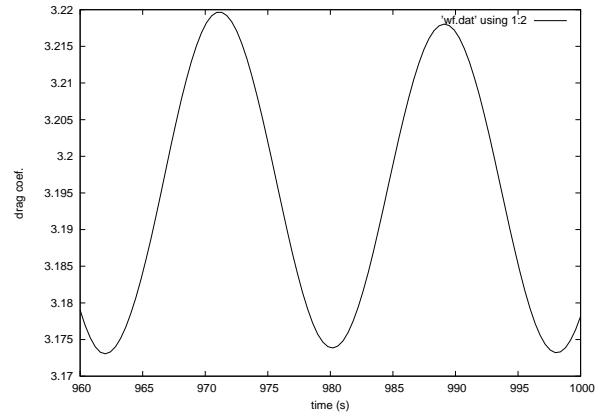
(c) Drag coefficient

Figure C.6: Channel flow at Re=100

Whilst small discrepancies exist between results by Ferziger and Perić [2002] and this code for the flow round the cylinder, it is likely to be due to differences in treatment of grid non-orthogonality, interpolation and choice of convection scheme. Further validation

cases were performed for 2D street canyon flows, though results are not available (see http://www2.dmu.dk/atmosphericenvironment/trapos/cfd-wg.htm for the cases).

References

A. A. Kaufmann, M. Moreau, O. Simonin, and J. Helie. Comparison between lagrangian and mesoscopic eulerian modelling approaches for inertial particles suspended in decaying isotropic turbulence. *Journal of Computational Physics*, 227:6448–6472, 2008.

R. V. Abramov. The multidimensional moment-constrained maximum entropy problem: A bfgs algorithm with constraint scaling. *Journal of Computational Physics*, 228:96–108, 2009.

M. Ahmadi and R. W. Sellens. A simplified maximum-entropy-based drop size distribution. *Atomization and Sprays*, 3:291–310, 1993.

D. Ayres, M. Caldas, V. Semiao, and M. da Graca Carvalho. Prediction of the droplet size and velocity joint distribution for sprays. *Fuel*, 80:383–394, 2001.

C. Bai and A. D. Gosman. Development of methodology for spray impingement simulation. *SAE Technical Paper Series*, (950283), 1995.

J. C. Beck. *Computational modelling of polydisperse sprays without segregation into droplet size classes.* Ph. D. Thesis, UMIST, 2000.

J. C. Beck and A. P. Watkins. On the development of spray submodels based on droplet size moments. *J. of Comp. Phys.*, 182:586–621, 2002.

J. C. Beck and A. P. Watkins. On the development of a spray model based on drop-size moments. *Proc. R. Soc. Lond.*, A(459):1365–1394, 2003a.

J. C. Beck and A. P. Watkins. The droplet number moments approach to spray modelling: The development of heat and mass transfer sub-models. *Int. J. of Heat and Fluid Flow*, 24:242–259, 2003b.

F. V. Bracco. Modeling of engine sprays. *SAE Technical Paper Series 850394*, 1985.

S. J. Chapman. *Fortran 95/2003 for scientists and engineers.* McGraw Hill, third edition, 2008.

C. T. Crowe, M. Sommerfeld, and Y. Tsuji. *Multiphase Flows with Droplets and Particles.* CRC Press, 1998.

M. S. Darwish and F. Moukalled. Tvd schemes for unstructured grids. *Int. J. of Heat and Mass Transfer*, 46:599–611, 2003.

M. S. Darwish and F. Moukalled. A coupled finite volume solver for the solution of incompressible flows on unstructured grids. *Journal of Computational Physics*, 228: 180–201, 2009.

O. Desjardins, R. O. Fox, and P. Villedieu. A quadrature-based moment closure for the Williams spray equation. *Center for Turbulence Research Proceedings*, pages 223–234, 2006.

J. H. Ferziger and M. Perić. *Computational Methods for Fluid Dynamics*. Springer, third edition, 2002.

R. O. Fox. A quadrature-based third-order moment method for dilute gas-particle flows. *Journal of Computational Physics*, 227:6313–6350, 2008.

U. Ghia, K. N. Ghia, and C. T. Shin. High-re solutions for incompressible ow using the navierstokes equations and a multigrid method. *Journal of Computational Physics*, 48 (3):387–411, 1982.

A. D. Gosman and D. Clerides. Diesel spray modelling: A review. *Imperial College of Science, Technology and Medicine Department of Mechanical Engineering*, 1997.

R. O. Grover and D. N. Assanis. A spray wall impingement model based upon conservation principles. *The Fifth International Sympostum on Diagnostics and Modeling of Combustion in Internal Combustion Engines*, 2001.

M. Gurpura. *Probability density function formalism for multiphase flows*. Ph. D. Thesis, Iowa State University, 2007.

L. P. Hsiang and G. M. Faeth. Near-limit drop deformation and secondary breakup. *Int. J. Multiphase Flow*, 18(5):635–652, 1992.

V. John, I. Angelov, A. A. Oncul, and D. Thevenin. Techniques for the reconstruction of a distribution from a finite number of its moments. *Chemical Engineering Science*, 62: 2890–2904, 2007.

B. E. Launder and D. B. Spalding. The numerical computation of turbulent flows. *Comput. Methods Appl. Mech. Eng.*, 3:269–289, 1974.

E. Lemini and A. P. Watkins. Development of a spray wall impaction model without discretisation into droplet size classes. *ILASS-Europe 2002*, 2002.

E. E. Lemini. *A new methodology for modelling impinging sprays based on drop size moments*. Ph. D. Thesis, UMIST, 2004.

D. L. Marchisio and R. O. Fox. Solution of population balance equations using the direct quadrature method of moments. *Aerosol Science*, 36:43–73, 2005.

R. McGraw. Description of aerosol dynamics by the quadrature method of moments. *Aerosol Science and Technology*, 27:255–265, 1997.

J. B. Moreau, O. Simonin, and C. C. Habchi. A numerical study of cavitation influence on diesel jet atomisation. *Proceedings of the 19th ILASS - Europe Meeting 2004*, 2004.

F. Moukalled and M. Darwish. Droplet evaporation and mixing in subsonic flow using the musig and h-musig models. *ILASS-Europe*, 2008.

S. Muzaferija and M. Peric. Computation of free-surface flows using interface tracking and interface-capturing methods. *Non-linear Water Wave Interaction*, pages 59–100, 1999.

J. A. Nicholls. Stream and droplet breakup by shock waves. *in NASA SP194 (Eds. D.T. Harrje and F.H. Reardon)*, pages 126–128, 1972.

F. Obermeier and H. Chaves. Initial modelling of splashing phenomena. *IDEA Project, Subprogram A3*, 1991.

P.J. O'Rourke. *Collective Drop Effects on Vaporising Liquid Sprays*. PhD Thesis, University of Princeton, 1981.

J. S. Park, H. S. Kim, and M. C. Lai. Visualization and measurement of a narrow-cone di gasoline spray for the impingement analysis. *Int. J. of Automotive Technology*, 5(4): 221–238, 2004.

S. V. Patankar. *Numerical heat transfer and fluid flow*. Hemisphere publishing corporation, Taylor and Francis group, New York, 1980.

M. Pilch and C. A. Erdman. Use of breakup time data and velocity history data to predict the maximum size of stable fragments for acceleration-induced breakup of a liquid drop. *Int. J. Multiphase Flow*, 13(6):741–757, 1987.

R. D. Reitz and R. Diwakar. Effect of drop breakup on fuel sprays. *SAE Technical Paper Series*, (860469), 1986.

J. Reveillon, M. Massot, and C. Pera. Analysis and modeling of the dispersion of vaporizing polydispersed sprays in turbulent flows. *Center for Turbulence Research Proceedings of the Summer Program*, 2002.

R. W. Sellens. Prediction of the drop size and velocity distribution in a spray, based on the maximum entropy formalism. *Part. Syst. Charact.*, 6:17–27, 1989.

O. J. Soriano and R. Rotondi. Linking nozzle flow and primary breakup of high pressure diesel jets using cfd. *ILASS-Europe*, 2008.

D. W. Stanton and C. J. Rutland. Multi-dimensional modeling of heat and mass transfer of fuel films resulting from impinging sprays. *SAE Paper*, (980132), 1998.

A. Tagliani. Hausdorff moment problem and maximum entropy: A unified approach. *Applied Mathematics and Computation*, 105:291–305, 1999.

A. Tagliani. Numerical aspects of finite Hausdorff moment problem by maximum entropy approach. *Applied Mathematics and Computation*, 118:133–149, 2001.

G. Talenti. Recovering a function from a finite number of moments. *Inverse Problems*, 3: 501–517, 1987.

R. Tatschl, C. V. Kunsberg, and E. Berg. Ic-engine spray modeling status and outlook. *International Multidimensional Engine Modeling Users Group Meeting, SAE Congress*, 2002.

T. Tomoda, M. Kubota, and R. Shimizu. Numerical analysis of mixture formation of a direct injection gasoline engine. *The Fifth International Sympostum on Diagnostics and Modeling of Combustion in Internal Combustion Engines*, 2001.

O. Ubbink. *Numerical predication of two fluid systems with sharp interfaces*. Ph.D Thesis, University of London, 1997.

H. K. Versteeg and W. Malalasekera. *An Introduction to Computational Fluid Dynamics*. Pearson, second edition, 2006.

M. Vujanovic, W. Edelbauer, E. von Berg, R. Tatschl, and N. Dui. Enhancement and validation of an Eulerian-Eulerian approach for diesel sprays. *ILASS-Europe*, 2008.

T. Waclawczyk and T Koronowicz. Modeling of the wave breaking with cicsam and hric high-resolution schemes. *European Conference on Computational Fluid Dynamics*, 2006.

A. P. Watkins. Modelling the mean temperatures used for calculating heat and mass transfer in sprays. *International Journal of Heat and Fluid Flow*, 2006.

G. Wigley, G. Pitcher, D. Law, B. Schneider, and S. Rogers. Effect of compression pressure on the spray morphology of gdi pressure-swirl injectors. *The Fifth International Sympostum on Diagnostics and Modeling of Combustion in Internal Combustion Engines*, 2001.

G. Wigley, G. Pitcher, M. Goodwin, and D. Blondel. Imaging and pda analysis of a gdi spray in the near-nozzle region. *Experiments in Fluids*, 36:565–574, 2004.

A. D. Woodbury. A Fortran program to produce minimum relative entropy distributions. *Computers and Geosciences*, 30:131–138, 2004.

B. Yue and A. P. Watkins. Mathematical development and numerical analysis of further transport equations for the droplet size moment theory. *19th Annual Meeting of the Institute for Liquid Atomization and Spraying Systems (Europe)*, 2004.